

## Insight into the multifunctionality of TiO<sub>2</sub>-based catalyst

Meeprasert, J.

**DOI**

[10.4233/uuid:e88a9277-41a0-495e-8af2-561fbe1a543b](https://doi.org/10.4233/uuid:e88a9277-41a0-495e-8af2-561fbe1a543b)

**Publication date**

2023

**Document Version**

Final published version

**Citation (APA)**

Meeprasert, J. (2023). *Insight into the multifunctionality of TiO<sub>2</sub>-based catalyst*. [Dissertation (TU Delft), Delft University of Technology]. <https://doi.org/10.4233/uuid:e88a9277-41a0-495e-8af2-561fbe1a543b>

**Important note**

To cite this publication, please use the final published version (if applicable).  
Please check the document version above.

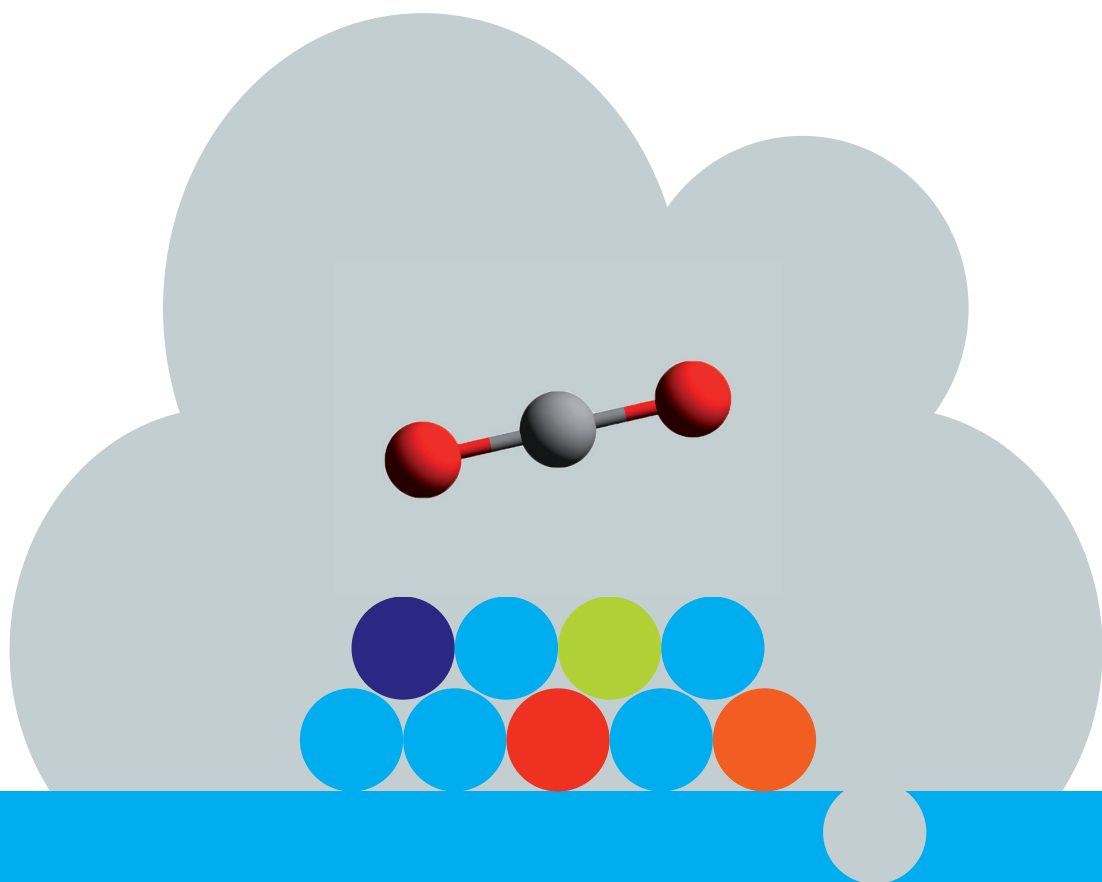
**Copyright**

Other than for strictly personal use, it is not permitted to download, forward or distribute the text or part of it, without the consent of the author(s) and/or copyright holder(s), unless the work is under an open content license such as Creative Commons.

**Takedown policy**

Please contact us and provide details if you believe this document breaches copyrights.  
We will remove access to the work immediately and investigate your claim.

# Insight into the multifunctionality of $\text{TiO}_2$ -based catalyst



Jittima Meeprasert

# Insight into the multifunctionality of TiO<sub>2</sub>-based catalyst

## Dissertation

for the purpose of obtaining the degree of doctor  
at Delft University of Technology  
by the authority of the Rector Magnificus,  
Prof.dr.ir. T.H.J.J. van der Hagen,  
chair of the Board of Doctorates  
to be defended publicly on  
Wednesday, 15 March 2023 at 15:00 o'clock

by

**Jittima MEEPRASERT**

Master of Science in Chemistry,  
Kasetsart University, Thailand,  
Born in Bangkok, Thailand

This dissertation has been approved by the promotor.

Promotor: Prof.dr. E. A. Pidko

Copromotor: Dr. G. Li

**Composition of the doctoral committee:**

Rector Magnificus	Chairperson
Prof.dr. E. A. Pidko	Delft University of Technology, promotor
Dr. G. Li	Wageningen University and Research, copromotor

**Independent members:**

Dr. N. Artrith	Utrecht University
Prof.dr. B.M. Szyja	Wroclaw University, Poland
Prof.dr.ir. A. Urakawa	Delft University of Technology
Dr.ir. M.A. van der Veen	Delft University of Technology
Prof.dr. F.M. Mulder	Delft University of Technology

The work described in this dissertation was carried out in the Inorganic Systems Engineering (ISE) group, Department of Chemical Engineering, Faculty of Applied Science, Delft University of Technology. The research was supported by the Royal Thai Government Scholarship and the European Research Council under the European Union's Horizon 2020 Research and Innovation Program (Grant Agreement No. 725686). Access to SurfSARA supercomputer resources was sponsored by the Netherlands Organization for Scientific Research (NWO).

Printed by: Proefschriftspecialist

Cover by: Jittima Meeprasert

Copyright © 2023 by Jittima Meeprasert

ISBN 978-94-6384-413-0

An electronic version of the dissertation is available at TU Delft library

# Contents

<b>1 Introduction</b>	<b>1</b>
<b>2 CO<sub>2</sub> hydrogenation to CH<sub>3</sub>OH on Cd<sub>4</sub>/TiO<sub>2</sub></b>	<b>27</b>
<b>3 C<sub>6</sub>H<sub>6</sub> esterification with CO<sub>2</sub> and CH<sub>3</sub>OH on K<sub>2</sub>CO<sub>3</sub>/TiO<sub>2</sub></b>	<b>49</b>
<b>4 CH<sub>4</sub> esterification with CO<sub>2</sub> and CH<sub>3</sub>OH on K<sub>2</sub>CO<sub>3</sub>/TiO<sub>2</sub></b>	<b>65</b>
<b>5 Benzonitrile hydrogenation on Au<sub>13</sub>/TiO<sub>2</sub></b>	<b>77</b>
<b>Summary</b>	<b>95</b>
<b>Samenvatting</b>	<b>99</b>
<b>Acknowledgements</b>	<b>105</b>
<b>Curriculum Vitae</b>	<b>107</b>
<b>List of Publications</b>	<b>109</b>



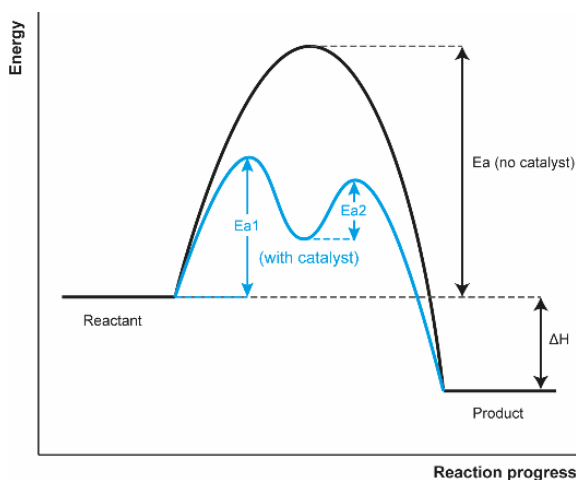
# 1

## Introduction

### 1.1 Heterogeneous catalyst and its multifunctionality

Catalysis is a mechanism by which the rate of chemical reactions can be accelerated by adding a promoting chemical, namely “catalyst,” that is not consumed during the chemical process [1]. The function of a catalyst is to lower the activation energy of the reaction and often provide an alternative reaction pathway without affecting the energy difference between reactant and product, as shown in Figure 1.1. An ideal catalyst should maximize the conversion of reactants, produce only the desired products, and maintain its function for prolonged periods of reaction time [2].

Generally, catalysts are divided into two main classes, depending on their phase compared to reactants or products: homogeneous and heterogeneous catalysts. A homogeneous catalyst is a catalyst in the same phase as the reactants or products. In contrast, a heterogeneous catalyst is in a different phase from the reaction mixture. The most common form of heterogeneous catalyst is solid, while the reactants or products are gases or liquids. This feature leads to the major advantage of heterogeneous catalysts is that the catalyst can be separated from the reaction mixture by simple methods, such as filtration. Thus, solid catalysts can be easily recycled, resulting in low operation costs, which are the key targets of the industrial production processes. Solid catalysts also often exhibit high thermal and mechanical stability, facilitating thus their utilization on large scales. Therefore, heterogeneous catalysts have been widely used in the chemical industry, accounting for approximately 80% of all commercialized catalysts [3].



**Figure 1.1** The effect of a catalyst on the activation energy and pathway of a chemical reaction.

Despite having many advantages, heterogeneous catalysts have some drawbacks. Table 1.1 lists the advantages and disadvantages of homogeneous and heterogeneous catalysts [4]. One of the main fundamental issues for many solid catalysts is the difficulty of controlling the reaction selectivity. Most common solid catalyst materials feature a wide variety of surface species and active sites with varied reactivity, giving rise to diverging reactivity within the same catalyst particle and promoting the formation of undesirable products next to the primary target conversion process. In some cases, such side products strongly bind with the active sites, prevent the regeneration of the active sites for recycling adsorption of the reactants, and thus lead to the deactivation of the catalytic surfaces. Therefore, understanding the role of the surface sites and identifying the reaction or deactivation processes in heterogeneous catalysts is critically important for learning how to control their catalytic activity and selectivity and develop effective catalysts.

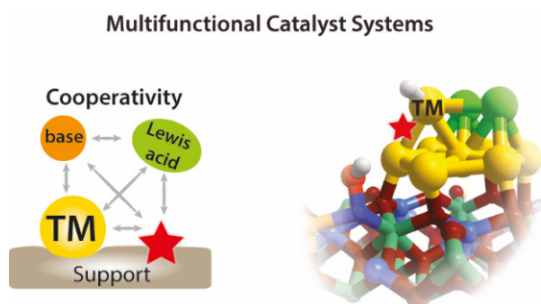
**Table 1.1** An overview of the main advantages and disadvantages of homogeneous and heterogeneous catalysts [4].

	<b>Homogeneous catalyst</b>	<b>Heterogeneous catalyst</b>
Selectivity	High	Low
Catalyst separation and recovery	Difficult and expensive	Easy and cheap
Thermal stability	Low	High
Mass transfer limitations	Very rare	Can be severe
Structure/Mechanism	Defined	Undefined
Applicability	Limited	Wide



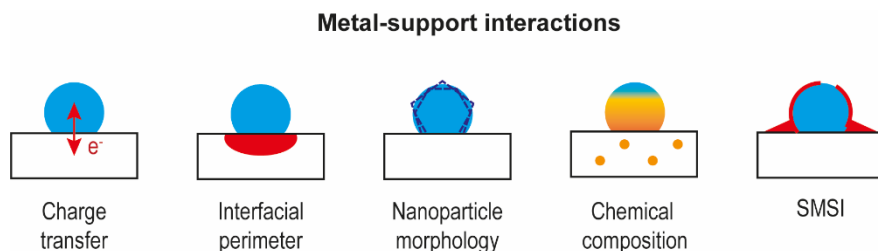
Nevertheless, many different active sites are not necessarily a negative aspect of solid catalysts. In fact, different chemical moieties can exhibit synergistic effects and help promote desirable conversions by forming the so-called “multifunctional catalytic ensembles.” In such a multifunctional system, each catalytic moiety can either work separately to catalyze different elementary reaction steps or work cooperatively to promote the same reaction. Thus, naturally, solid catalysts that exhibit multifunctionality are promising candidates for facilitating multistep reactions. For instance, the tremendous progress in hydrogenation chemistry witnessed in the last decade is related to the developments of multifunctional heterogeneous catalysts [5-7].

Among various solid catalysts, oxide-supported metal catalysts (metal/oxide) have been frequently used and developed in recent years. In such systems, the catalytic phase of transition metals is dispersed on the surface of oxides. The dispersion of metals on oxides initially aims to stabilize the metal nanoparticles and increase the surface area to volume ratio. The attention to such catalysts has been raised since it was found that the oxide support can also influence catalytic performances. The reducible oxides such as  $\text{TiO}_2$ ,  $\text{Fe}_2\text{O}_3$ ,  $\text{CeO}_2$ , and many other transition-metal oxides are particularly attractive for heterogeneous catalyst design. These supports provide versatile and tunable surface characteristics such as surface acidity and basicity. Furthermore, terminal OH groups and surface defects (steps, corners, and vacancies) can act as anchoring sites for metal nanoparticles to boost their dispersion and stabilization of the support surface [8]. For these reasons, the well-defined structure and function are crucial for designing rather complicated and efficient metal/oxide catalysts and understanding their catalytic activity.



**Figure 1.2** Schematic illustration of how different species on the surface can form catalytic ensembles. The synergistic action of the transition metal (TM) centers with the reactive sites of the support, along with the presence of base and Lewis acid promoters, allows for establishing a favorable conversion path for the substrates along the predefined route.

A schematic representation of a cooperative metal/oxide catalyst interface is shown in Figure 1.2. The metals with the reactive sites of the support acting as independent reactive sites or as base and Lewis acid species promoters work cooperatively to catalyze reactions. It should be noted that the reactivity of atoms at the direct contact of metal and oxide support – the interface, is typically different from the other sites. This is due to the synergistic effect between the metal and the oxide support known as the metal-support interactions (MSI) [9, 10]. The MSI comprises several phenomena, such as (i) charge transfer, (ii) interfacial perimeter, (iii) nanoparticle morphology, (iv) chemical composition, and (v) strong metal-support interaction (SMSI), as shown in Figure 1.3.



**Figure 1.3** The five main phenomena of metal-support interactions (MSI).

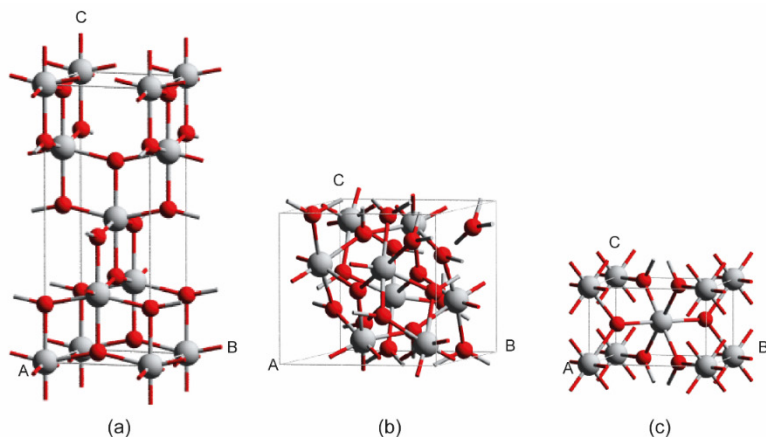
To clarify, (i) the electrons at the interface might be rearranged upon the interaction between metal and oxide, resulting in the charge transfer. (ii) The electron's accumulation and depletion at the interfacial perimeter sites can affect the adsorption/desorption of molecules. (iii) The adhesion energy released from metal-oxide interactions can affect the morphology of metal nanoparticles. (iv) The redox process at metal and oxide support might induce the rearrangement of components and the formation of new phases. (v) The oxide support might be reduced and generate suboxides covering the metal nanoparticle, known as the SMSI [9]. Indeed, such MSI phenomena significantly impact the performance of metal/oxide catalysts by changing their structural and electronic properties [9, 10].

The primary focus of this thesis is on the molecular-level aspects of the MSI and its role in catalysis. For instance, the formation of multifunctional reactive ensembles at the interfacial perimeter and the charge transfer modulate the reactivity of the supported metal particles. Different mechanistic features arising from such MSI phenomena will be demonstrated in the subsequent chapters. Chapters 2 and 5 focus on the reactivity of titania-supported catalysts in the hydrogenation of CO<sub>2</sub> and aromatic amines. Mechanisms of C-H carboxylation reactions will be discussed in Chapters 3 and 4.

## 1.2 TiO<sub>2</sub>-based catalysts

Titanium dioxide (titania or TiO<sub>2</sub>) is one of the most versatile and widely-explored oxide materials used as a catalyst or catalyst support because of its high stability, nontoxicity, and cost-effectiveness [11]. In the context of this thesis, the unique features of titania extend well beyond its excellent ability to disperse the transition metal catalysts nicely in the form of well-defined nanoparticles to a wide range of tuneable MSI phenomena. The catalytic activity of TiO<sub>2</sub> mainly depends on their Lewis acid-base pairs which occur due to the presence of Ti<sup>4+</sup> (Lewis acid) and O<sup>2-</sup> (Lewis base) on the surface. The Brønsted acid (H<sup>+</sup>) can also be introduced to the surface of TiO<sub>2</sub> via the dissociation of H<sub>2</sub>O or H<sub>2</sub> [11-14]. In addition, the deposition of metal nanoparticles on TiO<sub>2</sub> results in the formation of new active sites and, consequently, the changes in the activity and stability of the supported metal/TiO<sub>2</sub> catalyst. All these features are essential to creating highly complex multifunctional ensembles on the surface of TiO<sub>2</sub>-supported metal catalysts, as schematically illustrated in Figure 1.2. The presence of Brønsted acid, Lewis acid, and Lewis base sites on TiO<sub>2</sub> can cooperate with the dispersed metals to enable the selective conversion of various chemical feedstocks.

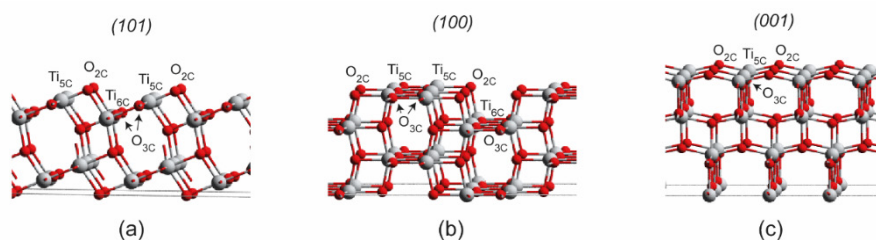
Many studies have shown that both the crystal phase and the exposed surface structure of TiO<sub>2</sub> affect the catalytic properties of titania-based systems [11-14]. TiO<sub>2</sub> can crystallize in one of the three crystalline structures, namely anatase, brookite, and rutile (Figure 1.4). Each of these forms exhibits different physical characteristics, surface properties, and reactivities. Brookite is the least studied TiO<sub>2</sub> due to the difficulty of synthesizing the pure phase. A recent study found that brookite provides a higher activity than other forms of titania in some photocatalytic reactions [13, 15]. The rutile is the most stable and common form of TiO<sub>2</sub>, with the highest density and refractive index [11]. However, it was reported that anatase becomes more stable than rutile when the particle size is smaller than 14 nm [16]. Furthermore, anatase typically exhibits higher photocatalytic activity than rutile [17]. Anatase is also preferred as a metal catalyst support because of its remarkably higher specific surface area [14]. Therefore, from this section onwards, the focus will be put on the anatase TiO<sub>2</sub>.



**Figure 1.4** The bulk crystal structures of **(a)** anatase, **(b)** brookite, and **(c)** rutile  $\text{TiO}_2$ .

The structure, stability and reactivity of anatase  $\text{TiO}_2$  have been studied extensively over decades. The anatase  $\text{TiO}_2$  has a tetragonal lattice ( $P4_2/mnm$ ) with four  $\text{TiO}_2$  units per unit cell (Figure 1.4a). The stability of anatase surfaces can be determined by surface energy calculations. For a series of low-index anatase surfaces, the (101) surface is thermodynamically most stable, followed by the (100), (001), and (110) surfaces, respectively [18-20]. The Wulff construction indicated that over 94% of the exposed surface area of the anatase crystals is represented by the (101) surface, whereas the (001) one is the minority surface having a fraction of about 6% [21].

The (101) surface (Figure 1.5a) contains 5- and 6-coordinated Ti atoms ( $\text{Ti}_{5C}$ ,  $\text{Ti}_{6C}$ ) and 2- and 3-coordinated O atoms ( $\text{O}_{2C}$ ,  $\text{O}_{3C}$ ). This surface has a sawtooth-like appearance, featuring alternating rows of  $\text{Ti}_{5C}$  and  $\text{O}_{2C}$  along the [010] direction. For the (100) surface (Figure 1.5b),  $\text{O}_{2C}$ ,  $\text{O}_{3C}$ , and  $\text{Ti}_{5C}$  atoms are exposed on the outermost layer, while  $\text{Ti}_{6C}$  and  $\text{O}_{3C}$  atoms are at the bottom of the surface. In the case of the (001) surface (Figure 1.5c), the atomic structure is unclear due to its low stability and facile reconstruction. A study based on the add-oxygen model (AOM) method indicated that the surface contains exposed  $\text{O}_{2C}$ ,  $\text{O}_{3C}$ , and  $\text{Ti}_{5C}$  centers [22], as illustrated in Figure 1.5c. An alternative surface structure featuring  $\text{O}_{2C}$  and  $\text{Ti}_{4C}$  exposed atoms was proposed by another literature based on the add-molecule model (ADM) method [23].



**Figure 1.5** The surface morphology of anatase TiO<sub>2</sub> (a) (101), (b) (001), and (c) (100) surfaces.

The exposed Lewis acid-base pairs ( $\text{Ti}^{4+}\text{-O}^{2-}$ ) are commonly considered to contribute to the surface reactivity of pristine TiO<sub>2</sub>. It was reported that the Lewis acidity of  $\text{Ti}^{4+}$  sites on (101) is slightly higher than those on the (001) surface, while the Lewis basicity of  $\text{O}^{2-}$  sites on the (001) is stronger than that on the (101) surface [18, 24]. Several studies on the interaction of small molecules with different anatase surfaces indicated that the most stable (101) surface shows a lower intrinsic reactivity than the other ones. For example, the H<sub>2</sub>O molecule dissociatively adsorbs on the (001) and (110) surfaces, while the molecular adsorption mode is observed on the (101) surface [14]. CO<sub>2</sub> is weakly adsorbed on the (101) surface with a linear configuration, while the formation of a variety of surface carbonates with stronger adsorption energy is observed on the (001) surface [24]. However, when considering the reactivity of supported catalytic ensembles, the dominant (101) surface appears the most relevant for practical catalytic applications.

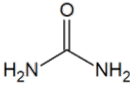
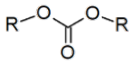
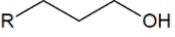
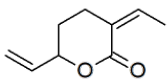

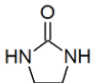
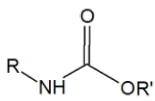
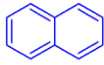
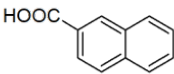
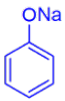
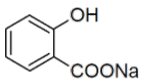
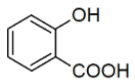

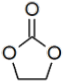
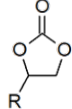
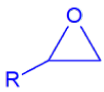
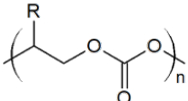
The reactivity of TiO<sub>2</sub> surface can be modified by introducing defects, with oxygen vacancies being the most common type of such surface defects. Removal of an oxygen atom from the surface leaves two excess electrons, which are trapped by the neighboring Ti sites. Thus, two  $\text{Ti}^{4+}$  sites are reduced to two  $\text{Ti}^{3+}$ , providing more electron-rich and reactive transition metal sites. The decreased coordination saturation of the Ti sites near the oxygen vacancy also contributes to the surface Lewis acidity. The formation of such defects can significantly impact the catalytic properties of the titania surface. For instance, the defective TiO<sub>2</sub> (101) surface was found to be more active than the perfect one for the reduction of CO<sub>2</sub> [25]. Besides, the surface oxygen vacancy can act as an anchoring site for the metal nanoparticles. For instance, a highly efficient and durable Pt-based electrocatalyst for oxygen reduction reaction has been prepared by anchoring Pt atoms on TiO<sub>2</sub> containing oxygen vacancies [26].

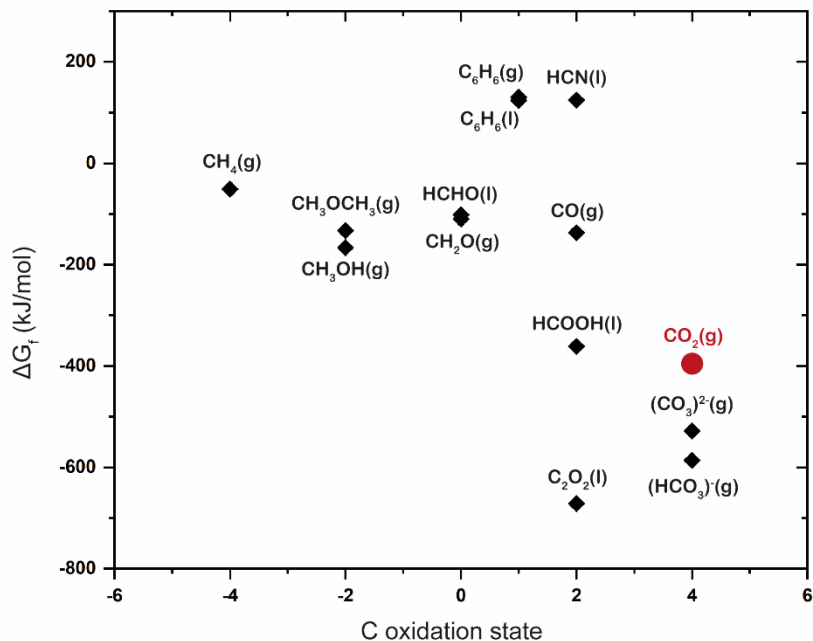
Because of the unique and tunable properties of titania, TiO<sub>2</sub>-based catalysts doped with various transition and non-transition metals have been synthesized and used in exploring different catalytic applications. Depending on the transition metal choice, different reactivity can be introduced to the titania-supported system [27]. For example, Pt/TiO<sub>2</sub> is an exceptional catalyst for the hydrogenation of various organic substrates with molecular H<sub>2</sub> [28]. Au/TiO<sub>2</sub> exhibited remarkable performance for the O<sub>2</sub> activation and the oxidation of organic molecules [29, 30]. Ru/TiO<sub>2</sub> is a promising candidate for the Fisher-Tropsch synthesis [31]. Re/TiO<sub>2</sub> [32] as well as related bimetallic catalysts such as Ni-Re/TiO<sub>2</sub> [33] and Pt-Re/TiO<sub>2</sub> [34] catalysts enabled highly selective reductive transformations of challenging ester substrates. Re/TiO<sub>2</sub> [35], Mo/TiO<sub>2</sub> [36], various metals promoted Co/TiO<sub>2</sub> [37], and other were also found to be uniquely active for the low-temperature and tunable conversions of carbon dioxide to value-added chemicals.

### 1.3 CO<sub>2</sub> conversion to chemicals

CO<sub>2</sub> capture and utilization have been attracting much attention as an important technology helping mitigate global warming and climate change because it could save fossil fuels and lower the CO<sub>2</sub> concentrations in the atmosphere. The utilization of CO<sub>2</sub> can be divided into the following categories: production of chemicals, production of fuels, enhanced biological utilization, and technological utilization that does not require CO<sub>2</sub> conversion [38]. Among them, the conversion of CO<sub>2</sub> to chemicals provides comprehensive benefits to the chemical industry [39]. Table 1.2 represents some of the chemicals that can be produced from CO<sub>2</sub>. The efficient conversion of CO<sub>2</sub> to chemical products is challenging because of its high thermodynamic stability. As illustrated in Figure 1.6, the Gibbs free energy of the CO<sub>2</sub> is lower than its reduction products, such as CO, CH<sub>3</sub>OH, and CH<sub>4</sub>, which can directly be utilized in various downstream applications [38, 40]. Thus, the conversion of CO<sub>2</sub> always requires energy input through the reaction with more energetic reagents [41]. Among various reactive agents used for the conversion of CO<sub>2</sub>, H<sub>2</sub> is the most attractive candidate to offer an opportunity for sustainable development of atom-efficient energy technologies and environmentally benign chemical processes [42].

**Table 1.2** Synthesis of chemicals from CO<sub>2</sub> with various reductants.

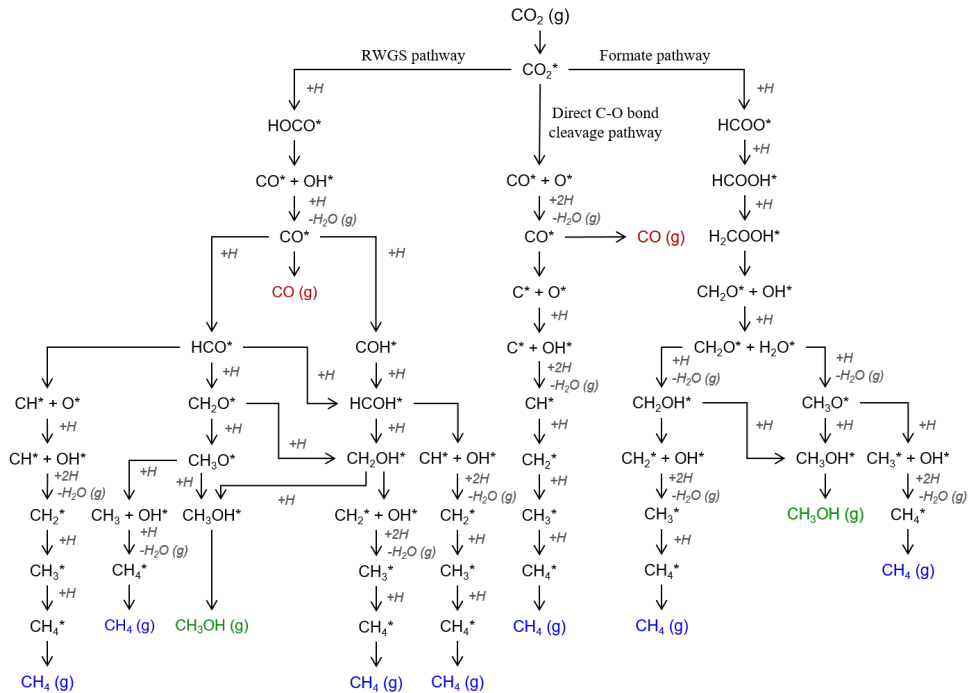
Reductants	Products		
H <sub>2</sub>	HCOOH	CH <sub>3</sub> OH	CH <sub>4</sub>
CH <sub>4</sub>	CO	CH <sub>3</sub> COOH	
NH <sub>3</sub>			
ROH			
Alkenes and Dienes			
Amines	HCONR <sub>2</sub>	R-N=C-O	
			
			
			
			
			



**Figure 1.6** Gibbs free energy of the  $\text{CO}_2$  compared with other chemicals.

The hydrogenation of  $\text{CO}_2$  can be used to produce a variety of chemicals with important downstream applications. In particular, the valorization of  $\text{CO}_2$  to valuable C1 building blocks such as  $\text{CO}$ ,  $\text{CH}_4$ ,  $\text{HCOOH}$ , and  $\text{CH}_3\text{OH}$  attracts much attention from researchers in industry and academia [43, 44]. The catalytic conversion of  $\text{CO}_2$  to such C1 chemicals is governed by three main reaction pathways (Figure 1.7): (1) the reverse water-gas shift (RWGS) pathway, (2) the direct C-O bond cleavage pathway, and (3) the formate pathway [45]. Each reaction pathway proceeds through several elementary steps and reaction intermediates leading to the formation of different products. Because of the complexity of this reaction network, the multifunctional  $\text{TiO}_2$ -supported metal catalyst is a promising candidate for controlling the selectivity of the desired products. However, the promotion of different reaction channels can be anticipated because of various reactive ensembles formed at the multifunctional metal-support interface. Therefore, understanding the fine mechanistic details of these conversion paths over realistic models of supported heterogeneous catalysts may give an insight into the fundamental factors underlying their catalytic behavior.





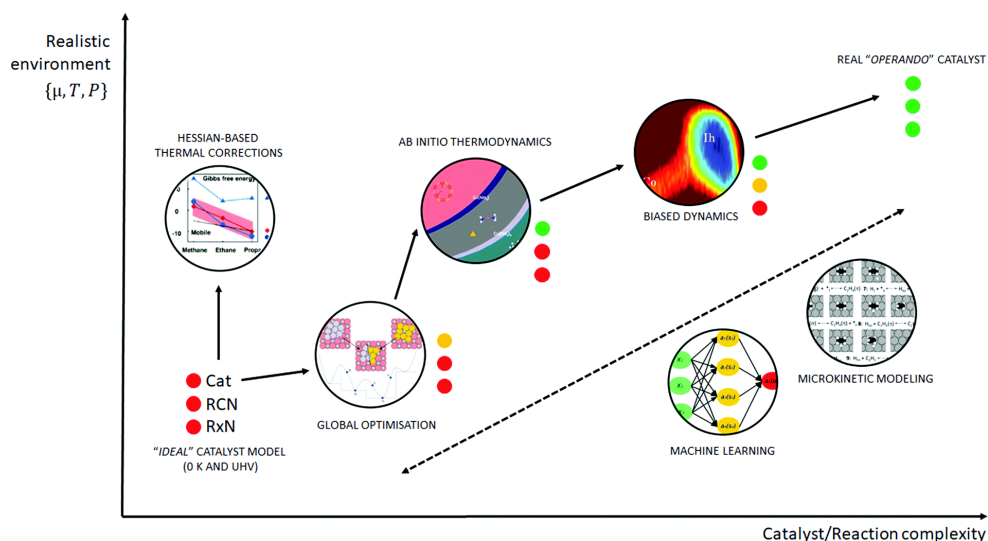
**Figure 1.7** Possible reaction pathways for the hydrogenation of  $\text{CO}_2$ .

Previous computational studies suggested that product selectivity can be determined by the binding strength of key intermediates with the catalytically active sites [45, 46]. The reaction networks in Figure 1.7 suggest that if we aim to design a catalyst with high activity and selectivity for the  $\text{CH}_3\text{OH}$  production, the  $\text{CO}^*$ ,  $\text{HCO}^*$ , and  $\text{CH}_2\text{O}^*$  should be stabilized on the active site to facilitate their further reaction. In contrast, the  $\text{CH}_3\text{O}^*$  should be destabilized to allow its hydrogenation to form  $\text{CH}_3\text{OH}$ . However, the over-stabilization of some intermediates such as  $\text{HCOO}^*$  and  $\text{CO}^*$  might lead to the formation of highly stable resting states that would poison the catalytic surface. The scission of the C-O bond in  $\text{CH}_x\text{O}$  species, which competes with the hydrogenation process, is a critical step for the production of side-product ( $\text{CH}_4$ ).

## 1.4 Computational modeling of complex multifunctional catalyst surfaces

The elucidation of the reaction mechanisms occurring at the active sites on the well-defined catalytic structures is crucial for the rational design of heterogeneous catalysts. In experiments, various spectroscopic methods such as X-ray diffraction/scattering (XRD), X-ray photoelectron spectroscopy (XPS), X-ray absorption spectroscopy (XAS), Raman, infrared spectroscopy (IR), transmission electron microscopy (TEM), and other methods have been performed to study what happens under reaction conditions [47]. It was found that the catalytic structures can change dramatically when exposed to reaction conditions or during chemical transformations. Furthermore, adsorbed species and dynamics at high temperatures and pressure can cause the restructuring of surfaces. These phenomena might lead to the formation of new functionalities or active sites that are not present before the reaction begins. Thus, identifying the real active sites and monitoring the catalytic processes under realistic working conditions are the persistent challenges in catalysis research. Fortunately, modern computational chemistry can help address them by giving insight into more details of the catalytic structure and its activities at the atomistic level.

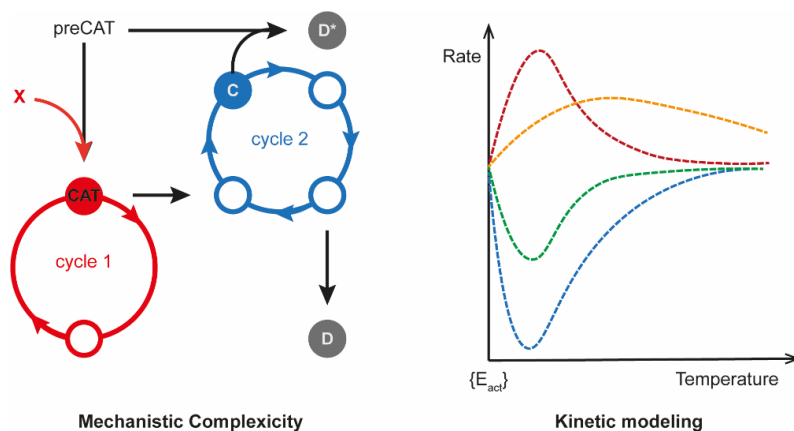
In computational catalysis, theoretical calculations based on quantum chemical approaches, particularly the density functional theory (DFT), have been widely used as fundamental tools for understanding the catalytic processes [48-52]. Traditionally, the reaction mechanisms were explored within the concept of potential energy surface (PES), corresponding to simplified catalytic models under ultrahigh vacuum and at 0 K (OK/UHV). However, in the real system, catalysts usually operate under ambient or higher temperatures and pressures. Furthermore, the multifunctions of heterogeneous catalysts and the chemical transformations during the reaction raise issues of structural complexity that are difficult to model. Thus, the development of computational heterogeneous catalysis is currently evolving into studying the catalytic processes using models representing the conditions and environments encountered under realistic working conditions, in other words, *operando* conditions.



**Figure 1.8** Schematic of the various computational methods applied to heterogeneous catalysis lies between an idealized UHV model and a realistic *operando* model. The traffic light depicts the quality of each method with respect to catalyst model complexity (Cat), reaction coordinate accuracy (RCN), and reaction network complexity (RxN) [48].

So far, many computational methods have been used to extend the conventional static models based on the 0 K/UHV to the *operando* conditions. Figure 1.8 illustrates a transition from 0K/UHV to *operando* conditions enabled by the introduction of four key computational methods [48]: (1) global optimization techniques, (2) ab initio constrained thermodynamics, (3) biased molecular dynamics simulations, (4) microkinetic modeling. The reaction environment (e.g., chemical potentials and temperature) becomes more realistic from the bottom to the top of the figure. At the same time, the development of computational methods results in the increased complexity of the catalytic system from left to right. Following such information, global optimization techniques are performed to screen candidate structures and search for stable active site formation. The ab initio thermodynamics can determine the thermodynamic stabilities of different active sites ensembles under varying reaction conditions, while the ab initio MD can identify the dynamic structures in environments with an explicit solvent or high reactant concentrations. Microkinetic modeling provides kinetic information from the known intermediates and reaction pathways that build up the reaction network [48, 53]. In addition, machine learning (ML) techniques can be used to assist in catalytic modeling, discovery, and prediction of chemicals with desired properties and prediction of reaction pathways without human biases [54-56].

In this thesis, the DFT calculations were employed together with the microkinetic modeling (MKM) to understand the catalytic processes. The MKM was used to reduce the complexity of the DFT-computed reaction networks and translate the atomistic details of molecular mechanisms into experimentally-measurable kinetic parameters, as schematically illustrated in Figure 1.9. Combining those two methods can identify the optimal reaction conditions so that the desired reaction pathway is enabled, resulting in the enhanced selectivity of the overall catalytic process. The general concepts and basics of each of these methods are briefly described in the following sections.



**Figure 1.9** A principle scheme of the hierarchical modeling strategy within this thesis

### 1.4.1 Density functional theory (DFT)

Computational modeling based on density functional theory (DFT) has been a powerful research tool for analyzing spectroscopic data, modeling catalysts, and studying reaction mechanisms. By applying DFT, the electronic properties of a many-electron system (atoms, molecules, and materials) are determined by using functionals of the electronic charge density, which can be written as [57]:

$$\rho(r) = N \iint \cdots \int |\psi(r_1, r_2 \cdots r_N)|^2 ds dx_2 \cdots dx_N \quad (1)$$

where  $\rho(r)$  is the total electronic density and  $\psi(r_1, r_2 \cdots r_N)$  is the N-electron wave function.

The foundation of the DFT has been laid by the seminal work of Hohenberg and Kohn [58], which demonstrated formally that any ground state property of a system is a function of its electron density. However, this approach is not sufficient to calculate the actual electronic motion state. Kohn and Sham [59] extended this

theory to practice by using the electron-electron interaction potential of the density functional to obtain the lowest energy and the corresponding molecular orbitals and orbital energies. The overall energy functional can be written as follows:

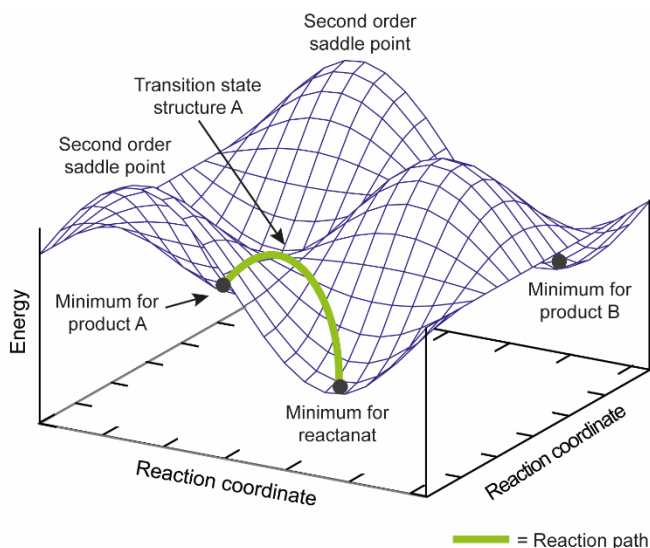
$$E[\rho] = E^K[\rho] + E^V[\rho] + E^J[\rho] + E^{XC}[\rho] \quad (2)$$

where  $E^K[\rho]$  is the kinetic energy of the electrons,  $E^V[\rho]$  is the nuclear-electron attraction energy,  $E^J[\rho]$  is the electron-electron repulsion energy, and  $E^{XC}[\rho]$  is the exchange-correlation potential energy (electron-electron interaction).

Based on this approach, the exact energy of the system could in principle be obtained from the exact electron density. Unfortunately, the exact form of the exchange-correlation functional is not known, and various approximations and fitting procedures have been proposed to derive different practically approximated DFT methodologies. Various approximate exchange-correlation functionals such as local density approximation (LDA), generalized gradient approximation (GGA), metal-GGA (mGGA), and hybrid-GGA (hGGA) have been applied for the density functional development. These methods have been described in detail elsewhere [ref]. In computational catalysis, the GGA is preferred over the LDA due to its minor errors of  $\pm 20$  kJ/mol for adsorption and reaction energies [60, 61]. Among the GGA family, the mGGA produces much better electron densities, and hGGA shows the best performance in terms of accuracy [62].

#### 1.4.2 Potential energy surface (PES)

Modeling the mechanism of chemical reactions requires the analysis of energetic and structural information of reactants, products, and intermediates occurring during the reaction. In that regard, the concept of potential energy surface (PES), a hyperdimensional energy surface as a function of geometric coordination [63], has been applied to the DFT calculations for studying the reaction mechanisms. A simple schematic PES is illustrated in Figure 1.10, similar to a hilly landscape composed of valleys, mountain passes, and peaks. Compared to a chemical reaction, the mountain passes are the reaction pathways. The valleys or minimum points are reactants, products, or intermediates, while the peaks or saddle points are transition state structures of the reaction. Thus, the shortest mountain pass between two valleys corresponding to reactant and product is the most preferred reaction pathway of the overall reaction.



**Figure 1.10** Model potential energy surface (PES) showing minima, transition state, a second-order saddle point, and reaction path.

Typically, the exploration of PES for any catalytic process involves the following steps: (1) identify/propose the active site(s), (2) predict/propose reaction mechanisms, (3) optimize candidate structures and calculate their electronic energy, (4) identify stationary points on the PES and locate the local minima and transition states connecting them to form reaction pathways, and finally (5) include temperature and pressure effects for obtaining the Gibbs free energy [49].

### 1.4.3 Microkinetic modeling (MKM)

The very high mechanistic complexity is one of the key challenges in closing the gap between the theoretical models and the experimental *operando* characterization of the catalytic systems. In practice, even the simplest catalytic process involves complex networks of competing and parallel multistep reaction channels taking place at different sites. The overall catalytic behavior is defined by the relative rates of each of the pathways leading to various intermediates and products, which in turn, are determined both by the intrinsic properties of the reactive ensembles and the conditions of the catalytic reactions. The DFT calculations enable the direct calculations of the rate constant of the individual reaction steps with sufficiently high accuracy. The resulting fine mechanistic details need to be further reduced to bridge the microscopic insights into the elementary steps and the macroscopic kinetics and measurable parameters of the catalytic processes.

The first principle-based kinetic modeling can be used to predict the activity of catalysts. Such models link the detailed microscopic insights into the catalytic reaction obtained from various computational approaches with the observable macroscopic kinetics of the reaction process. By reducing the mechanistic complexity, such kinetic models allow to point out computationally the abundant reaction intermediates or the composition of the catalyst under the specific reaction conditions. The resulting information on the preferred reaction pathway and the influence of the reaction conditions on catalyst behavior can be used for the *in silico* design of improving practical catalyst systems [48, 52]. The most popular approach to such kinetic models is the mean-field microkinetic modeling. In this approach, the reaction kinetics is described by using a macroscopic rate equation in which the surface state is represented by the coverage vector, as shown in the following equation

$$\left( \frac{d\theta_i}{dt} = \sum_j v_{ij} r_j f_j(\theta_1, \dots, \theta_N) \right)_{i=1-N} \quad (3)$$

where,  $\theta_i$  is the surface coverage of species  $i$  at time  $t$ ,  $v_{ij}$  is the stoichiometric coefficient for species  $i$  in step  $j$ ,  $r_j$  is the rate of reaction  $j$  and  $f_i$  is a function of several coverages involved in step  $j$ . The adsorbates are assumed uncorrelated. This system of differential equations effectively describes all chemical processes taking place in the catalytic system. However, this approximation does not include the effect of spatial correlations in the distribution of reactants on the catalyst surface as well as the lateral interactions among adsorbates. The kinetic Monte Carlo method can be performed to solve that problems, but beyond the scope of my study.

The transition state theory (TST) and the DFT data can be applied to equation (3) for obtaining the rate constant, as shown in equation (4)

$$k_a = A_e \exp\left(\frac{-\Delta E_a}{k_B T}\right) \quad (4)$$

where the prefactor  $A_e$  accounts for the entropic changes between the initial and transition state of the elementary reaction and  $\Delta E_a$  is the corresponding intrinsic activation energy barrier.

Besides, the apparent activation energy ( $E_a^{ap}$ ) can be computed from the following equation:

$$E_a^{app} = k_B T^2 \left( \frac{\partial \ln(r_t)}{\partial T} \right)_P \quad (5)$$

In addition, the rate constant of the adsorption reaction can be calculated by the Hertz-Knudsen equation [64]:

$$k_{ads} = \frac{PA}{\sqrt{2\pi mk_b T}} S \quad (6)$$

where  $k_{ads}$  is the rate constant of adsorption reaction,  $P$  is the partial pressure of the adsorbate in the gas phase,  $A$  is the surface area of the adsorption site,  $m$  is the mass of adsorbate,  $k_b$  is the Boltzmann constant,  $T$  is the temperature, and  $S$  is the sticking coefficient.

The desorption reaction is calculated by the following equation:

$$k_{des} = \frac{k_b T^3}{h^3} \frac{A(2\pi mk_b)}{\sigma \theta_{rot}} e^{\left( \frac{-E_{des}}{k_b T} \right)} \quad (7)$$

where  $k_{des}$  is the rate constant of desorption reaction,  $h$  is the Plank's constant,  $\sigma$  is the symmetry number of a molecule,  $\theta_{rot}$  is the rotational temperature of a molecule, and  $E_{des}$  is the desorption energy.

The differential equations are constructed using the rate constants and the set of elementary reaction steps. For each of the  $M$  components in the kinetic network, a single differential equation is in the form:

$$r_i = \sum_{j=1}^N \left( k_j v_i^j \prod_{k=1}^M c_k^{v_k^j} \right) \quad (8)$$

where  $r_i$  is the rate reaction,  $k_j$  is the elementary reaction constant,  $v_i^j$  is the stoichiometric coefficient of component  $i$  in elementary reaction step  $k$  and  $c_k$  is the concentration of component  $k$  on the catalytic surface.

The rate-determining step of the overall reaction can be identified by using the degree of the rate control (DRC) parameter as shown in the following equation [65-67]:

$$X_{RC,i} = \left[ \frac{\partial \ln(r_t)}{\partial \ln(k_i)} \right]_{k_j \neq i, K_i} \quad (9)$$

The DRC is a weighing factor that directly relates such macroscopic rate parameters as the apparent activation energy and reaction orders and the



microscopic characteristic as the elementary reaction rates and activation barriers for elementary steps.

## 1.5 Scope of the thesis

The aim of this thesis is to investigate the role of multifunctional ensembles on the catalytic behaviour of TiO<sub>2</sub>-supported catalysts by means of DFT calculations. Particular emphasis is placed on the catalytic reactivity at the perimeter of metal-TiO<sub>2</sub> interface. Here, CO<sub>2</sub> reduction and nitrile hydrogenation are selected as the model representative and industrially relevant catalytic processes. Furthermore, I try to extend the DFT calculations from classical computational methods, based on inspection of the potential energy surface at 0 K and low reactant concentrations (OK/UHV model) towards the operando conditions by using the microkinetic modeling (MKM).

Chapter 2 investigates computationally the CO<sub>2</sub> hydrogenation to CH<sub>3</sub>OH on a Cd<sub>4</sub>/TiO<sub>2</sub> catalyst. This catalyst system has been discovered by our experimental collaborators as a highly selective and exceptionally active CO<sub>2</sub> reduction catalyst. This chapter is devoted to rationalizing the unique reactivity of this system. The main aim of my computational work was to explore the multiple-site cooperation effects on the mechanism and energetics of various CO<sub>2</sub> reduction paths to construct a detailed molecular-level picture of the complex reaction pathways on the catalyst surface. The resulting mechanistic insights were used to construct an MKM that was used to analyze the reaction networks at the relevant experimental conditions and construct the direct links with the experimental findings.

Chapter 3 discusses the mechanistic role of K<sub>2</sub>CO<sub>3</sub> dispersed over defective TiO<sub>2</sub> support (K<sub>2</sub>CO<sub>3</sub>/TiO<sub>2</sub>) for the esterification of benzene with CO<sub>2</sub> and CH<sub>3</sub>OH, recently discovered experimentally. DFT calculations specifically addressed the role of the adsorbed K<sub>2</sub>CO<sub>3</sub> for CO<sub>2</sub> activation and the fast deactivation of bare defective TiO<sub>2</sub>. An important message in this chapter resonating with some of the conclusions from Chapter 2 is that catalyst enhancement can be achieved through inhibition of some thermodynamically highly favourable reaction channels giving rise to the formation of resting states and effective surface poisoning rather than promoting the desirable chemical conversions. Minimizing side reactions and deactivation pathways is at least as promising strategy as the more common reactivity enhancement towards the desirable ones for catalyst development and optimization.

Chapter 4 builds up on the mechanistic study of the Chapter 3 and analyses whether this exciting catalytic chemistry enable by non-critical metal-based catalysts only can be used to convert more challenging and abundant substrates. Based on the excellent performance of  $\text{K}_2\text{CO}_3/\text{TiO}_2$  catalyst in the carboxylation of the C-H bonds in benzene, we hypothesized that a similar mechanism could potentially be realized when using  $\text{CH}_4$  as an alternative reactant. Potentially, this reaction could provide a route for the efficient valorization of natural gas and simultaneous  $\text{CO}_2$  utilization. The DFT calculations presented in this chapter focus on providing insight into the mechanistic challenges associated with such a transformation and highlight the differences in reactivity of benzene and  $\text{CH}_4$ , particularly for the key C-C coupling reaction with  $\text{CO}_2$ .

Chapter 5 further explores the models and mechanistic concepts developed in the preceding chapters for providing a mechanistic explanation for the high reactivity and selectivity of  $\text{Au}/\text{TiO}_2$  catalyst for the direct hydrogenation of benzonitrile to benzylamine, recently discovered by our experimental collaborators. To rationalize the experimental observations, the reaction mechanism was studied in detail by using  $\text{Au}_{13}$  clusters supported on a rutile  $\text{TiO}_2$  surface as a model. The effect of  $\text{Au}_{13}$  cluster geometries on the catalytic reactivity is discussed. This study highlights the critical role of the multifunctional reaction environment at the metal-support interface for establishing a highly selective and efficient reduction of this challenging biomass-derived substrate. The proposed reaction mechanism consists of heterolytic  $\text{H}_2$  dissociation at the  $\text{Au}-\text{TiO}_2$  interface and the subsequent four consecutive  $\text{H}^+$  and  $\text{H}^-$  transfer reaction steps involving the additional nitrile substrate activation by the Lewis acidic sites of the  $\text{TiO}_2$  support. This chapter emphasizes and clarifies the role of each reactive center and their cooperation within the catalytic ensemble formed at the  $\text{Au}-\text{TiO}_2$  interface.

## References

1. Wilhelm Ostwald – Nobel Lecture: On Catalysis. <https://www.nobelprize.org/prizes/chemistry/1909/ostwald/lecture/>. 1909 [cited 2022, 2 Sep].
2. Védrine, J.C., *1 - Fundamentals of heterogeneous catalysis*, in *Metal Oxides in Heterogeneous Catalysis*, J.C. Védrine, Editor. 2018, Elsevier. p. 1-41.
3. Védrine, J.C., *Metal Oxides in Heterogeneous Oxidation Catalysis: State of the Art and Challenges for a More Sustainable World*. *ChemSusChem*, 2019. **12**(3): p. 577-588.

4. Fadhel, A.Z., P. Pollet, C.L. Liotta, and C.A. Eckert, *Combining the Benefits of Homogeneous and Heterogeneous Catalysis with Tunable Solvents and Nearcritical Water*. *Molecules*, 2010. **15**(11): p. 8400-8424.
5. Pritchard, J., G.A. Filonenko, R. van Putten, E.J.M. Hensen, and E.A. Pidko, *Heterogeneous and homogeneous catalysis for the hydrogenation of carboxylic acid derivatives: history, advances and future directions*. *Chem. Soc. Rev.*, 2015. **44**(11): p. 3808-3833.
6. Tamura, M., R. Tamura, Y. Takeda, Y. Nakagawa, and K. Tomishige, *Catalytic hydrogenation of amino acids to amino alcohols with complete retention of configuration*. *Chem. Commun.*, 2014. **50**(50): p. 6656-6659.
7. Wang, Y., Y. Shen, Y. Zhao, J. Lv, S. Wang, and X. Ma, *Insight into the Balancing Effect of Active Cu Species for Hydrogenation of Carbon–Oxygen Bonds*. *ACS Catal.*, 2015. **5**(10): p. 6200-6208.
8. Lang, R., X. Du, Y. Huang, X. Jiang, Q. Zhang, Y. Guo, K. Liu, B. Qiao, A. Wang, and T. Zhang, *Single-Atom Catalysts Based on the Metal–Oxide Interaction*. *Chem. Rev.*, 2020. **120**(21): p. 11986-12043.
9. van Deelen, T.W., C. Hernández Mejía, and K.P. de Jong, *Control of metal-support interactions in heterogeneous catalysts to enhance activity and selectivity*. *Nat. Catal.*, 2019. **2**(11): p. 955-970.
10. Li, Y., Y. Zhang, K. Qian, and W. Huang, *Metal–Support Interactions in Metal/Oxide Catalysts and Oxide–Metal Interactions in Oxide/Metal Inverse Catalysts*. *ACS Catal.*, 2022. **12**(2): p. 1268-1287.
11. Oi, L.E., M.-Y. Choo, H.V. Lee, H.C. Ong, S.B.A. Hamid, and J.C. Juan, *Recent advances of titanium dioxide (TiO<sub>2</sub>) for green organic synthesis*. *RSC Adv.*, 2016. **6**(110): p. 108741-108754.
12. Wu, L., C. Fu, and W. Huang, *Surface chemistry of TiO<sub>2</sub> connecting thermal catalysis and photocatalysis*. *Phys. Chem. Chem. Phys.*, 2020. **22**(18): p. 9875-9909.
13. De Angelis, F., C. Di Valentin, S. Fantacci, A. Vittadini, and A. Selloni, *Theoretical Studies on Anatase and Less Common TiO<sub>2</sub> Phases: Bulk, Surfaces, and Nanomaterials*. *Chem. Rev.*, 2014. **114**(19): p. 9708-9753.
14. Bourikas, K., C. Kordulis, and A. Lycourghiotis, *Titanium Dioxide (Anatase and Rutile): Surface Chemistry, Liquid–Solid Interface Chemistry, and Scientific Synthesis of Supported Catalysts*. *Chem. Rev.*, 2014. **114**(19): p. 9754-9823.
15. Kandiel, T.A., L. Robben, A. Alkaim, and D. Bahnemann, *Brookite versus anatase TiO<sub>2</sub> photocatalysts: phase transformations and photocatalytic activities*. *Photochem. Photobiol. Sci.*, 2013. **12**(4): p. 602-609.
16. Zhang, H. and J. F. Banfield, *Thermodynamic analysis of phase stability of nanocrystalline titania*. *J. Mater. Chem.*, 1998. **8**(9): p. 2073-2076.

17. Luttrell, T., S. Halpegamage, J. Tao, A. Kramer, E. Sutter, and M. Batzill, *Why is anatase a better photocatalyst than rutile? - Model studies on epitaxial TiO<sub>2</sub> films*. *Sci. Rep.*, 2014. **4**(1): p. 4043.
18. Mino, L., A.M. Ferrari, V. Lacivita, G. Spoto, S. Bordiga, and A. Zecchina, *CO Adsorption on Anatase Nanocrystals: A Combined Experimental and Periodic DFT Study*. *J. Phys. Chem. C*, 2011. **115**(15): p. 7694-7700.
19. Esch, T.R., I. Gadaczek, and T. Bredow, *Surface structures and thermodynamics of low-index of rutile, brookite and anatase – A comparative DFT study*. *Appl. Surf. Sci.*, 2014. **288**: p. 275-287.
20. Arrouvel, C., M. Digne, M. Breyse, H. Toulhoat, and P. Raybaud, *Effects of morphology on surface hydroxyl concentration: a DFT comparison of anatase–TiO<sub>2</sub> and  $\gamma$ -alumina catalytic supports*. *J. Catal.*, 2004. **222**(1): p. 152-166.
21. Lazzeri, M., A. Vittadini, and A. Selloni, *Structure and energetics of stoichiometric TiO<sub>2</sub> anatase surfaces*. *Phys. Rev. B*, 2001. **63**(15): p. 155409.
22. Wang, Y., H. Sun, S. Tan, H. Feng, Z. Cheng, J. Zhao, A. Zhao, B. Wang, Y. Luo, J. Yang, and J.G. Hou, *Role of point defects on the reactivity of reconstructed anatase titanium dioxide (001) surface*. *Nat. Commun.*, 2013. **4**(1): p. 2214.
23. Lazzeri, M. and A. Selloni, *Stress-driven reconstruction of an oxide surface: The anatase TiO<sub>2</sub>(001)-(1 $\times$ 4) surface*. *Phys. Rev. Lett.*, 2001. **87**(26): p. 266105-1.
24. Mino, L., G. Spoto, and A.M. Ferrari, *CO<sub>2</sub> Capture by TiO<sub>2</sub> Anatase Surfaces: A Combined DFT and FTIR Study*. *J. Phys. Chem. C*, 2014. **118**(43): p. 25016-25026.
25. Ji, Y. and Y. Luo, *New Mechanism for Photocatalytic Reduction of CO<sub>2</sub> on the Anatase TiO<sub>2</sub>(101) Surface: The Essential Role of Oxygen Vacancy*. *J. Am. Chem. Soc.*, 2016. **138**(49): p. 15896-15902.
26. Chen, Y., J. Chen, J. Zhang, Y. Xue, G. Wang, and R. Wang, *Anchoring Highly Dispersed Pt Electrocatalysts on TiO<sub>x</sub> with Strong Metal–Support Interactions via an Oxygen Vacancy-Assisted Strategy as Durable Catalysts for the Oxygen Reduction Reaction*. *Inorg. Chem.*, 2022. **61**(12): p. 5148-5156.
27. Bagheri, S., N. Muhd Julkapli, and S. Bee Abd Hamid, *Titanium Dioxide as a Catalyst Support in Heterogeneous Catalysis*. *Sci. World J.*, 2014. **2014**: p. 727496.
28. Macino, M., A.J. Barnes, S.M. Althahban, R. Qu, E.K. Gibson, D.J. Morgan, S.J. Freakley, N. Dimitratos, C.J. Kiely, X. Gao, A.M. Beale, D. Bethell, Q. He, M. Sankar, and G.J. Hutchings, *Tuning of catalytic sites in Pt/TiO<sub>2</sub> catalysts for the chemoselective hydrogenation of 3-nitrostyrene*. *Nat. Catal.*, 2019. **2**(10): p. 873-881.

29. Panayotov, D.A., A.I. Frenkel, and J.R. Morris, *Catalysis and Photocatalysis by Nanoscale Au/TiO<sub>2</sub>: Perspectives for Renewable Energy*. *ACS Energy Lett.*, 2017. **2**(5): p. 1223-1231.
30. Huang, J., S. He, J.L. Goodsell, J.R. Mulcahy, W. Guo, A. Angerhofer, and W.D. Wei, *Manipulating Atomic Structures at the Au/TiO<sub>2</sub> Interface for O<sub>2</sub> Activation*. *J. Am. Chem. Soc.*, 2020. **142**(14): p. 6456-6460.
31. Zhang, Y., X. Su, L. Li, H. Qi, C. Yang, W. Liu, X. Pan, X. Liu, X. Yang, Y. Huang, and T. Zhang, *Ru/TiO<sub>2</sub> Catalysts with Size-Dependent Metal/Support Interaction for Tunable Reactivity in Fischer–Tropsch Synthesis*. *ACS Catal.*, 2020. **10**(21): p. 12967-12975.
32. Toyao, T., S.M.A.H. Siddiki, A.S. Touchy, W. Onodera, K. Kon, Y. Morita, T. Kamachi, K. Yoshizawa, and K.-i. Shimizu, *TiO<sub>2</sub>-Supported Re as a General and Chemoselective Heterogeneous Catalyst for Hydrogenation of Carboxylic Acids to Alcohols*. *Eur. J. Chem.*, 2017. **23**(5): p. 1001-1006.
33. Liu, K., J. Pritchard, L. Lu, R. van Putten, M.W.G.M. Verhoeven, M. Schmitkamp, X. Huang, L. Lefort, C.J. Kiely, E.J.M. Hensen, and E.A. Pidko, *Supported nickel–rhenium catalysts for selective hydrogenation of methyl esters to alcohols*. *Chem. Commun.*, 2017. **53**(70): p. 9761-9764.
34. Pritchard, J., A. Ciftci, M.W.G.M. Verhoeven, E.J.M. Hensen, and E.A. Pidko, *Supported Pt-Re catalysts for the selective hydrogenation of methyl and ethyl esters to alcohols*. *Catal. Today*, 2017. **279**: p. 10-18.
35. Ting, K.W., T. Toyao, S.M.A.H. Siddiki, and K.-i. Shimizu, *Low-Temperature Hydrogenation of CO<sub>2</sub> to Methanol over Heterogeneous TiO<sub>2</sub>-Supported Re Catalysts*. *ACS Catal.*, 2019. **9**(4): p. 3685-3693.
36. Len, T., M. Bahri, O. Ersen, Y. Lefkir, L. Cardenas, I.J. Villar-Garcia, V. Pérez Dieste, J. Llorca, N. Perret, R. Checa, E. Puzenat, P. Afanasiev, F. Morfin, and L. Piccolo, *Ultradispersed Mo/TiO<sub>2</sub> catalysts for CO<sub>2</sub> hydrogenation to methanol*. *Green Chem.*, 2021. **23**(18): p. 7259-7268.
37. Li, W., G. Zhang, X. Jiang, Y. Liu, J. Zhu, F. Ding, Z. Liu, X. Guo, and C. Song, *CO<sub>2</sub> Hydrogenation on Unpromoted and M-Promoted Co/TiO<sub>2</sub> Catalysts (M = Zr, K, Cs): Effects of Crystal Phase of Supports and Metal–Support Interaction on Tuning Product Distribution*. *ACS Catal.*, 2019. **9**(4): p. 2739-2751.
38. Aresta, M., A. Dibenedetto, and A. Angelini, *Catalysis for the Valorization of Exhaust Carbon: from CO<sub>2</sub> to Chemicals, Materials, and Fuels. Technological Use of CO<sub>2</sub>*. *Chem. Rev.*, 2014. **114**(3): p. 1709-1742.
39. Tabanelli, T., D. Bonincontro, S. Albonetti, and F. Cavani, *Chapter 7 - Conversion of CO<sub>2</sub> to Valuable Chemicals: Organic Carbonate as Green Candidates for the Replacement of Noxious Reactants*, in *Studies in Surface Science and Catalysis*, S. Albonetti, S. Perathoner, and E.A. Quadrelli, Editors. 2019, Elsevier. p. 125-144.

40. Song, C., *Global challenges and strategies for control, conversion and utilization of CO<sub>2</sub> for sustainable development involving energy, catalysis, adsorption and chemical processing*. *Catal. Today*, 2006. **115**(1): p. 2-32.
41. Li, W., H. Wang, X. Jiang, J. Zhu, Z. Liu, X. Guo, and C. Song, *A short review of recent advances in CO<sub>2</sub> hydrogenation to hydrocarbons over heterogeneous catalysts*. *RSC Adv.*, 2018. **8**(14): p. 7651-7669.
42. Wang, W., S. Wang, X. Ma, and J. Gong, *Recent advances in catalytic hydrogenation of carbon dioxide*. *Chem. Soc. Rev.*, 2011. **40**(7): p. 3703-3727.
43. Jangam, A., S. Das, N. Dewangan, P. Hongmanorom, W.M. Hui, and S. Kawi, *Conversion of CO<sub>2</sub> to C1 chemicals: Catalyst design, kinetics and mechanism aspects of the reactions*. *Catal. Today*, 2020. **358**: p. 3-29.
44. Alam, M.I., R. Cheula, G. Moroni, L. Nardi, and M. Maestri, *Mechanistic and multiscale aspects of thermo-catalytic CO<sub>2</sub> conversion to C<sub>1</sub> products*. *Catal. Sci. Technol.*, 2021. **11**(20): p. 6601-6629.
45. Kattel, S., P. Liu, and J.G. Chen, *Tuning Selectivity of CO<sub>2</sub> Hydrogenation Reactions at the Metal/Oxide Interface*. *J. Am. Chem. Soc.*, 2017. **139**(29): p. 9739-9754.
46. Li, Y., S.H. Chan, and Q. Sun, *Heterogeneous catalytic conversion of CO<sub>2</sub>: a comprehensive theoretical review*. *Nanoscale*. **7**(19): p. 8663-8683.
47. Zhu, Y., J. Wang, H. Chu, Y.-C. Chu, and H.M. Chen, *In Situ/Operando Studies for Designing Next-Generation Electrocatalysts*. *ACS Energy Lett.*, 2020. **5**(4): p. 1281-1291.
48. Grajciar, L., C.J. Heard, A.A. Bondarenko, M.V. Polynski, J. Meeprasert, E.A. Pidko, and P. Nachtigall, *Towards operando computational modeling in heterogeneous catalysis*. *Chem. Soc. Rev.*, 2018. **47**(22): p. 8307-8348.
49. Morales-García, Á., F. Viñes, J.R.B. Gomes, and F. Illas, *Concepts, models, and methods in computational heterogeneous catalysis illustrated through CO<sub>2</sub> conversion*. *Wiley Interdiscip. Rev. Comput. Mol. Sci.*, 2021. **11**(4): p. e1530.
50. Eisenstein, O. and S. Shaik, *Computational Catalysis: A Land of Opportunities*. *Top. Catal.*, 2022. **65**(1): p. 1-5.
51. Studt, F., *Grand Challenges in Computational Catalysis*. *Front. Catal.*, 2021. **1**: p. 658965.
52. Chen, B.W.J., L. Xu, and M. Mavrikakis, *Computational Methods in Heterogeneous Catalysis*. *Chem. Rev.*, 2021. **121**(2): p. 1007-1048.
53. Shi, X., X. Lin, R. Luo, S. Wu, L. Li, Z.-J. Zhao, and J. Gong, *Dynamics of Heterogeneous Catalytic Processes at Operando Conditions*. *JACS Au*, 2021. **1**(12): p. 2100-2120.
54. Keith, J.A., V. Vassilev-Galindo, B. Cheng, S. Chmiela, M. Gastegger, K.-R. Müller, and A. Tkatchenko, *Combining Machine Learning and*

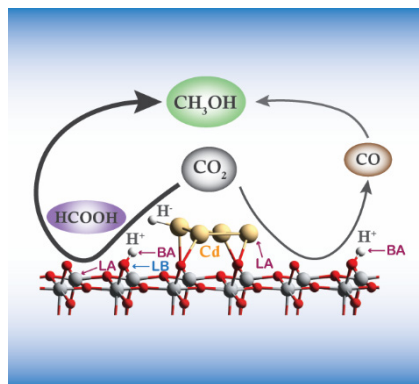
- Computational Chemistry for Predictive Insights Into Chemical Systems. Chem. Rev.*, 2021. **121**(16): p. 9816-9872.
55. Ma, S. and Z.-P. Liu, *Machine Learning for Atomic Simulation and Activity Prediction in Heterogeneous Catalysis: Current Status and Future. ACS Catal.*, 2020. **10**(22): p. 13213-13226.
  56. Yang, W., T.T. Fidelis, and W.-H. Sun, *Machine Learning in Catalysis, From Proposal to Practicing. ACS Omega*, 2020. **5**(1): p. 83-88.
  57. Blinder, S.M., *Chapter 14 - Density functional theory*, in *Introduction to Quantum Mechanics (Second Edition)*, S.M. Blinder, Editor. 2021, Academic Press: San Diego. p. 235-244.
  58. Hohenberg, P. and W. Kohn, *Inhomogeneous electron gas. Phys. Rev.*, 1964. **136**(3B): p. B864-B871.
  59. Kohn, W. and L.J. Sham, *Self-Consistent Equations Including Exchange and Correlation Effects. Phys. Rev.*, 1965. **140**(4A): p. A1133-A1138.
  60. Wellendorff, J., T.L. Silbaugh, D. Garcia-Pintos, J.K. Nørskov, T. Bligaard, F. Studt, and C.T. Campbell, *A benchmark database for adsorption bond energies to transition metal surfaces and comparison to selected DFT functionals. Surf. Sci.*, 2015. **640**: p. 36-44.
  61. Mallikarjun Sharada, S., T. Bligaard, A.C. Luntz, G.-J. Kroes, and J.K. Nørskov, *SBH10: A Benchmark Database of Barrier Heights on Transition Metal Surfaces. J. Phys. Chem. C*, 2017. **121**(36): p. 19807-19815.
  62. Medvedev, M.G., I.S. Bushmarinov, J. Sun, J.P. Perdew, and K.A. Lyssenko, *Density functional theory is straying from the path toward the exact functional. Science*, 2017. **355**(6320): p. 49-52.
  63. Schlegel, H.B., *Exploring potential energy surfaces for chemical reactions: An overview of some practical methods. J. Comput. Chem.*, 2003. **24**(12): p. 1514-1527.
  64. Nitoń, P., A. Żywociński, M. Fiałkowski, and R. Hołyst, *A "nano-windmill" driven by a flux of water vapour: a comparison to the rotating ATPase. Nanoscale*, 2013. **5**(20): p. 9732-9738.
  65. Campbell, C.T., *Future Directions and Industrial Perspectives Micro- and macro-kinetics: Their relationship in heterogeneous catalysis. Top. Catal.*, 1994. **1**(3): p. 353-366.
  66. Campbell, C.T., *Finding the Rate-Determining Step in a Mechanism: Comparing DeDonder Relations with the "Degree of Rate Control". J. Catal.*, 2001. **204**(2): p. 520-524.
  67. Stegelmann, C., A. Andreasen, and C.T. Campbell, *Degree of Rate Control: How Much the Energies of Intermediates and Transition States Control Rates. J. Am. Chem. Soc.*, 2009. **131**(23): p. 8077-8082.





## 2

# CO<sub>2</sub> hydrogenation to methanol over Cd<sub>4</sub>/TiO<sub>2</sub>



Supported metal catalysts have shown to be efficient for CO<sub>2</sub> conversion due to their multifunctionality and high stability. Herein, we have combined density functional theory calculations with microkinetic modeling to investigate the catalytic reaction mechanisms of CO<sub>2</sub> hydrogenation to CH<sub>3</sub>OH over a recently reported catalyst of Cd<sub>4</sub>/TiO<sub>2</sub>. Calculations reveal that the metal-oxide interface is the active center for CO<sub>2</sub> hydrogenation and methanol formation via the formate pathway dominates over the RWGS pathway. Microkinetic modeling demonstrated that formate species on the surface of Cd<sub>4</sub>/TiO<sub>2</sub> is the relevant intermediate for the production of CH<sub>3</sub>OH, and CH<sub>2</sub>O<sup>#</sup> formation is the rate-determining step. These findings demonstrate the crucial role of the Cd-TiO<sub>2</sub> interface in controlling CO<sub>2</sub> reduction reactivity and CH<sub>3</sub>OH selectivity.

## 2.1 Introduction

The increase of CO<sub>2</sub> concentration in the atmosphere is one of the major factors in global climate change. CO<sub>2</sub> capture and valorization have been considered as promising strategies to mitigate this problem [1, 2]. Using CO<sub>2</sub> as a feedstock to produce valuable chemicals not only can help to decrease dramatically the amount of CO<sub>2</sub> emitted into the atmosphere but also provide economic benefits [2, 3]. A large number of value-added chemicals can be produced from CO<sub>2</sub> via platform molecules such as CO, CH<sub>4</sub>, and CH<sub>3</sub>OH [4, 5]. Among these, CH<sub>3</sub>OH is highly desirable because it is an important fuel as well as a starting feedstock for the production of more valuable chemical compounds [6]. Recently, two different approaches for CO<sub>2</sub> hydrogenation to CH<sub>3</sub>OH have received a lot of attention: (1) electrochemical reduction and (2) thermochemical reduction [7]. The electrochemical CO<sub>2</sub> reduction offers the advantage that product distribution can be controlled by adjusting electrolyte, electrocatalyst, and applied voltage [8-11]. However, the selectivity, energetic efficiency, and electrode lifetime restrict its large-scale applications [10, 11]. Therefore, using the thermochemical approach to synthesize CH<sub>3</sub>OH from CO<sub>2</sub> hydrogenation is more practical for potential industrial applications compared to the alternative electrochemical CO<sub>2</sub> reduction. It offers an opportunity to develop sustainable technologies and environmentally benign chemical processes since H<sub>2</sub>, a reducing agent, can readily be obtained from renewable energy resources [1, 3].

Many studies have been devoted to creating new tailor-made CO<sub>2</sub> conversion catalysts with improved activity and selectivity to methanol, of which Cu/ZnO/Al<sub>2</sub>O<sub>3</sub> catalyst has been industrialized [12, 13]. However, the disadvantages of low CH<sub>3</sub>OH selectivity and the sintering of Cu and ZnO motivated the development of new Cu-based catalysts such as Cu/ZnO [14, 15], Cu/ZrO<sub>2</sub> [16, 17], and Cu/CeO<sub>2</sub> [18]. In these catalytic systems, it was found that H<sub>2</sub> molecule is dissociated at the Cu site and CO<sub>2</sub> is activated at the oxide surface, while the interface between Cu and metal oxide supports plays a crucial role for the stabilization of the reaction intermediate for CH<sub>3</sub>OH formation [16, 17]. Besides Cu-based catalysts, various other materials have also been reported as promising catalysts for CO<sub>2</sub> hydrogenation to CH<sub>3</sub>OH. For instance, Au [19-21], Pd [22-25], Re [26], ZnO [27], and In<sub>2</sub>O<sub>3</sub> [28, 29] supported on oxides were reported to be active toward the production of CH<sub>3</sub>OH under moderate conditions. Although many different types of catalysts have been reported, all of the active sites involved in the reaction have a common feature of multifunctionality in nature. Efficient cooperation between active sites of different

catalytic natures coupled in one heterogeneous catalyst plays a key role in eventual selective CH<sub>3</sub>OH formation.

Regarding the reaction mechanism, typically, two different reaction pathways have been proposed for the hydrogenation of CO<sub>2</sub> to CH<sub>3</sub>OH: (1) the reverse water-gas shift (RWGS) pathway and (2) the formate pathway. In the RWGS reaction, CO<sub>2</sub> is hydrogenated to form CO\* intermediate, which is then further hydrogenated to form CH<sub>3</sub>OH. For the formate pathway, CH<sub>3</sub>OH is produced via the formate (HCOO\*) intermediate [30, 31]. Most studies have suggested that the formate pathway is preferred over the RWGS pathway [13, 22, 32-35]. The main reason is that the binding strength of CO\* intermediate on these catalysts is quite weak, leading to the desorption of CO to the gas phase. However, on some other catalysts, such as Cu/TiO<sub>2</sub>, Cu/ZrO<sub>2</sub>, and Cu/CeO<sub>x</sub>, CH<sub>3</sub>OH was produced through CO\* intermediate due to the strong enough interaction between CO\* and catalyst [17, 18]. Therefore, the specific reaction pathway dominating methanol formation is system-dependent and should be investigated individually.

Recently, our experimental collaborators have discovered a promising reactivity of Cd/TiO<sub>2</sub> and CdTiO<sub>3</sub> catalysts in CO<sub>2</sub> hydrogenation to methanol [36]. It was found that Cd/TiO<sub>2</sub> catalyst exhibits a much higher catalytic CO<sub>2</sub> hydrogenation activity than the CdTiO<sub>3</sub> mixed oxide. To further identify the detailed reaction mechanism catalyzed by Cd/TiO<sub>2</sub> and clarify the functionalities of different types of active sites in this system, we constructed a Cd/TiO<sub>2</sub> model catalyst and investigated its catalytic activity towards CO<sub>2</sub> conversion to methanol with H<sub>2</sub> as a reductant. The key objective of this study is to explore the multiple-site cooperation effects on the catalyst reactivity by combining DFT calculation with microkinetic modeling.

## 2.2 Computational details

All DFT calculations have been performed using the Vienna Ab Initio Simulation Package (VASP) [37, 38]. The generalized gradient approximation (GGA) with Perdew-Burke-Ernzerhof (PBE) exchange and correlation functional was used to account for the exchange-correlation energy [38, 39]. The kinetic energy cutoff of the plane wave basis set was set to 400 eV. The threshold for energy convergence for each iteration was set to 10<sup>-5</sup> eV. Geometries were assumed to be converged when forces on each atom were less than 0.05 eV/Å. Gaussian smearing of the population of partial occupancies with a width of 0.10 eV was used during iterative diagonalization of the Kohn-Sham Hamiltonian.

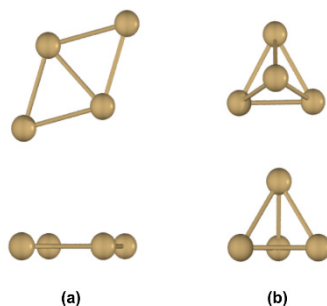
The bulk  $\text{TiO}_2$  unit cell in the phase of anatase was firstly fully optimized. The optimized lattice vectors of  $a = 3.799 \text{ \AA}$   $b = 3.799 \text{ \AA}$   $c = 9.716 \text{ \AA}$  have a good agreement with the experiment parameters [40]. For  $\text{Cd}_4/\text{TiO}_2$  model, 1x3 and 2x4 supercells of anatase  $\text{TiO}_2$  (101) surface with a vacuum space of 15  $\text{\AA}$  were built for investigation of the reaction mechanism of  $\text{H}_2$  dissociation and  $\text{CO}_2$  hydrogenation, respectively. These slab models contain six titanium layers with the bottom three layers fixed while the rest was allowed to relax during the geometry optimization. The lattice parameters were fixed throughout the surface calculations. The nudged-elastic band method with the improved tangent estimate (CI-NEB) was used to determine the minimum energy path and to locate the transition state structure for each elementary reaction step [41]. The maximum energy geometry along the reaction path generated by the NEB method was further optimized using a quasi-Newton algorithm. Vibrational frequencies were calculated by determining the second derivatives of the Hessian matrix using the density functional perturbation theory as implemented in VASP 5.3.5. Transition state was confirmed by showing a single imaginary frequency corresponding to each reaction coordinate. Bader charge analysis was visualized by VESTA software [42]. Mean-field microkinetic modeling (MKM) is applied based on the DFT calculations of all elementary reaction steps. All MKM results are simulated by a home-made script.

## 2.3 Results

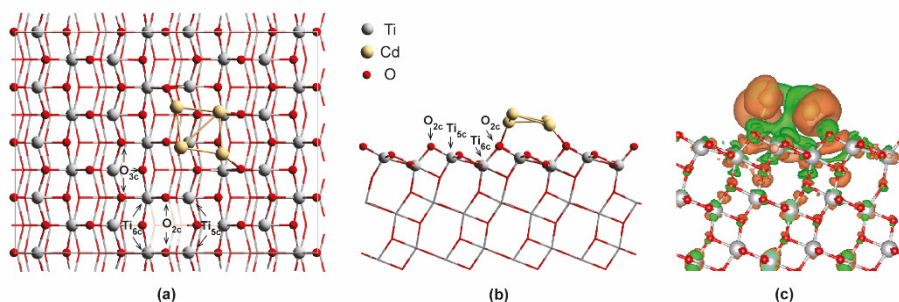
### 2.3.1 $\text{Cd}_4/\text{TiO}_2$ model rationalization

A cluster containing 4 Cd atoms ( $\text{Cd}_4$ ) was selected as representative of the supported Cd nanoparticles on the  $\text{TiO}_2$  surface since it was reported as the smallest Cd cluster featuring a magic number of Cd atoms [43]. In order to model the  $\text{Cd}_4/\text{TiO}_2$  catalyst, two possible configurations of isolated  $\text{Cd}_4$  cluster, i.e., a tetrahedron ( $T_d$ ) and planar rhombus ( $C_{2v}$ ) [44] were firstly optimized in the vacuum by using a large unit cell of 15x15x15  $\text{\AA}$ , as shown in Figure 2.1. Then the so-obtained  $\text{Cd}_4$  clusters were deposited and optimized on the (101) surface of anatase  $\text{TiO}_2$ . It is found that the most stable configuration of the supported  $\text{Cd}_4$  cluster on the (101)  $\text{TiO}_2$  surface is a deformed planar geometry even though the tetrahedron is more stable in the gas phase. As shown in Figure 2.2, the  $\text{Cd}_4$  ( $C_{2v}$ ) cluster is slightly distorted upon the adsorption with one of the Cd atoms lying above the plane of the other three. The adsorption energy of  $\text{Cd}_4$  over the surface is calculated to be -1.05 eV indicating a strong interaction between the metal cluster and the support of  $\text{TiO}_2$ . Bader charge analysis demonstrates that the entire

$\text{Cd}_4$  cluster is  $+1.48|e|$  charged, which indicates that the electrons are transferred from  $\text{Cd}_4$  cluster to  $\text{TiO}_2$  surface through metal-support interaction.



**Figure 2.1** The optimized  $\text{Cd}_4$  clusters: **(a)** planar rhombus and **(b)** tetrahedron. The clusters represent in top view (top) and side view (bottom).

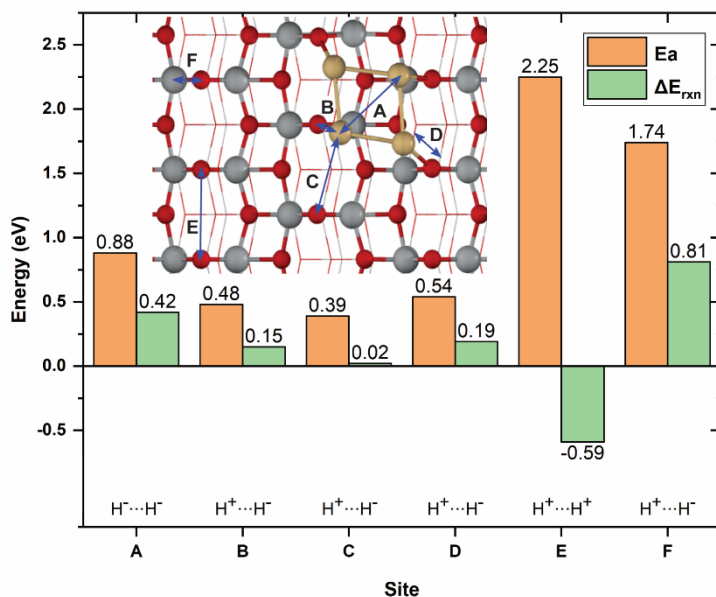


**Figure 2.2** **(a)** Top view and **(b)** side view of  $\text{Cd}_4/\text{TiO}_2(101)$  slab model. The  $\text{O}_{2c}$  and  $\text{O}_{3c}$  are twofold coordinated and threefold coordinated oxygen atoms, and the  $\text{Ti}_{5c}$  and  $\text{Ti}_{6c}$  are fivefold coordinated and sixfold coordinated titanium atoms on the surface of  $\text{TiO}_2$ , respectively. **(c)** The electron density difference plots upon the adsorption of  $\text{Cd}_4$  cluster on  $\text{TiO}_2$  surface. The orange and green regions represent electrons depletion and accumulation, respectively (isosurface value =  $0.05 \text{ e}/\text{Bohr}^3$ ).

### 2.3.2 $\text{H}_2$ dissociation and H spillover

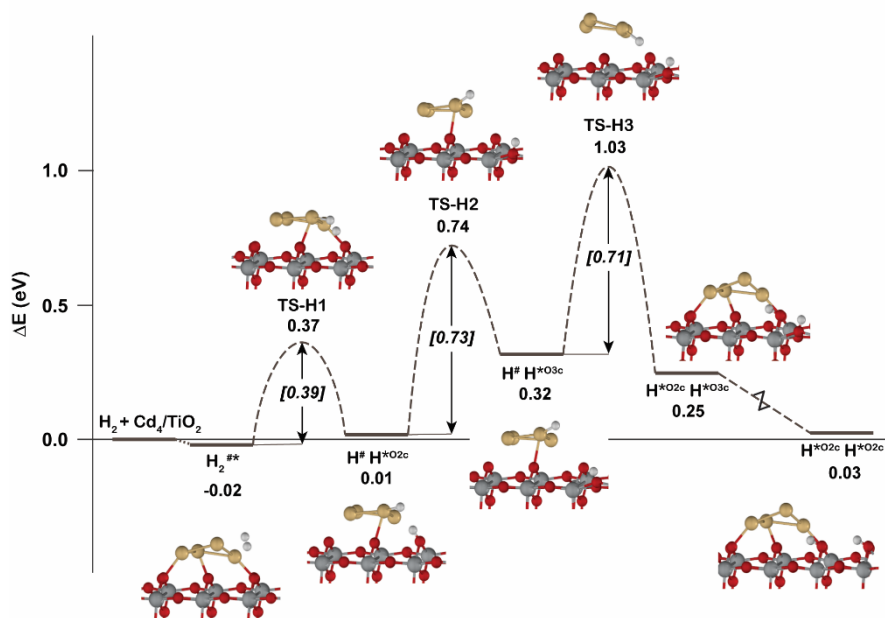
Many studies have proposed that activation and dissociation of an  $\text{H}_2$  molecule take place at the metal-oxide interface [45-47]. In this work, six possible active sites of  $\text{Cd}_4/\text{TiO}_2$  catalyst for the activation and dissociation of  $\text{H}_2$  molecule was systematically studied. As shown in Figure 2.3, site A is on top of the supported  $\text{Cd}_4$  cluster. Site B, C and D are at the interface of  $\text{Cd}_4/\text{TiO}_2$  ( $\text{Cd}\cdots\text{O}_{2c}$ ). Site E is located between two nearest  $\text{O}_{2c}$  atoms and site F is on top of bridging  $\text{Ti}_{5c}$  and  $\text{O}_{2c}$  atoms of  $\text{TiO}_2$  surface. From Figure 2.3, it can be seen that heterolytic  $\text{H}_2$  dissociation at the interface of  $\text{Cd}/\text{TiO}_2$  is more preferable than the other sites. Among all interface

sites considered, H<sub>2</sub> dissociation over site C has the lowest activation barrier (0.39 eV). Homolytic dissociation of H<sub>2</sub> molecule over site A needs to overcome an activation barrier of 0.88 eV and generates two hydrides on the supported Cd<sub>4</sub> cluster. On the TiO<sub>2</sub> surface, both homolytic (site E) and heterolytic dissociation pathways (site F) exhibit very high activation barriers (1.74 and 2.25 eV), indicating that TiO<sub>2</sub> surface site is inactive for H<sub>2</sub> activation. This is in agreement with a previous theoretical study of H<sub>2</sub> dissociation on TiO<sub>2</sub> surfaces [48].



**Figure 2.3.** Activation energy ( $E_a$ ) and reaction energy ( $\Delta E_{rxn}$ ) for H<sub>2</sub> dissociation at all possible active sites of Cd<sub>4</sub>/TiO<sub>2</sub> catalyst.

After we figured out the most favorable active site for H<sub>2</sub> dissociation, the spillover process of the so-formed H\* on the surface of the Cd<sub>4</sub>/TiO<sub>2</sub> is further studied. As shown in Figure 2.4, the migration of the H\* generated by H<sub>2</sub> dissociation at the interface (site C) from O<sub>2c</sub> site to its neighboring O<sub>3c</sub> site has an activation barrier of 0.73 eV. The other H\* species on the Cd<sub>4</sub> cluster can also spillover to the surface of TiO<sub>2</sub> with an activation barrier of 0.71 eV. H\* on O<sub>3c</sub> site can also hop to another O<sub>2c</sub> site next to it by overcoming a barrier of only 0.42 eV. The overall reaction is slightly endothermic. These results indicate that the activated H\* on the surface of the Cd<sub>4</sub>/TiO<sub>2</sub> catalyst is rather dynamic and hydrogen migrations among different surface sites is thermodynamically and kinetically easy processes.



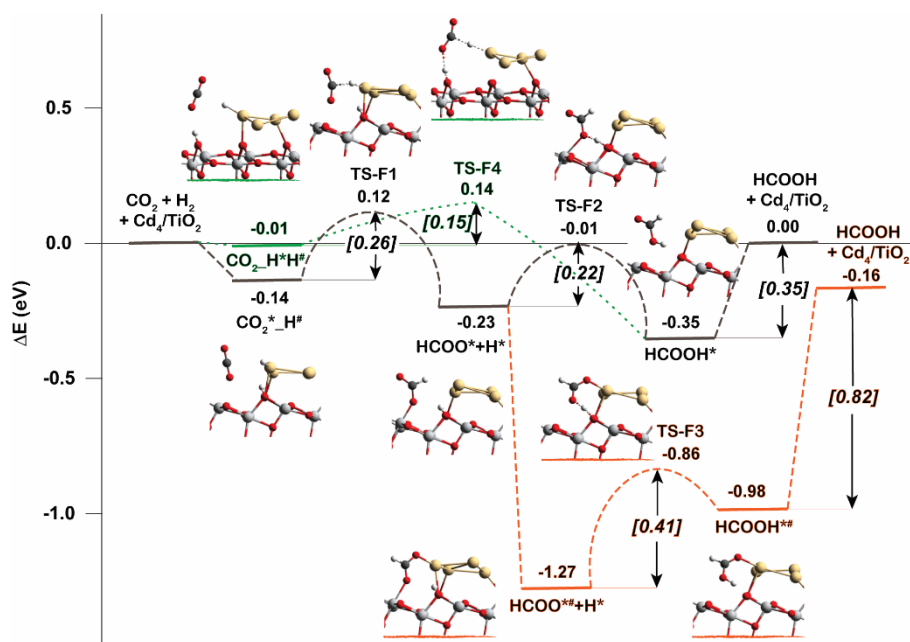
**Figure 2.4** The reaction energy profiles for the  $\text{H}_2$  dissociation followed by H migration and H spillover on  $\text{Cd}_4/\text{TiO}_2$  catalyst

### 2.3.3 $\text{CO}_2$ hydrogenation to $\text{HCOOH}$ and $\text{CO}$

In this section, the hydrogenation of  $\text{CO}_2$  on  $\text{Cd}_4/\text{TiO}_2$  catalyst will be discussed. Two main reaction pathways of  $\text{CO}_2$  hydrogenation which have been intensively debated in the literature were studied: (1) methanol formation via the intermediate of  $\text{HCOOH}^*$ , and (2) methanol formation via the reversed water-gas shift (RWGS) pathway with  $\text{CO}$  as an intermediate. Note that the species with asterisk (\*) and hash sign (#) are species that interact with  $\text{TiO}_2$  surface and  $\text{Cd}_4$  cluster of the  $\text{Cd}_4/\text{TiO}_2$  catalyst, respectively.

**Formate pathway:** The reaction mechanisms of  $\text{CO}_2$  hydrogenation to formate ( $\text{HCOO}^*$ ) and formic acid ( $\text{HCOOH}^*$ ) are shown in Figure 2.5. After heterolytic dissociation of  $\text{H}_2$  at the interface of  $\text{Cd}_4/\text{TiO}_2$ , a hydride coordinated to Cd ( $\text{H}^\#$ ) and a proton bonded to  $\text{O}_{2c}$  site ( $\text{H}^*$ ) are produced.  $\text{CO}_2$  is adsorbed over the  $\text{Ti}_{5c}$  site nearby both  $\text{H}^*$  and  $\text{H}^\#$  species. The adsorption energy is calculated to be  $-0.14$  eV. Then  $\text{CO}_2$  can be hydrogenated by the transfer of  $\text{H}^\#$  from  $\text{Cd}_4$  cluster to the C atom of  $\text{CO}_2$  forming formate intermediate of  $\text{HCOO}^*$ . The activation barrier for this step is only  $0.26$  eV. Further protonation of  $\text{HCOO}^*$  to form formic acid ( $\text{HCOOH}^*$ ) can be realized via two different reaction routes, either by protonation of monodentate  $\text{HCOO}^*$  intermediate to form *cis*- $\text{HCOOH}^*$  (gray line in Figure 2.5), or protonation

of bidentate  $\text{HCOO}^{*\#}$  intermediate which can be formed by structure rearrangement to form  $\text{trans-HCOOH}^{*\#}$  (orange line in figure 2.5). The activation barriers of proton transfer for both routes are relatively low (0.22 and 0.41 eV), however, the configurational transformation of  $\text{HCOO}^*$  from monodentate coordination to bidentate coordination with both  $\text{Ti}_{5c}$  and Cd before protonation reaction is dramatically favorable. Another possible pathway for  $\text{HCOOH}^*$  formation is also identified with a small activation barrier of 0.15 eV, the so-called concerted reaction mechanism with  $\text{CO}_2$  hydrogenation by both  $\text{H}^*$  and  $\text{H}^\#$  in one step (green line in Figure 2.5).

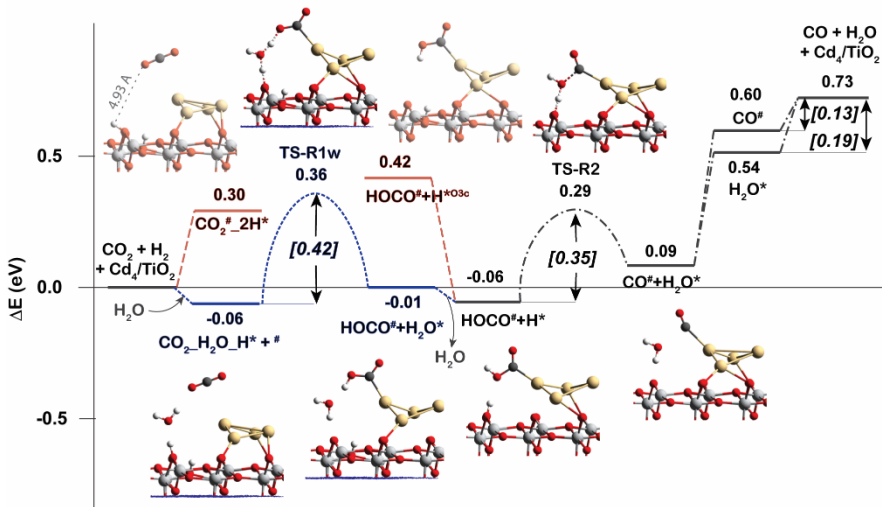


**Figure 2.5.** Reaction energy profiles for the  $\text{CO}_2$  hydrogenation to  $\text{HCOOH}^*$  on  $\text{Cd}_4/\text{TiO}_2$  catalyst. Green line is the concerted pathway. Gray line is the stepwise pathway via monodentate  $\text{HCOO}^*$ . Orange line is the stepwise pathway via bidentate  $\text{HCOO}^{*\#}$ . The species with asterisk (\*) and hash sign (#) are species that interact with  $\text{TiO}_2$  surface and  $\text{Cd}_4$  cluster of the  $\text{Cd}_4/\text{TiO}_2$  catalyst, respectively.

**RWGS pathway:** The RWGS reaction mechanism is initiated by  $\text{CO}_2$  hydrogenation to form a carboxylate intermediate ( $\text{HOCO}^\#$ ), from which CO is produced and can be further converted into methanol by continuous hydrogenation reactions. As shown in Figure 2.6, the reaction starts with the adsorption of  $\text{CO}_2$  at the perimeter site of  $\text{Cd}_4$  cluster after hydrogen spillover process. Then, the  $\text{CO}_2$  can be protonated by the  $\text{H}^*$  on  $\text{TiO}_2$  surface forming  $\text{HOCO}^\#$ . It is found that this reaction cannot occur directly due to the long distance



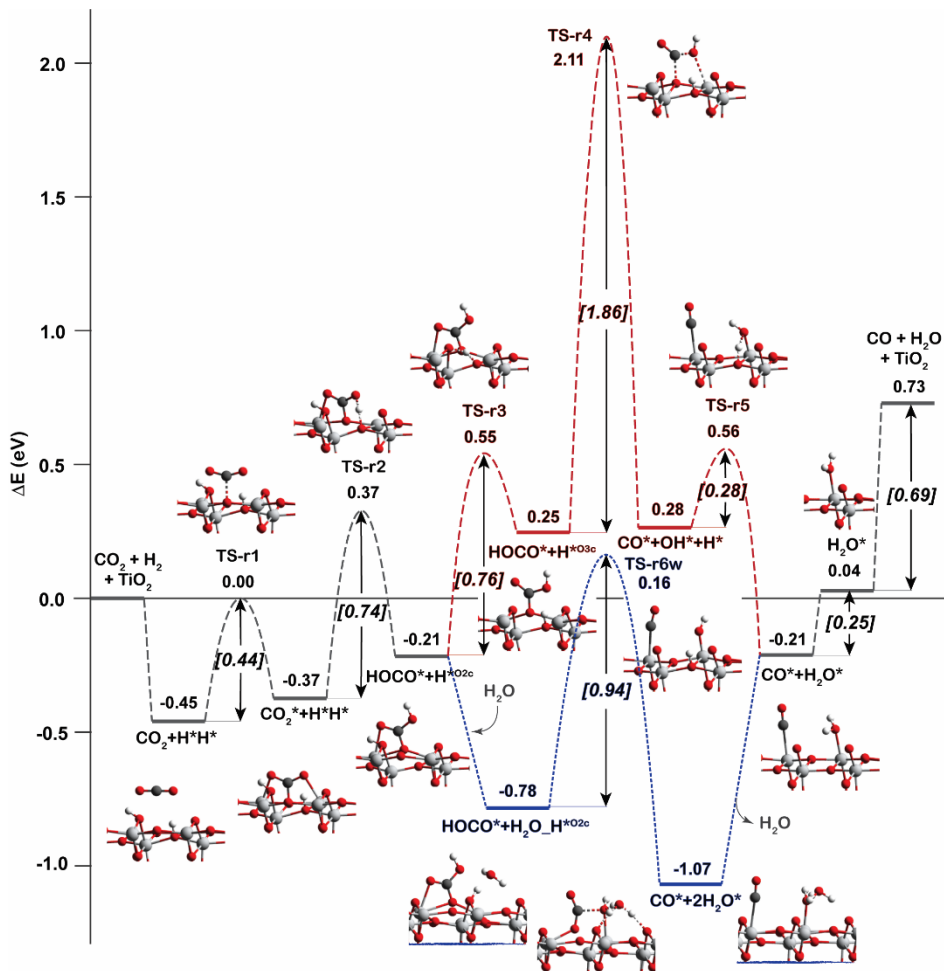
between  $\text{CO}_2$  and  $\text{H}^*$  (4.93 Å). However, it can proceed with the assistance of an  $\text{H}_2\text{O}$  molecule which acts as a proton shuttle between  $\text{H}^*$  and  $\text{CO}_2$  (blue line in Figure 2.6). The activation energy in this case is calculated to be 0.42 eV indicating that this process is feasible. Subsequent hydrogenation of the  $\text{HOCO}^\#$  intermediate at its terminal OH group with the breaking of C-O bond produces  $\text{CO}^\#$  and  $\text{H}_2\text{O}^*$ . This process requires overcoming an activation barrier of 0.35 eV. Finally,  $\text{CO}$  and  $\text{H}_2\text{O}$  can be desorbed from the catalyst with desorption barriers of 0.13 and 0.19 eV, respectively.



**Figure 2.6** Reaction energy profiles for the  $\text{CO}_2$  hydrogenation to  $\text{CO}$  on  $\text{Cd}_4/\text{TiO}_2$  catalyst (RWGS pathway). Blue line is the reaction with the assistance of  $\text{H}_2\text{O}$  molecule.

Due to the unfavorable adsorption of  $\text{CO}_2$  on the supported  $\text{Cd}_4$  cluster, we also explored the  $\text{CO}_2$  adsorption on a separate  $\text{TiO}_2$  surface site without interaction with the  $\text{Cd}_4$  cluster. The mechanisms of RWGS reaction on the  $\text{TiO}_2$  surface are shown in Figure 2.7. In this case, this reaction starts with the adsorption of  $\text{CO}_2$  on the  $\text{TiO}_2$  surface after hydrogen spillover process. The adsorption energy of  $\text{CO}_2$  is calculated to be -0.45 eV which is relatively stronger than that on supported  $\text{Cd}_4$  cluster. The bent  $\text{CO}_2$  geometry can be formed on the  $\text{TiO}_2$  surface with an activation barrier of 0.44 eV. Then the adsorbed  $\text{CO}_2^*$  is directly hydrogenated to form  $\text{HOCO}^*$  without the  $\text{H}_2\text{O}$  mediator. The activation energy for this step is calculated to be 0.74 eV. The diffusion of the second  $\text{H}^*$  to the  $\text{O}_{3c}$  site close to the OH group of  $\text{HOCO}^*$  needs to overcome an activation barrier of 0.76 eV. After that, the cleavage of the C-O bond of  $\text{HOCO}^*$  intermediate to generate  $\text{CO}^*$  and  $\text{OH}^*$  species on the  $\text{TiO}_2$  surface is rather difficult with an activation barrier of 1.86 eV.

However, the presence of H<sub>2</sub>O molecule can again decrease this activation barrier to 0.94 eV with C-O bonding breaking and OH group hydrogenation occurring simultaneously.



**Figure 2.7** Reaction energy profiles for the CO<sub>2</sub> hydrogenation to CO on clean TiO<sub>2</sub> surface (RWGS pathway). Blue line is the reaction with the assistance of H<sub>2</sub>O molecule.

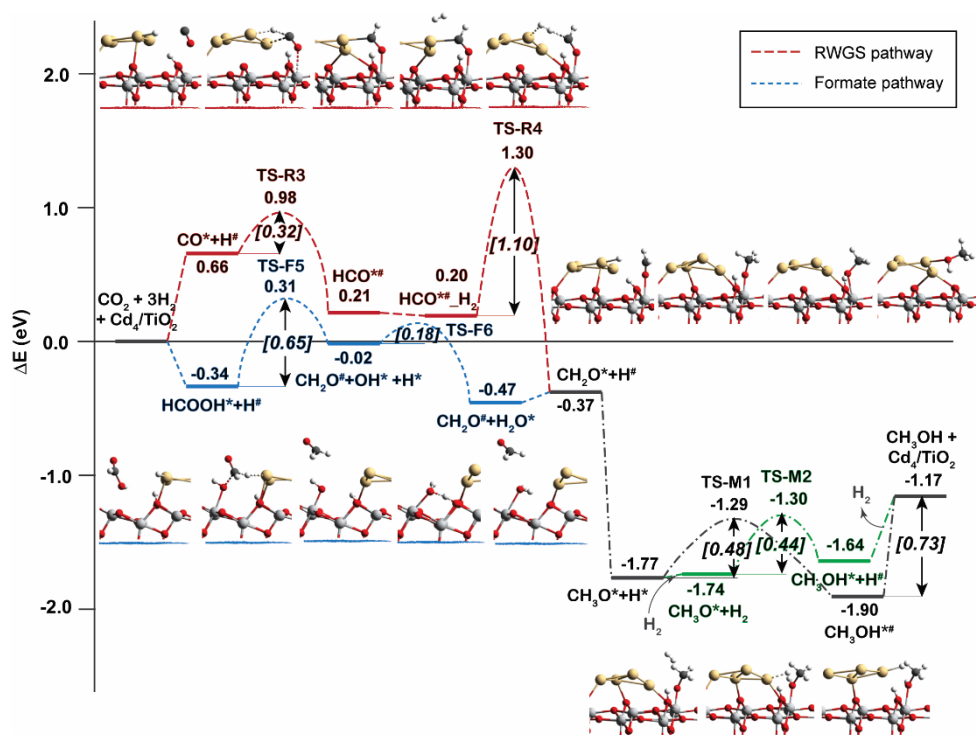
It is found that H<sub>2</sub>O molecule plays an important role as a proton shuttle to promote the most difficult reaction steps during the RWGS reactions taking place at both the interface and TiO<sub>2</sub> surface of Cd<sub>4</sub>/TiO<sub>2</sub> catalyst. The hydrogenation reaction of CO<sub>2</sub> is the most difficult step for the reaction that occurred at the interface, while the C-O bond cleavage of HOCO\* carboxylate intermediate is found to be the most difficult step for the reaction occurred at the TiO<sub>2</sub> surface. The

highest activation energy of the RWGS reaction that occurs at the interface of Cd<sub>4</sub> and TiO<sub>2</sub> surface (TS-R1w) is about two times lower than that of the other reaction route on the TiO<sub>2</sub> surface (TS-r6w). Therefore, it is concluded that the most preferable active site for the RWGS reaction is the interface of Cd<sub>4</sub>/TiO<sub>2</sub> catalyst. Therefore, in the next section, the discussion of CH<sub>3</sub>OH formation via CO\* will only focus on the reaction route at the interface.

### 2.3.4 CH<sub>3</sub>OH formation

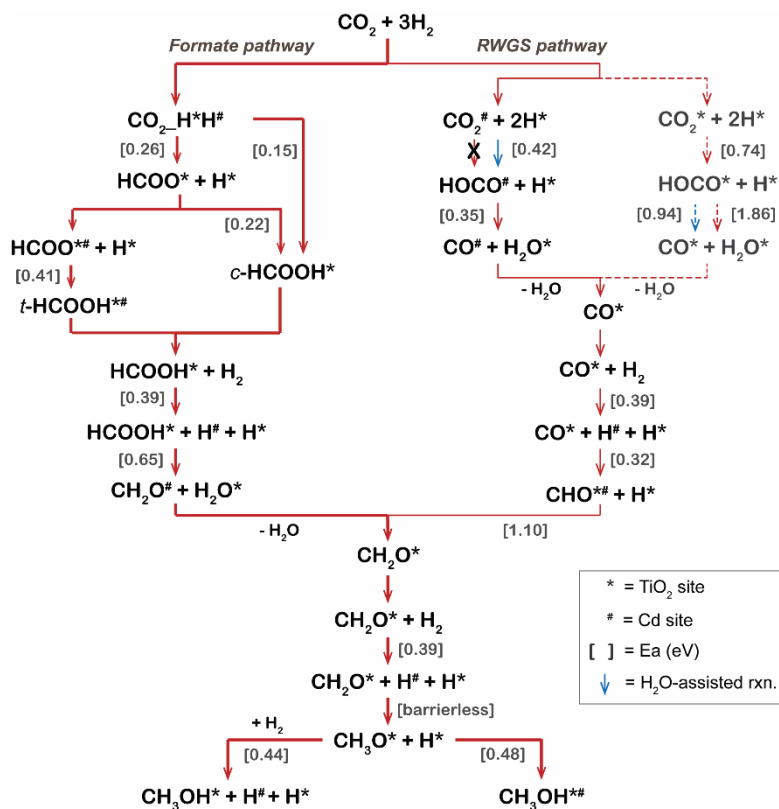
In this section, we will discuss the reaction mechanism of CH<sub>3</sub>OH formation from HCOOH\* as well as CO\* intermediates generated from the formate and the RWGS reaction pathways. The results are shown in Figure 2.8. Totally four elementary hydrogenation reaction steps are involved for CH<sub>3</sub>OH formation from CO i.e. CO\* → HCO\*<sup>#</sup>, HCO\*<sup>#</sup> → CH<sub>2</sub>O\*, CH<sub>2</sub>O\* → CH<sub>3</sub>O\* and CH<sub>3</sub>O\* → CH<sub>3</sub>OH. The activation barrier for CO hydrogenation to form HCO\*<sup>#</sup> is 0.32 eV by H<sup>#</sup> on Cd<sub>4</sub> cluster. The next step of dissociative adsorption of H<sub>2</sub> on top of HCO\*<sup>#</sup> intermediate generating CH<sub>2</sub>O\* and H<sup>#</sup> species has an activation barrier of 1.10 eV. Subsequent CH<sub>3</sub>O\* formation by CH<sub>2</sub>O\* hydrogenation is a barrierless process with a reaction energy of -1.40 eV. Finally, the CH<sub>3</sub>OH is formed by hydrogenation of CH<sub>3</sub>O\* intermediate with an activation barrier of 0.48 eV. In addition, CH<sub>3</sub>OH can be produced by the hydrogenolysis of CH<sub>3</sub>O\* (green line in Figure 2.8). The activation energy of this step is only 0.04 eV lower than that of the CH<sub>3</sub>O\* hydrogenation step. These results imply that both CH<sub>3</sub>O\* hydrogenolysis and CH<sub>3</sub>O\* hydrogenation coexist in the formation of CH<sub>3</sub>OH.

Alternatively, CH<sub>3</sub>OH can also be formed from HCOOH\* (blue line in Figure 2.8). The initial step is the hydrogenation of HCOOH\* to produce formaldehyde (CH<sub>2</sub>O<sup>#</sup>) and an OH\* species (CH<sub>2</sub>O<sup>#</sup>+OH\*+H\*). The activation energy of this step is calculated to be 0.65 eV. Then, the OH\* is protonated to form H<sub>2</sub>O and regenerate a vacant interfacial active site on the surface. In the next step, after another H<sub>2</sub> molecule is dissociated at the interface, the CH<sub>3</sub>OH can be formed by two successive hydrogenation steps from CH<sub>2</sub>O\*, which is the same process as the reactions via the RWGS pathway.

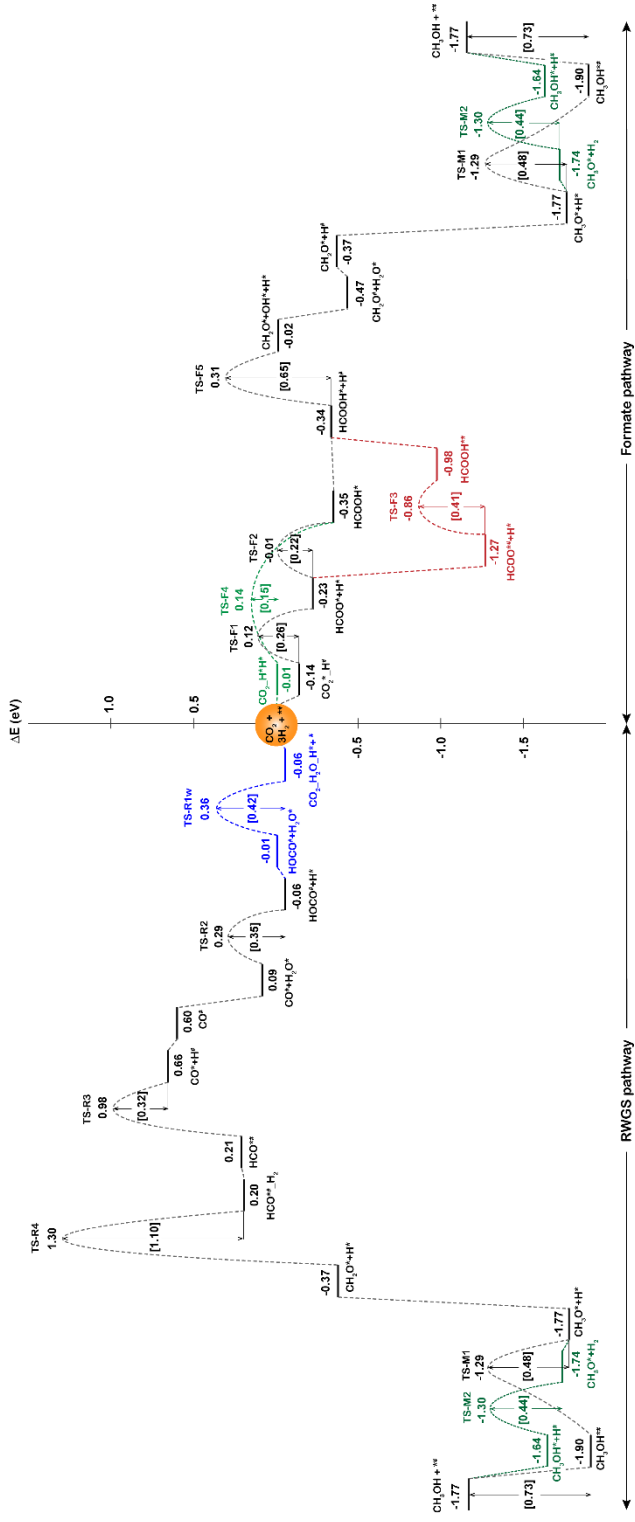


**Figure 2.8** Reaction energy profiles for the production of  $\text{CH}_3\text{OH}$  from  $\text{CO}$  and  $\text{HCOOH}$ .

To summarize, Figure 2.9 gives a schematic representation of the whole DFT reaction mechanism identified in this work, and the whole reaction pathways of  $\text{CO}_2$  hydrogenation to  $\text{CH}_3\text{OH}$  on  $\text{Cd}_4/\text{TiO}_2$  catalyst are shown in Figure 2.10. It can be seen that the formate pathway dominates over the RWGS pathway for the production of  $\text{CH}_3\text{OH}$  from  $\text{CO}_2$  and  $\text{H}_2$ . The formation of  $\text{CH}_2\text{O}^*$  intermediate is found to be the most difficult reaction step for  $\text{CH}_3\text{OH}$  production from both RWGS and formate reaction routes.



**Figure 2.9** A schematic representation of the whole reaction mechanism for  $\text{CO}_2$  hydrogenation to  $\text{CH}_3\text{OH}$  on  $\text{Cd}_4/\text{TiO}_2$  catalyst. Numbers in parentheses represent activation energies in eV. Solid lines and dash lines represent reactions at the interface and  $\text{TiO}_2$  surface, respectively.



**Figure 2.10** The complete reaction energy profiles for the competing mechanisms of the CO<sub>2</sub> hydrogenation to CH<sub>3</sub>OH on Cd<sub>4</sub>/TiO<sub>2</sub> catalyst

### 2.3.5 Microkinetic modeling

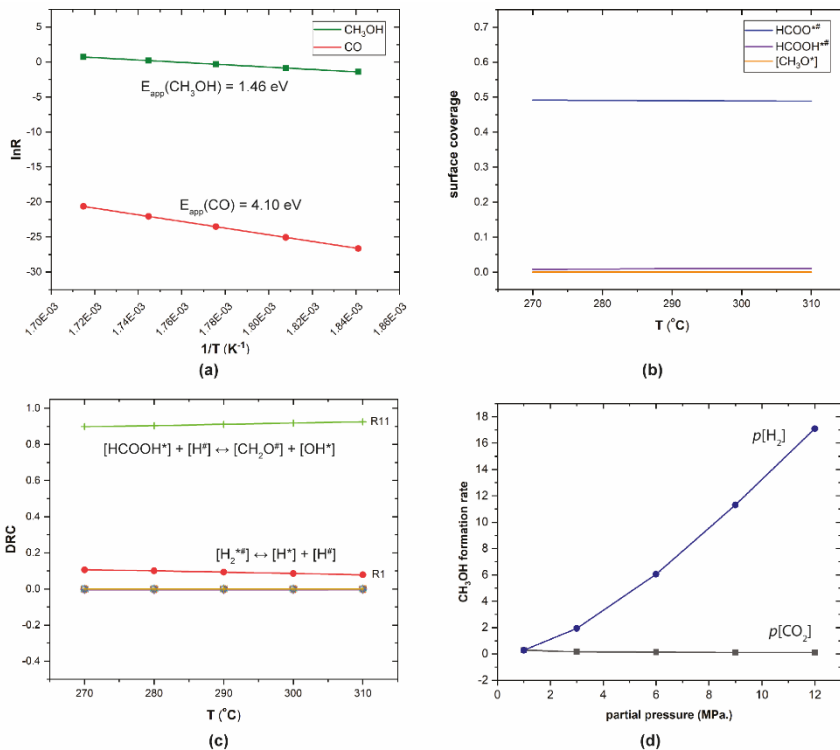
All considered elementary steps of the CO<sub>2</sub> hydrogenation to CH<sub>3</sub>OH on the interface sites of the Cd<sub>4</sub>/TiO<sub>2</sub> catalyst, and corresponding activation energies are listed in Table 2.1. The MKM is performed using a dual-site model representing TiO<sub>2</sub> (\*) and Cd (#) sites on Cd<sub>4</sub>/TiO<sub>2</sub> catalyst, respectively. The ratio between the number of \* and # sites is 0.5:0.5. The reaction rate, surface coverages, and degree of rate control (DRC) are calculated under the following steady-state reaction conditions: total pressure = 2MPa., H<sub>2</sub>/CO<sub>2</sub> = 3:1, temperature = 270-310°C. The apparent activation energy ( $E_{app}$ ) is determined from the slope of the Arrhenius plot, as shown in Figure 2.11a. The  $E_{app}$  for the CH<sub>3</sub>OH formation is calculated to be 1.46 eV, while that for the CO formation is computed at 4.10 eV, which is due to the incomplete representation of the catalyst system in the MKM model. Our calculations suggest that the direct RWGS can take place over TiO<sub>2</sub> surface with a barrier of around 2 eV, whereas the presence of H<sub>2</sub>O in the system can help establish the lower-energy path for the CO formation at the interface sites. However, in the simulations, the water coverage at such sites was very low, resulting in negligible CO formation and, as a result, the unrealistically high apparent activation barrier. The introduction of additional H<sub>2</sub>O in the system reduced the barrier for the RWGS path to the expected value of 0.77 eV that is close to the overall barrier for the CO desorption via the H<sub>2</sub>O-assisted reaction path. The presence of water did not affect the kinetic parameters for CH<sub>3</sub>OH production. The latter path dominated all MKM simulations in line with the experimental observations of the high selectivity to methanol over Cd/TiO<sub>2</sub> catalyst [36]. Therefore, we focused specifically on the methanol production path in further analysis of the MKM simulation results.

**Table 2.1** Summary of elementary reaction steps and activation energies from DFT calculations used for microkinetic modeling. Ea-f and Ea-b are activation energy for forward and backward reactions, respectively. \* and # represent TiO<sub>2</sub> and Cd sites on Cd<sub>4</sub>/TiO<sub>2</sub> catalyst.

	Elementary reaction step	Ea-f (eV)	Ea-b	
<b>H<sub>2</sub> dissociation</b>	R0: [H <sub>2</sub> ] + [*] + [#] ↔ [H <sub>2</sub> *#]	0.00	0.02	
	R1: [H <sub>2</sub> *#] ↔ [H*] + [H#]	0.39	0.38	
	R2: [H#] + [*] ↔ [H*] + [#]	0.71	0.78	
<b>Formate pathway</b>	R3: [CO <sub>2</sub> ] + [H*] + [H#] ↔ [CO <sub>2</sub> _H*H#]	0.00	0.01	
	R4: [CO <sub>2</sub> _H*H#] ↔ [HCOOH*] + [#]	0.15	0.49	
	R5: [CO <sub>2</sub> ] + [*] + [H#] ↔ [CO <sub>2</sub> *_H#]	0.00	0.14	
	R6: [CO <sub>2</sub> *_H#] ↔ [HCOO*] + [#]	0.26	0.35	
	R7: [HCOO*] + [H*] ↔ [HCOOH*] + [*]	0.22	0.34	
	R8: [HCOO*] + [#] ↔ [HCOO*#]	0.00	1.04	
	R9: [HCOO*#] + [H*] ↔ [HCOOH*#] + [*]	0.41	0.12	
	R10: [HCOOH*#] ↔ [HCOOH*] + [#]	0.63	0.00	
	R11: [HCOOH*] + [H#] ↔ [CH <sub>2</sub> O#] + [OH*]	0.65	0.33	
	R12: [CH <sub>2</sub> O#] + [*] ↔ [CH <sub>2</sub> O*] + [#]	0.00	0.44	
	R13: [OH*] + [H*] ↔ [H <sub>2</sub> O*] + [*]	0.18	0.63	
	R14: [H <sub>2</sub> O] + [*] ↔ [H <sub>2</sub> O*]	0.00	0.57	
	<b>CH<sub>3</sub>OH formation</b>	R15: [CH <sub>2</sub> O*] + [H#] ↔ [CH <sub>3</sub> O*] + [#]	0.00	1.40
		R16: [CH <sub>3</sub> O*] + [H*] + [#] ↔ [CH <sub>3</sub> OH*#] + [*]	0.48	0.61
R17: [CH <sub>3</sub> OH] + [*] + [#] ↔ [CH <sub>3</sub> OH*#]		0.00	0.73	
<b>RWGS pathway</b>	R18: [H <sub>2</sub> O] + [H*] ↔ [H <sub>2</sub> O_H*]	0.00	0.26	
	R19: [CO <sub>2</sub> ] + [H <sub>2</sub> O*] + [H <sub>2</sub> O_H*] ↔	0.00	0.06	
	R20: [CO <sub>2</sub> _H <sub>2</sub> O_H*] + [#] ↔ [HOCO#] +	0.42	0.37	
	R21: [H <sub>2</sub> O] + [*] ↔ [HOH*]	0.00	0.19	
	R22: [HOCO#] + [H*] ↔ [CO#] + [HOH*]	0.35	0.20	
	R23: [CO] + [#] ↔ [CO#]	0.00	0.13	
	R24: [CO] + [*] ↔ [CO*]	0.00	0.03	
	R25: [CO*] + [H#] ↔ [HCO*#]	0.32	0.77	
	R26: [HCO*#] + [H <sub>2</sub> ] ↔ [HCO*#_H <sub>2</sub> ]	0.00	0.01	
	R27: [HCO*#_H <sub>2</sub> ] ↔ [CH <sub>2</sub> O*] + [H#]	1.10	1.67	
	<b>CH<sub>3</sub>O* to CH<sub>3</sub>OH*</b>	R28: [CH <sub>3</sub> O*] + [H <sub>2</sub> ] + [#] ↔ [CH <sub>3</sub> OH*] + [H#]	0.44	0.34
R29: [CH <sub>3</sub> OH] + [*] ↔ [CH <sub>3</sub> OH*]		0.00	0.46	



Figure 2.11b shows that the  $\text{HCOO}^{*\#}$  has the highest surface coverage ( $\sigma \approx 0.5$ ), indicating the formation of this intermediate is the resting state of the overall reaction. This result is consistent with the experimental in-situ IR observation [36]. DRC analysis (Figure 2.11c) shows that the conversion of  $\text{HCOOH}^*$  to  $\text{CH}_2\text{O}^\#$  (R11), the most difficult reaction step of the formate pathway, is also the rate-determining step. This result demonstrates that formate pathway dominates over RWGS pathway for the  $\text{CO}_2$  hydrogenation to  $\text{CH}_3\text{OH}$  on the surface of  $\text{Cd}/\text{TiO}_2$  catalyst. In addition, it was found that the  $\text{H}_2$  dissociation reaction step (R1 in Table 1) has only a minor influence on the overall reaction rate. The effect of  $\text{H}_2$  and  $\text{CO}_2$  partial pressure on the reaction rate is also investigated by MKM, as shown in Figure 2.11d. These results indicate that increasing  $\text{H}_2$  partial pressure can significantly enhance the methanol production rate, which, in turn, is not affected by the  $\text{CO}_2$  partial pressure.



**Figure 2.11** Results of the microkinetic modeling for the  $\text{CO}_2$  hydrogenation on  $\text{Cd}/\text{TiO}_2$  catalyst. (a) is product formation rates as a function of temperature ( $T=270\text{--}310^\circ\text{C}$ ) and the calculated apparent activation energy ( $E_a$ ). (b) is surface coverages of major surface intermediates at  $270\text{--}310^\circ\text{C}$ . (c) is degree of rate control analysis at  $270\text{--}310^\circ\text{C}$ . (d) is the partial pressure dependence of the  $\text{CH}_3\text{OH}$  formation rate at  $290^\circ\text{C}$ . The partial pressure of another reactant is fixed as 1MPa.

## 2.4 Conclusion

In summary, the reaction mechanisms of CO<sub>2</sub> hydrogenation to methanol over TiO<sub>2</sub>-supported Cd catalyst have been investigated computationally by a combination of DFT and MKM modelling approaches. It is proposed that the interface between the Cd<sub>4</sub> cluster and the support of TiO<sub>2</sub> plays a key role for H<sub>2</sub> dissociation as well as preactivation of CO<sub>2</sub>. H<sub>2</sub> dissociation and CO<sub>2</sub> activation are energetically more favorable at the Cd-TiO<sub>2</sub> interface than that at bare TiO<sub>2</sub> surface and Cd cluster. Both CO<sub>2</sub> hydrogenation reactions to formate and CO are remarkably facilitated by the synergy between H<sup>-</sup> on Cd and H<sup>+</sup> on TiO<sub>2</sub> surface (Figure 2.5, formate pathway; Figure 2.6, RWGS pathway). In contrast, CO<sub>2</sub> conversion to CH<sub>3</sub>OH on bare TiO<sub>2</sub> is very difficult compared to the Cd/TiO<sub>2</sub> interface. Cd-TiO<sub>2</sub> interface is crucial for stabilizing various reaction intermediates and promoting the rate-determining step of formaldehyde formation identified by DFT and MKM. All these mechanism results indicate that the multifunctionality of Cd/TiO<sub>2</sub> interface, including Lewis acids of metals and Lewis base of surface oxygen, is of great importance accounting for the outstanding catalytic activity of Cd/TiO<sub>2</sub> material. Water molecules produced from the reaction or present in the reaction system can dramatically facilitate the most difficult reaction steps of RWGS reaction. However, formate is identified to be the relevant intermediate for CO<sub>2</sub> hydrogenation to methanol, with formaldehyde formation being the rate-limiting reaction step. Our results demonstrate that Cd/TiO<sub>2</sub> can be a promising candidate for valorization of CO<sub>2</sub> to produce methanol and the multifunctionality of the metal-support interface is a crucial aspect for rational design of CO<sub>2</sub> hydrogenation catalyst.

## References

1. Wang, W., S. Wang, X. Ma, and J. Gong, *Recent advances in catalytic hydrogenation of carbon dioxide*. *Chem Soc Rev*, 2011. **40**(7): p. 3703-27.
2. Alvarez, A., A. Bansode, A. Urakawa, A.V. Bavykina, T.A. Wezendonk, M. Makkee, J. Gascon, and F. Kapteijn, *Challenges in the Greener Production of Formates/Formic Acid, Methanol, and DME by Heterogeneously Catalyzed CO<sub>2</sub> Hydrogenation Processes*. *Chem Rev*, 2017. **117**(14): p. 9804-9838.
3. Pérez-Fortes, M., J.C. Schöneberger, A. Boulamanti, and E. Tzimas, *Methanol synthesis using captured CO<sub>2</sub> as raw material: Techno-economic and environmental assessment*. *Appl. Energy*, 2016. **161**: p. 718-732.

4. Li, W., H. Wang, X. Jiang, J. Zhu, Z. Liu, X. Guo, and C. Song, *A short review of recent advances in CO<sub>2</sub> hydrogenation to hydrocarbons over heterogeneous catalysts*. *RSC Adv.*, 2018. **8**: p. 7651-7669.
5. Ye, R.-P., W.G. Jie Ding, M.D. Argyle, Q. Zhong, Y. Wang, C.K. Russell, Z. Xu, A.G. Russell, Q. Li, M. Fan, and Y.-G. Yao, *CO<sub>2</sub> hydrogenation to high-value products via heterogeneous catalysis*. *Nat. Commun*, 2019. **10**: p. 5698.
6. Ghasemzadeh, K., S.M. Sadati Tilebon, M. Nasirinezhad, and A. Basile, *Economic Assessment of Methanol Production*, in *Methanol*. 2018. p. 613-632.
7. Albo, J., M. Alvarez-Guerra, P. Castaño, and A. Irabien, *Towards the electrochemical conversion of carbon dioxide into methanol*. *Green Chem.*, 2015. **17**(4): p. 2304-2324.
8. Yang, W., K. Dastafkan, C. Jia, and C. Zhao, *Design of Electrocatalysts and Electrochemical Cells for Carbon Dioxide Reduction Reactions*. *Adv. Mater. Technol.*, 2018. **3**(9): p. 1700377.
9. Qiao, J., Y. Liu, F. Hong, and J. Zhang, *A review of catalysts for the electroreduction of carbon dioxide to produce low-carbon fuels*. *Chem. Soc. Rev.*, 2014. **43**(2): p. 631-75.
10. Khezri, B., A.C. Fisher, and M. Pumera, *CO<sub>2</sub> reduction: the quest for electrocatalytic materials*. *J. Mater. Chem. A*, 2017. **5**(18): p. 8230-8246.
11. Sun, Z., T. Ma, H. Tao, Q. Fan, and B. Han, *Fundamentals and Challenges of Electrochemical CO<sub>2</sub> Reduction Using Two-Dimensional Materials*. *Chem*, 2017. **3**(4): p. 560-587.
12. Behrens, M., F. Studt, I. Kasatkin, S. Kühl, M. Hävecker, F. Abild-Pedersen, S. Zander, F. Girgsdies, P. Kurr, B.-L. Kniep, M. Tovar, R.W. Fischer, J.K. Nørskov, and R. Schlögl, *The Active Site of Methanol Synthesis over Cu-ZnO-Al<sub>2</sub>O<sub>3</sub> Industrial Catalysts*. *Science*, 2012. **336**: p. 893-897.
13. Kattel, S., P.J. Ramírez, J.G. Chen, J.A. Rodriguez, and P. Liu, *Active sites for CO<sub>2</sub> hydrogenation to methanol on Cu/ZnO catalysts*. *Science*, 2017. **355**(6331): p. 1296-1299.
14. Wu, J., M. Saito, M. Takeuchi, and T. Watanabe, *The stability of Cu/ZnO-based catalysts in methanol synthesis from a CO<sub>2</sub>-rich feed and from a CO-rich feed*. *Appl. Catal. A*, 2001. **218**: p. 235-240.
15. Hu, X., W. Qin, Q. Guan, and W. Li, *The Synergistic Effect of CuZnCeO<sub>x</sub> in Controlling the Formation of Methanol and CO from CO<sub>2</sub> Hydrogenation*. *ChemCatChem*, 2018. **10**(19): p. 4438-4449.
16. Larmier, K., W.C. Liao, S. Tada, E. Lam, R. Verel, A. Bansode, A. Urakawa, A. Comas-Vives, and C. Coperet, *CO<sub>2</sub>-to-Methanol Hydrogenation on Zirconia-Supported Copper Nanoparticles: Reaction Intermediates and the Role of the Metal-Support Interface*. *Angew. Chem. Int. Ed.*, 2017. **56**(9): p. 2318-2323.

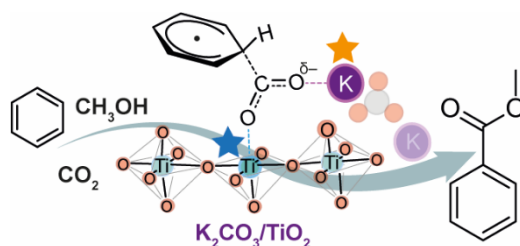
17. Kattel, S., B. Yan, Y. Yang, J.G. Chen, and P. Liu, *Optimizing Binding Energies of Key Intermediates for CO<sub>2</sub> Hydrogenation to Methanol over Oxide-Supported Copper*. *J. Am. Chem. Soc.*, 2016. **138**(38): p. 12440-50.
18. Graciani, J., K. Mudiyansele, F. Xu, A.E. Baber, J. Evans, S.D. Senanayake, D.J. Stacchiola, P.L. Hrbek, J.F. Sanz, and J.A. Rodriguez, *Highly active copper-ceria and copper-ceria-titania catalysts for methanol synthesis from CO<sub>2</sub>*. *Science*, 2014. **345**: p. 546-550.
19. Vourros, A., I. Garagounis, V. Kyriakou, S.A.C. Carabineiro, F.J. Maldonado-Hódar, G.E. Marnellos, and M. Konsolakis, *Carbon dioxide hydrogenation over supported Au nanoparticles: Effect of the support*. *J. CO<sub>2</sub> Util.*, 2017. **19**: p. 247-256.
20. Hartadi, Y., D. Widmann, and R.J. Behm, *Methanol formation by CO<sub>2</sub> hydrogenation on Au/ZnO catalysts – Effect of total pressure and influence of CO on the reaction characteristics*. *J. Catal.*, 2016. **333**: p. 238-250.
21. Rodriguez, J.A., J. Evans, L. Feria, A.B. Vidal, P. Liu, K. Nakamura, and F. Illas, *CO<sub>2</sub> hydrogenation on Au/TiC, Cu/TiC, and Ni/TiC catalysts: Production of CO, methanol, and methane*. *J. Catal.*, 2013. **307**: p. 162-169.
22. Malik, A.S., S.F. Zaman, A.A. Al-Zahrani, M.A. Daous, H. Driss, and L.A. Petrov, *Development of highly selective PdZn/CeO<sub>2</sub> and Ca-doped PdZn/CeO<sub>2</sub> catalysts for methanol synthesis from CO<sub>2</sub> hydrogenation*. *Appl. Catal. A: Gen.*, 2018. **560**: p. 42-53.
23. Snider, J.L., V. Streibel, M.A. Hubert, T.S. Choksi, E. Valle, D.C. Upham, J. Schumann, M.S. Duary, A. Gallo, F. Abild-Pedersen, and T.F. Jaramillo, *Revealing the Synergy between Oxide and Alloy Phases on the Performance of Bimetallic In–Pd Catalysts for CO<sub>2</sub> Hydrogenation to Methanol*. *ACS Catal.*, 2019. **9**(4): p. 3399-3412.
24. Wu, D., K. Deng, B. Hu, Q. Lu, G. Liu, and X. Hong, *Plasmon-Assisted Photothermal Catalysis of Low-Pressure CO<sub>2</sub> Hydrogenation to Methanol over Pd/ZnO Catalyst*. *ChemCatChem*, 2019. **11**(6): p. 1598-1601.
25. Jiang, F., S. Wang, B. Liu, J. Liu, L. Wang, Y. Xiao, Y. Xu, and X. Liu, *Insights into the Influence of CeO<sub>2</sub> Crystal Facet on CO<sub>2</sub> Hydrogenation to Methanol over Pd/CeO<sub>2</sub> Catalysts*. *ACS Catal.*, 2020. **10**(19): p. 11493-11509.
26. Ting, K.W., T. Toyao, S.M.A.H. Siddiki, and K.-i. Shimizu, *Low-Temperature Hydrogenation of CO<sub>2</sub> to Methanol over Heterogeneous TiO<sub>2</sub>-Supported Re Catalysts*. *ACS Catal.*, 2019. **9**(4): p. 3685-3693.
27. Wang, J., G. Li, Z. Li, C. Tang, Z. Feng, H. An, H. Liu, T. Liu, and C. Li, *A highly selective and stable ZnO-ZrO<sub>2</sub> solid solution catalyst for CO<sub>2</sub> hydrogenation to methanol*. *Sci. Adv.*, 2017. **3**(10): p. e1701290.
28. Yang, C., C. Pei, R. Luo, S. Liu, Y. Wang, Z. Wang, Z.-J. Zhao, and J. Gong, *Strong Electronic Oxide–Support Interaction over In<sub>2</sub>O<sub>3</sub>/ZrO<sub>2</sub> for Highly*

- Selective CO<sub>2</sub> Hydrogenation to Methanol*. *J. Am. Chem. Soc.*, 2020. **142**(46): p. 19523-19531.
29. Dang, S., B. Qin, Y. Yang, H. Wang, J. Cai, Y. Han, S. Li, P. Gao, and Y. Sun, *Rationally designed indium oxide catalysts for CO<sub>2</sub> hydrogenation to methanol with high activity and selectivity*. *Sci. Adv.*, 2020. **6**(25): p. eaaz2060.
  30. Li, Y., S.H. Chan, and Q. Sun, *Heterogeneous catalytic conversion of CO<sub>2</sub>: a comprehensive theoretical review*. *Nanoscale*, 2015. **7**(19): p. 8663-8683.
  31. Kattel, S., P. Liu, and J.G. Chen, *Tuning Selectivity of CO<sub>2</sub> Hydrogenation Reactions at the Metal/Oxide Interface*. *J. Am. Chem. Soc.*, 2017. **139**(29): p. 9739-9754.
  32. Dou, M., M. Zhang, Y. Chen, and Y. Yu, *Theoretical study of methanol synthesis from CO<sub>2</sub> and CO hydrogenation on the surface of ZrO<sub>2</sub> supported In<sub>2</sub>O<sub>3</sub> catalyst*. *Surf. Sci.*, 2018. **672-673**: p. 7-12.
  33. Wang, J., G. Li, Z. Li, C. Tang, Z. Feng, H. An, H. Liu, T. Liu, and C. Li, *A highly selective and stable ZnO-ZrO<sub>2</sub> solid solution catalyst for CO<sub>2</sub> hydrogenation to methanol*. *Sci Adv*, 2018. **3**(10): p. e1701290.
  34. Ye, J., C. Liu, D. Mei, and Q. Ge, *Active Oxygen Vacancy Site for Methanol Synthesis from CO<sub>2</sub> Hydrogenation on In<sub>2</sub>O<sub>3</sub>(110): A DFT Study*. *ACS Catal.*, 2013. **3**(6): p. 1296-1306.
  35. Liu, C., B. Yang, E. Tyo, S. Seifert, J. DeBartolo, B. von Issendorff, P. Zapol, S. Vajda, and L.A. Curtiss, *Carbon Dioxide Conversion to Methanol over Size-Selected Cu<sub>4</sub> Clusters at Low Pressures*. *J. Am. Chem. Soc.*, 2015. **137**(27): p. 8676-9.
  36. Wang, J., J. Meeprasert, Z. Han, H. Wang, Z. Feng, C. Tang, F. Sha, S. Tang, G. Li, and C.L. E.A. Pidko, *Highly dispersed Cd cluster supported on TiO<sub>2</sub> as an efficient catalyst for CO<sub>2</sub> hydrogenation to methanol*. *Chin. J. Catal.*, 2022. **43**(3): p. 761-770.
  37. Kresse, G. and J. Furthmüller, *Efficiency of ab-initio total energy calculations for metals and semiconductors using a plane-wave basis set*. *Comput. Mater. Sci.*, 1996. **6**(1): p. 15-50.
  38. Kresse, G. and J. Furthmüller, *Efficient iterative schemes for ab initio total-energy calculations using a plane-wave basis set*. *Phys. Rev. B*, 1996. **54**(16): p. 11169-11186.
  39. Perdew, J.P., K. Burke, and M. Ernzerhof, *Generalized Gradient Approximation Made Simple*. *Phys. Rev. Lett.*, 1996. **77**(18): p. 3865-3868.
  40. Diebold, U., *The surface science of titanium dioxide*. *Surf. Sci. Rep.*, 2003. **48**(5): p. 53-229.
  41. Henkelman, G., B.P. Uberuaga, and H. Jónsson, *A climbing image nudged elastic band method for finding saddle points and minimum energy paths*. *J. Chem. Phys.*, 2000. **113**(22): p. 9901-9904.

42. Momma, K. and F. Izumi, *VESTA 3 for three-dimensional visualization of crystal, volumetric and morphology data*. *J. Appl. Crystallogr.*, 2011. **44**(6): p. 1272-1276.
43. Kohaut, S. and M. Springborg, *Growth patterns and structural motifs of cadmium clusters with up to 60 atoms: disordered or not?* *Phys Chem Chem Phys*, 2016. **18**(41): p. 28524-28537.
44. Zhao, J., *Density-functional study of structures and electronic properties of Cd clusters*. *Phys. Rev. A*, 2001. **64**(4): p. 043204.
45. Boronat, M., F. Illas, and A. Corma, *Active Sites for H<sub>2</sub> Adsorption and Activation in Au-TiO<sub>2</sub> and the Role of the Support*. *J. Phys. Chem. A*, 2009. **113**: p. 3750-3757.
46. Wan, W., X. Nie, M.J. Janik, C. Song, and X. Guo, *Adsorption, Dissociation, and Spillover of Hydrogen over Au/TiO<sub>2</sub> Catalysts: The Effects of Cluster Size and Metal-Support Interaction from DFT*. *J. Phys. Chem. C*, 2018. **122**(31): p. 17895-17916.
47. Sun, K., M. Kohyama, S. Tanaka, and S. Takeda, *A Study on the Mechanism for H<sub>2</sub> Dissociation on Au/TiO<sub>2</sub> Catalysts*. *J. Phys. Chem. C*, 2014. **118**(3): p. 1611-1617.
48. Hu, G., Z. Wu, and D.-e. Jiang, *First Principles Insight into H<sub>2</sub> Activation and Hydride Species on TiO<sub>2</sub> Surfaces*. *J. Phys. Chem. C*, 2018. **122**(35): p. 20323-20328.

## 3

# Mechanistic investigation of benzene esterification with CO<sub>2</sub> and CH<sub>3</sub>OH by K<sub>2</sub>CO<sub>3</sub>/TiO<sub>2</sub>



Potassium carbonate dispersed over defective TiO<sub>2</sub> support (K<sub>2</sub>CO<sub>3</sub>/TiO<sub>2</sub>) is an efficient catalyst for benzene esterification with CO<sub>2</sub> and CH<sub>3</sub>OH. Density functional theory calculations reveal that this unique catalytic reactivity originates from the cooperation of the Ti<sup>3+</sup>/K<sup>+</sup> surface sites. K<sub>2</sub>CO<sub>3</sub> promoter steers the stabilization of surface intermediates thus preventing catalyst deactivation.

*This chapter has been published in ChemComm, 2021, 57, 7890-7893.*

### 3.1 Introduction

CO<sub>2</sub> conversion into valuable chemicals has received much attention due to the environmental concerns associated with the growing atmospheric concentrations of greenhouse gases. Many efforts have been invested to develop a carbon-neutral economic system by recycling the carbon resource of CO<sub>2</sub> from industrial emissions to the production of chemicals [1-3]. The carboxylation of aromatics by CO<sub>2</sub> is one of the attractive routes for the valorization of CO<sub>2</sub>, because the produced aromatic carboxylic acids and their derivatives can serve as important chemical feedstocks [4, 5]. Conventionally, such a carboxylation coupling reaction is carried out in the presence of strong base or Lewis acids such as NaH [6], AlCl<sub>3</sub> [4], and AlBr<sub>3</sub> [7]. The strong base is needed to cleave the C-H bond of arene to form a nucleophilic carbon atom which can further interact with the weak CO<sub>2</sub> electrophile. The role of the Lewis acid is to activate the CO<sub>2</sub> molecule before the arene C-H bond carboxylation [8]. However, both these strategies usually provide rather low yields of the target products due to the low electrophilicity of CO<sub>2</sub> and side reactions caused by excessive reactivity of the mediators [7, 8]. Therefore, the development of alternative catalytic procedures avoiding the usage of strong base or acid is highly desired but also represents one of the great challenges for this reaction.

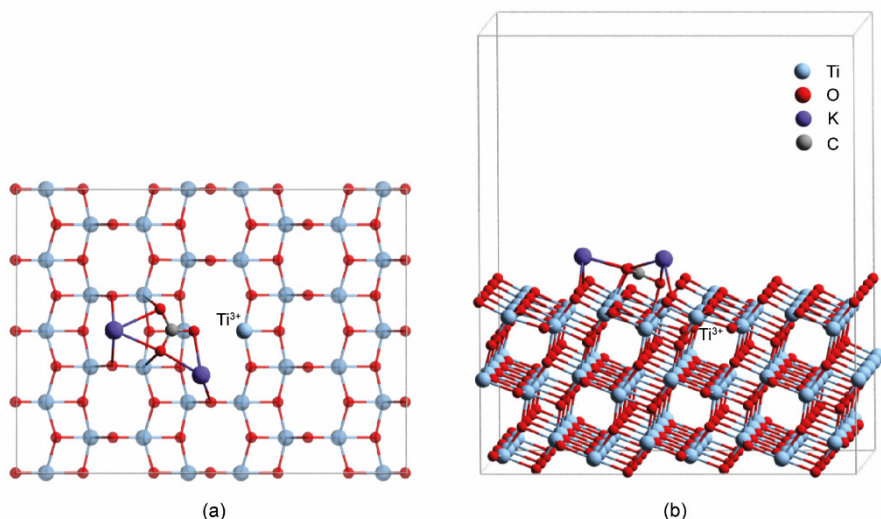
Recently, Kanan et al. reported that alkali carbonates (K<sub>2</sub>CO<sub>3</sub> and Cs<sub>2</sub>CO<sub>3</sub>) finely dispersed over TiO<sub>2</sub> support could promote the two-step cycle of benzene esterification with CO<sub>2</sub> and CH<sub>3</sub>OH to produce methyl benzoate with both high yield (80%) and high selectivity (100%) in the absence of stoichiometric additives [9]. It is important to note that bare TiO<sub>2</sub> can also promote the first step of benzene C-H bond carboxylation, however, the catalyst became deactivated after just one catalyst recycling. In contrast, no carboxylation products were observed when K<sub>2</sub>CO<sub>3</sub> or Cs<sub>2</sub>CO<sub>3</sub> powders as the only component was used. Thus, it was hypothesized that dispersing alkali carbonate over TiO<sub>2</sub> would engender catalytic carboxylation activity towards hydrocarbon substrates because of the disruption of the bulk alkali carbonate structure. However, the mechanistic aspects of this system, such as the nature of the active site and the exact role of the different catalyst components, remained moot. Especially for the initial C-H bond carboxylation with CO<sub>2</sub> many possible mechanisms have been proposed [8]. This inspired us to carry out a comprehensive mechanistic study of benzene carboxylation with CO<sub>2</sub> and subsequent methylation by CH<sub>3</sub>OH over the K<sub>2</sub>CO<sub>3</sub>/TiO<sub>2</sub> catalyst by periodic density functional theory calculations. Our main objective was



to identify the role and function of each catalyst component and to propose the origin of the deactivation of bare  $\text{TiO}_2$  catalyst.

### 3.2 Computational details

In this work, all calculations were performed using the Vienna Ab Initio Simulation Package (VASP) 5.3.5 [10, 11]. DFT calculations were carried out using PBE functional based on the generalized gradient approximation (GGA) [12]. Grimme's DFT-D3 method with Becke-Jonson damping was used to account for the dispersion interactions [13]. The DFT+U method was applied to the 3d orbitals of Ti to correct the on-site Coulomb interactions. The U value used in this work is 4.2 eV [14]. The energy cutoff and convergence criteria used in this study were 400 eV,  $10^{-5}$  eV, and 0.05 eV/Å for the electronic and ionic loops, respectively. Transition states were determined by the nudged-elastic band method with the improved tangent estimate (CI-NEB) and subsequent frequency analysis. The model of  $\text{K}_2\text{CO}_3/\text{TiO}_2$  catalyst was built following the experimental evidence of the very fine dispersion of  $\text{K}_2\text{CO}_3$  on the surface of  $\text{TiO}_2$  [9]. Figure 3.1 shows the catalyst model featuring the  $\text{K}_2\text{CO}_3$  species deposited on the defective anatase  $\text{TiO}_2$  (101) surface. We hypothesized that the interface of coordination-unsaturated surface Ti site ( $\text{Ti}^{3+}$ ) together with the adjacent  $\text{K}_2\text{CO}_3$  cluster form the reactive ensemble because neither the bulk crystalline  $\text{K}_2\text{CO}_3$  nor the pristine  $\text{TiO}_2$  surface are active [9, 15].

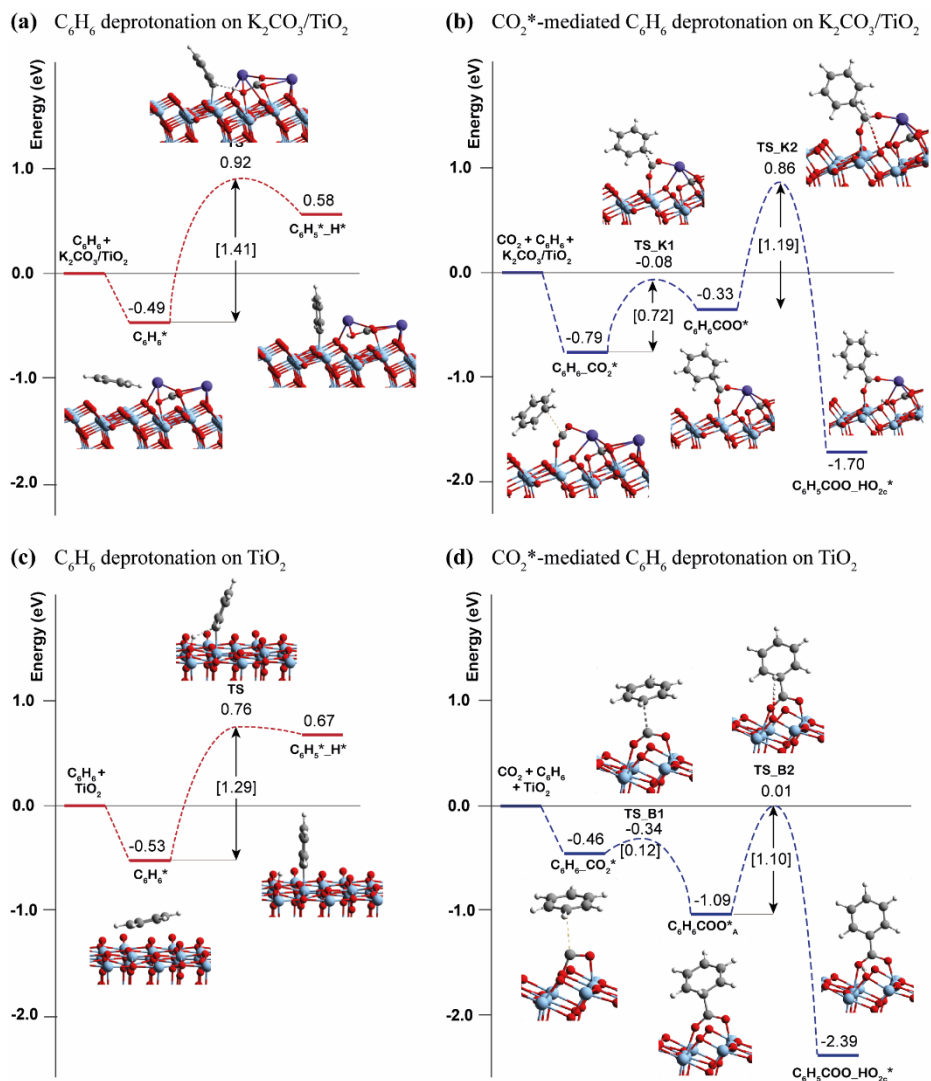


**Figure 3.1** Optimized structure of  $\text{K}_2\text{CO}_3$  supported on defective anatase  $\text{TiO}_2$  (101) surface ( $\text{K}_2\text{CO}_3/\text{TiO}_2$ ). **(a)** and **(b)** are top view and side view, respectively

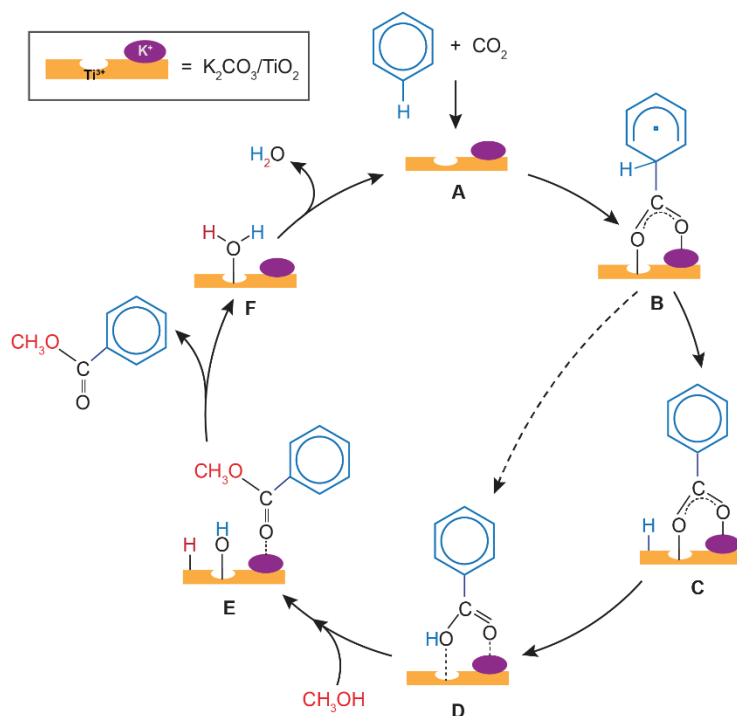
## 3.3 Results

### 3.3.1 Benzene activation and deprotonation

The experimental study hypothesized that the benzene carboxylation mechanism could proceed via benzene deprotonation followed by rapid reaction with  $\text{CO}_2$  to produce a surface-bound carbonate [1].  $\text{K}_2\text{CO}_3$  should then be responsible for the deprotonation reaction, as observed in other hydrocarbon carboxylation reactions promoted by homogeneous catalysts [2, 3]. An alternative mechanism involves a direct C-H bond carboxylation via electrophilic attack by pre-activated  $\text{CO}_2$ , which has also been considered in a number of earlier studies as a viable reaction path [4, 5]. Herein, both reaction pathways were considered by DFT calculations and the respectively computed energetics are shown in Figure 3.2. We found that the deprotonation of  $\text{C}_6\text{H}_6$  (Figure 3.2a) is an endothermic reaction with a rather higher activation barrier ( $\Delta E_{\text{rxn}} = 1.07$  eV,  $E_a = 1.41$  eV). The alternative reaction starts with a much more favourable addition of an activated  $\text{CO}_2^*$  to  $\text{C}_6\text{H}_6$  ( $\Delta E_{\text{rxn}} = 0.46$  eV,  $E_a = 0.72$  eV) followed by an exothermic C-H bond dissociation (Figure 3.2b) ( $\Delta E_{\text{rxn}} = -1.37$  eV,  $E_a = 1.19$  eV). A similar trend is also observed in the case of bare defective  $\text{TiO}_2$  (Figure 3.2c and Figure 3.2d). These results indicate that the  $\text{C}_6\text{H}_6$  deprotonation that Kanan et al.[9] proposed as an initial reaction step for the benzene carboxylation is both thermodynamically and kinetically less favourable than the direct carboxylation route facilitated by  $\text{K}_2\text{CO}_3/\text{TiO}_2$ , which is in line with the substantial carboxylation activity of the carbonate-free  $\text{TiO}_2$  catalyst.



**Figure 3.2** The comparison of computed reaction energy diagrams for  $C_6H_6$  deprotonation and  $CO_2^*$ -mediated  $C_6H_6$  deprotonation on  $K_2CO_3/TiO_2$  and bare defective  $TiO_2$ . **(a)**  $C_6H_6$  deprotonation on  $K_2CO_3/TiO_2$ . **(b)**  $CO_2^*$ -mediated  $C_6H_6$  deprotonation on  $K_2CO_3/TiO_2$ . **(c)**  $C_6H_6$  deprotonation on bare defective  $TiO_2$ . **(d)**  $CO_2^*$ -mediated  $C_6H_6$  deprotonation on bare defective  $TiO_2$ .



**Scheme 3.1** Proposed mechanism of benzene esterification with  $CO_2$  and  $CH_3OH$  on  $K_2CO_3/TiO_2$  catalyst. The  $A + CO_2 + C_6H_6 \rightarrow D$  conversion involves the carboxylation of benzene with  $CO_2$  via the one-step direct (dashed) or stepwise indirect (solid path) mechanisms to yield the adsorbed benzoic acid. The latter is methylated with  $CH_3OH$  ( $D + CH_3OH \rightarrow F + C_6H_5COOCH_3$ ) to yield methyl benzoate product and the adsorbed water. Subsequent desorption of  $H_2O$  by-product ( $F \rightarrow A + H_2O$ ) regenerates the catalytic surface ensemble.

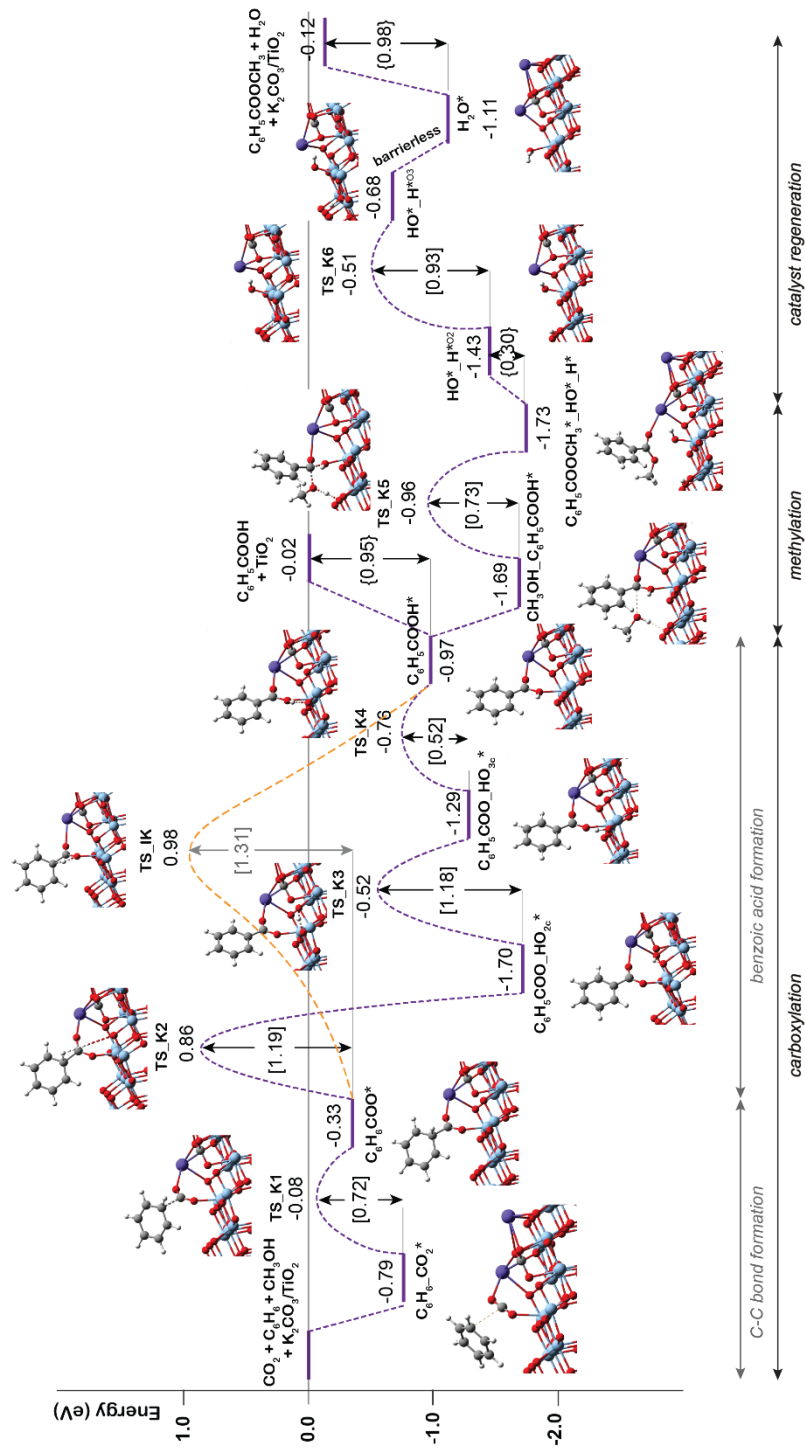
### 3.3.2 Esterification of benzene with $CO_2$ and $CH_3OH$ on $K_2CO_3/TiO_2$

Scheme 3.1 presents a proposed reaction mechanism for the esterification of benzene with  $CO_2$  and  $CH_3OH$  by the  $K_2CO_3/TiO_2$  catalyst. The computed reaction energy profile is shown in Figure 3.3. The previous section showed that the C-H carboxylation of benzene with activated  $CO_2$  is preferred over the alternative mechanism initiated by the  $C_6H_6$  deprotonation. Thus, we proposed that the reaction starts with the adsorption of  $CO_2$  through bidentate coordination with the interface  $Ti^{3+}$  and  $K^+$  sites. It should be noted that the presence of  $K_2CO_3$  prevents a bidentate adsorption mode of  $CO_2$  with two  $Ti^{3+}$  surface atoms, which occur on the bare defective  $TiO_2$  surface. In the next step, the C-C bond formation between the co-adsorbed benzene and  $CO_2^*$  generates the  $C_6H_6COO^*$  intermediate ( $C_6H_6\_CO_2^*$

→ C<sub>6</sub>H<sub>6</sub>COO\*). This step is endothermic with  $\Delta E_{\text{rxn}} = 0.46$  eV and proceeds with activation energy (E<sub>a</sub>) of 0.72 eV.

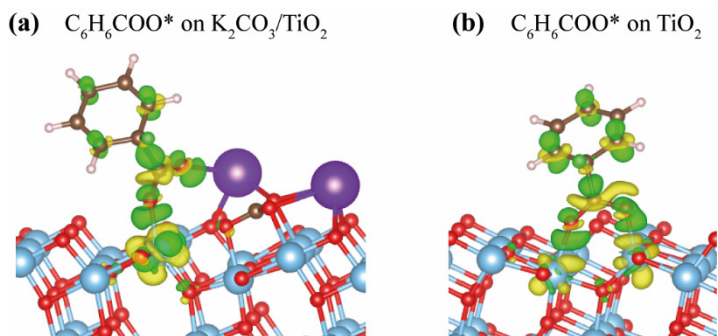
Next, the C-H bond of the activated C<sub>6</sub>H<sub>6</sub> fragment is cleaved to form benzoic acid (C<sub>6</sub>H<sub>5</sub>COOH\*) or benzoate (C<sub>6</sub>H<sub>5</sub>COO\*) surface intermediate. The former is formed via a direct intramolecular H-transfer from the C<sub>6</sub>H<sub>6</sub> moiety of C<sub>6</sub>H<sub>6</sub>COO\* to terminal O of the carboxylate moiety. The computed activation barrier for this step is 1.31 eV. An alternative path involves a two-step surface-assisted H\*-transfer, upon which the C<sub>6</sub>H<sub>6</sub>COO\* intermediate is first deprotonated by the vicinal basic surface O sites (E<sub>a</sub> = 1.19 eV) followed by the C<sub>6</sub>H<sub>5</sub>COO\* and H\* recombination (E<sub>a</sub> = 1.19 eV). The highest activation energy of the indirect route is only ca. 0.10 eV lower than that of the direct pathway, indicating that both reaction routes can contribute to the catalytic reaction. The hydrogen transfer from the C<sub>6</sub>H<sub>6</sub>COO\* to form C<sub>6</sub>H<sub>5</sub>COO\* is predicted to be more difficult than the initial coupling of CO<sub>2</sub> and benzene, which is consistent with the experimentally observed kinetic isotopic effect results [9]. The electronic analysis further indicated that effective charge transfer between intermediates and the defective catalyst surface facilitates the C-C coupling and deprotonation reaction processes (Figure 3.4-3.5). The desorption of benzoic acid to regenerate the catalytic interface is endothermic by 0.95 eV.

The closure of the catalytic cycle can be facilitated in the presence of methanol, which reacts with the surface benzoate intermediate (CH<sub>3</sub>OH\_C<sub>6</sub>H<sub>5</sub>COOH\*) to produce methyl benzoate product (C<sub>6</sub>H<sub>5</sub>COOCH<sub>3</sub>\*\_HO\*\_H\*). During the methylation process, a CH<sub>3</sub>OH molecule is added to the system and co-adsorbed at the neighboring surface oxygen atom of benzoic acid. Then, the methyl benzoate is generated by the formation of the C-O bond between CH<sub>3</sub>OH and benzoic acid. The simultaneous deprotonation of CH<sub>3</sub>OH\* and cleavage of the C-OH bond of C<sub>6</sub>H<sub>5</sub>COOH\* result in the generation of two hydroxyl groups on the surface. This concerted step is slightly exothermic and proceeds with an activation energy of 0.73 eV. In the next step, the methyl benzoate product is desorbed from the surface with  $\Delta E$  of 0.30 eV. The last step is the recombination of surface OH groups to form H<sub>2</sub>O and regenerate the catalytic interface sites (HO\*\_H\*\_O<sub>2</sub> → H<sub>2</sub>O\*). This dehydration step is barrierless but proceeds with a barrier of 0.93 eV associated with the surface migration of H\*. Overall, the hydrogen transfer step following the C-C bond formation in the carboxylation process is the most difficult step along the reaction path, with an activation barrier of 1.31 eV.

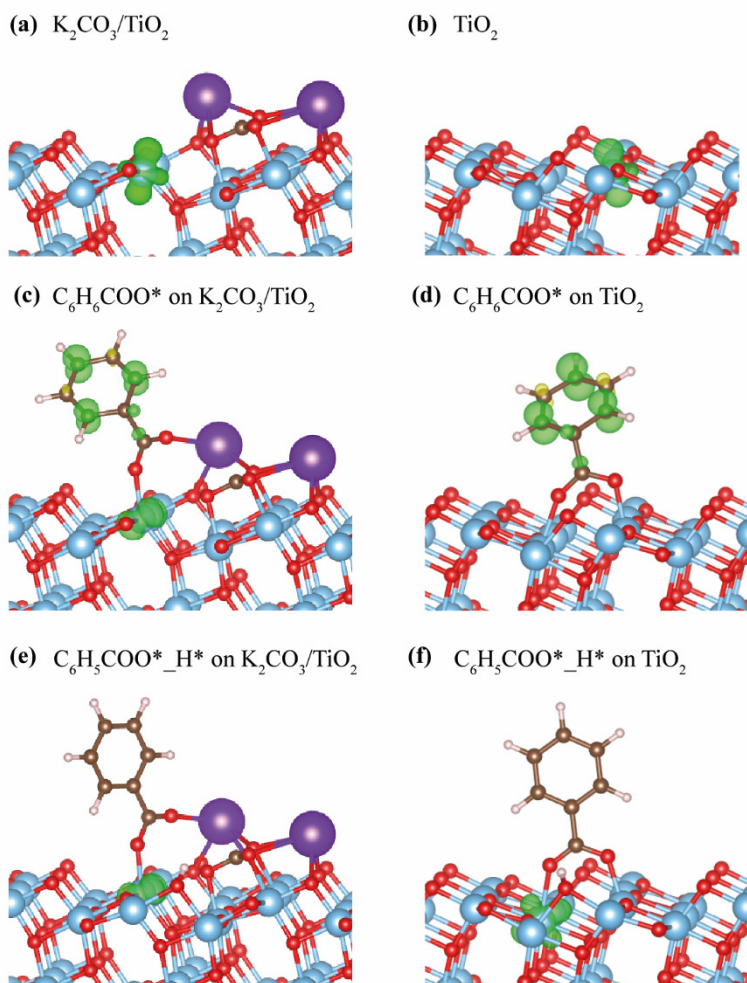


**Figure 3.3** DFT-computed reaction energy diagram for the benzene esterification with  $\text{CO}_2$  and  $\text{CH}_3\text{OH}$  on  $\text{K}_2\text{CO}_3/\text{TiO}_2$ .

**Electronic structure analysis of  $C_6H_6COO^*$ :** For the 1<sup>st</sup> step, which represents carboxylation of benzene with  $CO_2$  forming benzoic acid, the  $C_6H_6COO^*$  is proposed as the first intermediate. The formation of the meta-stable  $C_6H_6COO^*$  species on the surface of the catalyst is facilitated by the interaction of the  $CO_2$  moiety with the  $Ti^{3+}$  and  $K^+$  species (with two  $Ti^{3+}$  in the case of bare  $TiO_2$ ). As shown in Figure 3.4, the reaction is formally a nucleophilic aromatic substitution reaction, which is facilitated by the increased nucleophilicity of  $CO_2$  adsorbed to the defect  $Ti^{3+}$  sites. This mechanistic proposal is supported by the anionic nature of the  $C_6H_6COO^*$  intermediate on  $K_2CO_3/TiO_2$  and bare  $TiO_2$  catalysts as follows from the charge density difference plots.



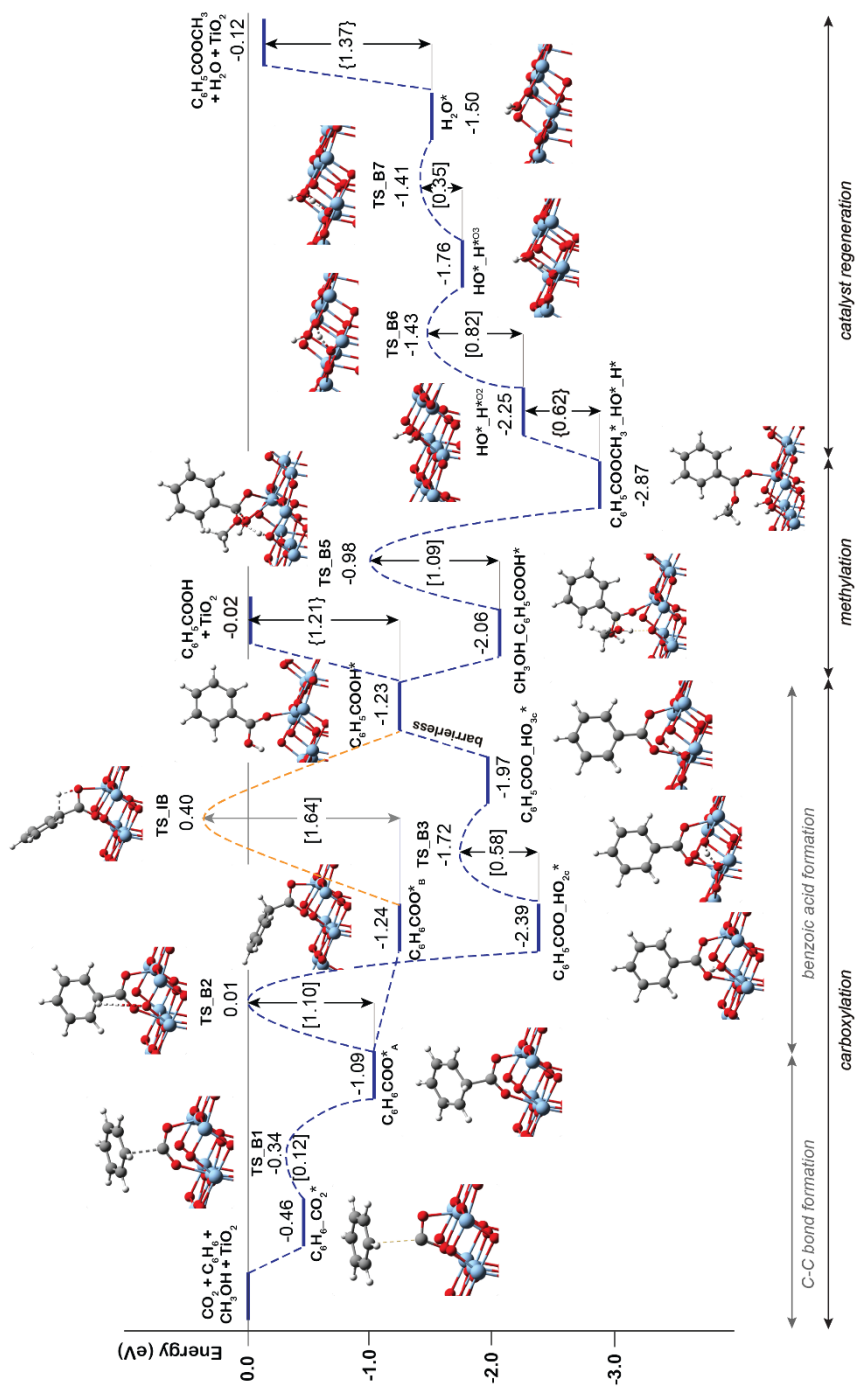
**Figure 3.4** Charge density difference plots of  $C_6H_6COO^*$  adsorbed on (a)  $K_2CO_3/TiO_2$  and (b) bare defective  $TiO_2$ . The green and yellow regions represent enriched and depleted electron density, respectively. The isosurface values are  $0.005 e/Bohr^3$ .



**Figure 3.5** The spin density difference of (a)  $\text{K}_2\text{CO}_3/\text{TiO}_2$ , (b) defective  $\text{TiO}_2$ , (c)  $\text{C}_6\text{H}_6\text{COO}^*$  on  $\text{K}_2\text{CO}_3/\text{TiO}_2$ , (d)  $\text{C}_6\text{H}_6\text{COO}^*$  on  $\text{TiO}_2$ , (e)  $\text{C}_6\text{H}_5\text{COO}^*_\text{H}^*$  on  $\text{K}_2\text{CO}_3/\text{TiO}_2$ , and (f)  $\text{C}_6\text{H}_5\text{COO}^*_\text{H}^*$  on  $\text{TiO}_2$ . Isosurface values are  $0.01 \text{ e}/\text{Bohr}^3$ .

Figure 3.5 illustrates the spin density difference that occurred during the C-H carboxylation of benzene with  $\text{CO}_2$ . Figure 3.5a-b show that the unpaired electron is localized on  $\text{Ti}^{3+}$  site for both bare  $\text{TiO}_2$  and  $\text{K}_2\text{CO}_3/\text{TiO}_2$  catalysts. When  $\text{C}_6\text{H}_6\text{COO}^*$  intermediate was formed (Figure 3.5c-d), redistribution of the unpaired electrons on the benzene ring indicated the formation of a sigma complex. In the next step, Hydride transfer from the benzene ring to the surface, forming  $\text{C}_6\text{H}_5\text{COO}^*_\text{H}^*$  intermediates leading to spin density relocated to the surface (Figure 3.5e-f).





**Figure 3.6** DFT-computed reaction energy diagram for the benzene esterification with CO<sub>2</sub> and CH<sub>3</sub>OH on bare defective TiO<sub>2</sub>.

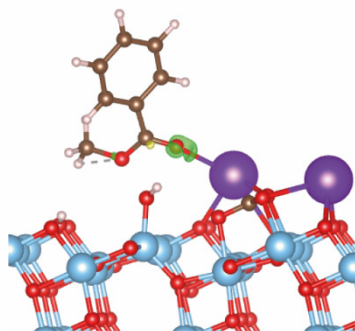
### 3.3.3 Esterification of benzene with CO<sub>2</sub> and CH<sub>3</sub>OH on bare TiO<sub>2</sub>

Previous experimental studies [9] showed that the carbonate-free defective TiO<sub>2</sub> can also promote benzene carboxylation, but it loses the activity already after the first reaction cycle. We therefore hypothesized that the reaction intermediates or the reaction products (e.g. methyl benzoate or water) might block the active site of the bare TiO<sub>2</sub> catalyst, while the presence of K<sub>2</sub>CO<sub>3</sub> species protects catalyst from such poisoning. To check this hypothesis, the DFT analysis was extended to the mechanism of benzene carboxylation followed by methylation on the bare and defective anatase TiO<sub>2</sub> (101) surface. Figure 3.6 presents the respective DFT-computed reaction energy diagram. In this case, the C-C bond formation between CO<sub>2</sub> and benzene is thermodynamically and kinetically more favorable than on the interface site ( $\Delta E_{\text{rxn}} = -0.63$  eV,  $E_a = 0.12$  eV). However, the subsequent H\* transfer to directly form adsorbed benzoic acid is, in this case, 0.3 eV higher than over the K<sub>2</sub>CO<sub>3</sub>/TiO<sub>2</sub>. A much more favorable reaction is the benzoate formation via the hydroxylation of the TiO<sub>2</sub> surface. This step has a barrier of 1.1 eV and stabilizes the system by  $\Delta E_{\text{rxn}}$  of -1.3 eV. Almost identical energetics was observed for the K<sub>2</sub>CO<sub>3</sub>/TiO<sub>2</sub> catalyst. For the subsequent concerted benzoic acid methylation reaction, the activation energy over defective TiO<sub>2</sub> is 0.36 eV higher than that of K<sub>2</sub>CO<sub>3</sub>/TiO<sub>2</sub> catalyst reaction ( $E_a(\text{TS}_{\text{B5}}) = 1.09$  eV vs  $E_a(\text{TS}_{\text{K5}}) = 0.73$  eV).

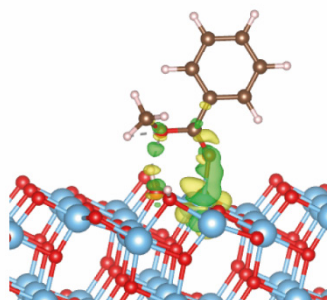
The comparison of the reaction profiles in Figures 3.3 and 3.6 reveals that the activation energies of all elementary steps (except the initial CO<sub>2</sub> coupling with benzene) over the defective TiO<sub>2</sub> surface and K<sub>2</sub>CO<sub>3</sub>-promoted TiO<sub>2</sub> are quite close and comparable suggesting that indeed both catalysts can enable the esterification reaction of benzene with CO<sub>2</sub> and CH<sub>3</sub>OH to form methyl benzoate. However, we find that most of the reaction intermediates on the defective TiO<sub>2</sub> surface are significantly more stable than those on K<sub>2</sub>CO<sub>3</sub>/TiO<sub>2</sub>. The energies of all reaction intermediates on the defective TiO<sub>2</sub> surface are in the range of 0.00 to -3.00 eV, while those on K<sub>2</sub>CO<sub>3</sub>/TiO<sub>2</sub> catalyst fall in the range of +1.00 to -2.00 eV relative to the reactant state. The stronger binding interaction on the bare TiO<sub>2</sub> surface impedes the desorption of the products and regeneration of the active site for the next catalytic cycle. Specifically, the desorption energies of methyl benzoate and H<sub>2</sub>O on the defective TiO<sub>2</sub> surface are 0.39 and 0.32 eV higher than that on K<sub>2</sub>CO<sub>3</sub>/TiO<sub>2</sub>, respectively ( $E_{\text{des}}(\text{C}_6\text{H}_5\text{COOCH}_3)$ : 1.37 eV vs 0.98 eV;  $E_{\text{des}}(\text{H}_2\text{O})$ : 0.62 eV vs 0.30 eV).

**Electronic structure analysis of  $C_6H_5COOCH_3^*$  and  $H_2O^*$ :** The electron density difference plots for  $C_6H_5COOCH_3$  and  $H_2O$  adsorption on  $K_2CO_3/TiO_2$  and defective  $TiO_2$  are shown in Figure 3.7. Upon adsorption, it can be seen that electron transfer takes place between the adsorption sites ( $Ti^{3+}$  and  $K^+$ ) and the oxygen atoms of the adsorbates ( $C_6H_5COOCH_3$  and  $H_2O$ ). For the adsorption of  $C_6H_5COOCH_3$ , it is obvious that the electron transfer between  $C_6H_5COOCH_3$  and  $TiO_2$  is much more significant than that between  $C_6H_5COOCH_3$  and  $K_2CO_3/TiO_2$ , accounting for the stronger interaction and higher desorption barrier. For the adsorption of  $H_2O$  on defective  $TiO_2$ , the accumulation of electrons is observed at both  $Ti^{3+}-O_{H_2O}$  bonds. In the case of  $H_2O$  adsorbed on  $K_2CO_3/TiO_2$ , the accumulation of electrons on the surface is only observed at  $Ti^{3+}$  site, while that on  $K^+$  is negligible. These results indicate the stronger interaction of  $C_6H_5COOCH_3$  and  $H_2O$  on the defective  $TiO_2$ , which is in agreement with the calculated desorption energy.

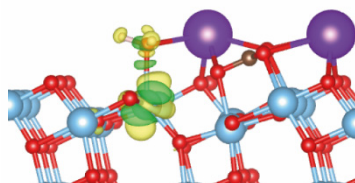
(a)  $C_6H_5COOCH_3^*$  on  $K_2CO_3/TiO_2$



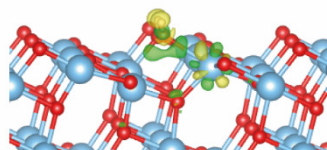
(b)  $C_6H_5COOCH_3^*$  on  $TiO_2$



(c)  $H_2O^*$  on  $K_2CO_3/TiO_2$



(d)  $H_2O^*$  on  $TiO_2$



**Figure 3.7** Charge density difference of (a)  $C_6H_5COOCH_3$  adsorption on  $K_2CO_3/TiO_2$ , (b)  $C_6H_5COOCH_3$  adsorption on defective  $TiO_2$ , (c)  $H_2O$  adsorption on  $K_2CO_3/TiO_2$ , and (d)  $H_2O^*$  adsorption on defective  $TiO_2$ . Green region indicates electron accumulation whereas yellow region indicates electron depletion. Isosurface values are  $0.005 e/Bohr^3$ .

### 3.4 Conclusion

In this work, we conclude that both bare TiO<sub>2</sub> with oxygen vacancy and K<sub>2</sub>CO<sub>3</sub>/TiO<sub>2</sub> catalysts are able to activate CO<sub>2</sub> and benzene to form benzoate products. However, the excessive reactivity of the surface sites in the former results in surface poisoning by the reaction products/by-products. The presence of potassium carbonate species partially deactivates the reactive sites on the titanium surface to facilitate the product desorption and the regeneration of the catalytic interface sites. Although the K<sub>2</sub>CO<sub>3</sub> species cannot act as an active site alone for this reaction, it steers the local structures of the transition states and reaction intermediates, and thus facilitates the products desorption and catalyst regeneration. These insights shed light on the role of multicomponent reaction environments on the catalytic surface for efficient CO<sub>2</sub> valorization. They can form a base for further development of efficient and stable catalysts for the direct carboxylation with CO<sub>2</sub> of other more challenging hydrocarbon substrates such as ethane, methane, and ethylene.

### References

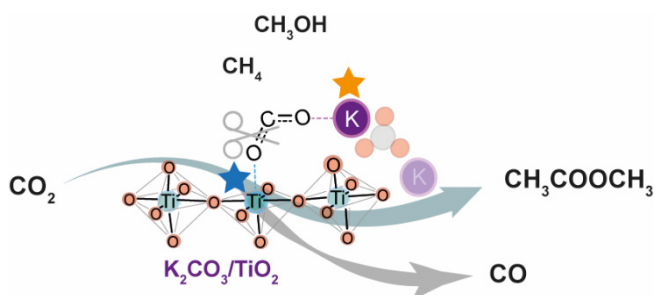
1. Burkart, M.D., N. Hazari, C.L. Tway, and E.L. Zeitler, *Opportunities and Challenges for Catalysis in Carbon Dioxide Utilization*. *ACS Catal.*, 2019. **9**(9): p. 7937-7956.
2. Kamkeng, A.D.N., M. Wang, J. Hu, W. Du, and F. Qian, *Transformation technologies for CO<sub>2</sub> utilisation: Current status, challenges and future prospects*. *J. Chem. Eng.*, 2021. **409**: p. 128138.
3. Hepburn, C., E. Adlen, J. Beddington, E.A. Carter, S. Fuss, N. Mac Dowell, J.C. Minx, P. Smith, and C.K. Williams, *The technological and economic prospects for CO<sub>2</sub> utilization and removal*. *Nature*, 2019. **575**(7781): p. 87-97.
4. Olah, G.A., B. Török, J.P. Joschek, I. Bucsí, P.M. Esteves, G. Rasul, and G.K. Surya Prakash, *Efficient Chemoselective Carboxylation of Aromatics to Arylcarboxylic Acids with a Superelectrophilically Activated Carbon Dioxide–Al<sub>2</sub>Cl<sub>6</sub>/Al System*. *J. Am. Chem. Soc.*, 2002. **124**(38): p. 11379-11391.
5. Lindsey, A.S. and H. Jeskey, *The Kolbe-Schmitt Reaction*. *Chem. Rev.*, 1957. **57**(4): p. 583-620.
6. Luo, J., S. Preciado, P. Xie, and I. Larrosa, *Carboxylation of Phenols with CO<sub>2</sub> at Atmospheric Pressure*. *Eur. J. Chem.*, 2016. **22**(20): p. 6798-6802.
7. Nemoto, K., H. Yoshida, N. Egusa, N. Morohashi, and T. Hattori, *Direct Carboxylation of Arenes and Halobenzenes with CO<sub>2</sub> by the Combined Use of AlBr<sub>3</sub> and R<sub>3</sub>SiCl*. *J. Org. Chem.*, 2010. **75**(22): p. 7855-7862.

8. Luo, J. and I. Larrosa, *C-H Carboxylation of Aromatic Compounds through CO<sub>2</sub> Fixation*. *ChemSusChem*, 2017. **10**(17): p. 3317-3332.
9. Xiao, D.J., E.D. Chant, A.D. Frankhouser, Y. Chen, A. Yau, N.M. Washton, and M.W. Kanan, *A closed cycle for esterifying aromatic hydrocarbons with CO<sub>2</sub> and alcohol*. *Nat. Chem.*, 2019. **11**(10): p. 940-947.
10. Kresse, G. and J. Furthmüller, *Efficiency of ab-initio total energy calculations for metals and semiconductors using a plane-wave basis set*. *Comput. Mater. Sci.*, 1996. **6**(1): p. 15-50.
11. Kresse, G. and J. Furthmüller, *Efficient iterative schemes for ab initio total-energy calculations using a plane-wave basis set*. *Phys. Rev. B*, 1996. **54**(16): p. 11169-11186.
12. Perdew, J.P., K. Burke, and M. Ernzerhof, *Generalized Gradient Approximation Made Simple*. *Phys. Rev. Lett.*, 1996. **77**(18): p. 3865-3868.
13. Grimme, S., S. Ehrlich, and L. Goerigk, *Effect of the damping function in dispersion corrected density functional theory*. *J. Comput. Chem.*, 2011. **32**(7): p. 1456-1465.
14. Song, W., S. Ma, L. Wang, J. Liu, and Z. Zhao, *Theoretical Explanation of the Photogenerated Carrier Separation at the Surface Junction*. *ChemCatChem*, 2017. **9**(23): p. 4340-4344.
15. Sorescu, D.C., W.A. Al-Saidi, and K.D. Jordan, *CO<sub>2</sub> adsorption on TiO<sub>2</sub>(101) anatase: A dispersion-corrected density functional theory study*. *J. Chem. Phys.*, 2011. **135**(12): p. 124701.



## 4

# CH<sub>4</sub> esterification with CO<sub>2</sub> and CH<sub>3</sub>OH on K<sub>2</sub>CO<sub>3</sub>/TiO<sub>2</sub>

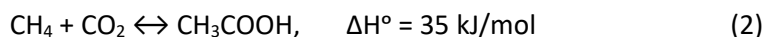
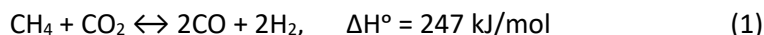


The catalytic activity of K<sub>2</sub>CO<sub>3</sub>/TiO<sub>2</sub> for the two-step cycle of CH<sub>4</sub> esterification with CO<sub>2</sub> and CH<sub>3</sub>OH was investigated computationally and compared with the reaction of C<sub>6</sub>H<sub>6</sub>. Even though the theory predicts that the K<sub>2</sub>CO<sub>3</sub>/TiO<sub>2</sub> can catalyze the carboxylation of CH<sub>4</sub> with CO<sub>2</sub> and the subsequent methylation by CH<sub>3</sub>OH, the reaction is not selective. The formation of side product (CO) competes with the CH<sub>4</sub> carboxylation, while it is not the case for the carboxylation of C<sub>6</sub>H<sub>6</sub>.

## 4.1 Introduction

CO<sub>2</sub> and CH<sub>4</sub> are the primary greenhouse gases that cause the global warming crisis. The development of an effective approach for converting these greenhouse gases into fuels and chemicals is of great importance to environmental sustainability as well as economic benefits. However, using CO<sub>2</sub> and CH<sub>4</sub> as co-feedstocks is still challenging because of their high stability. To date, most studies have focused on the dry reforming of CH<sub>4</sub> with CO<sub>2</sub> to produce syngas (CO and H<sub>2</sub>), followed by either CH<sub>3</sub>OH synthesis or Fischer-Tropsch processes [1]. Nevertheless, the high energy demand and the deactivation of catalysts are the drawbacks of producing syngas.

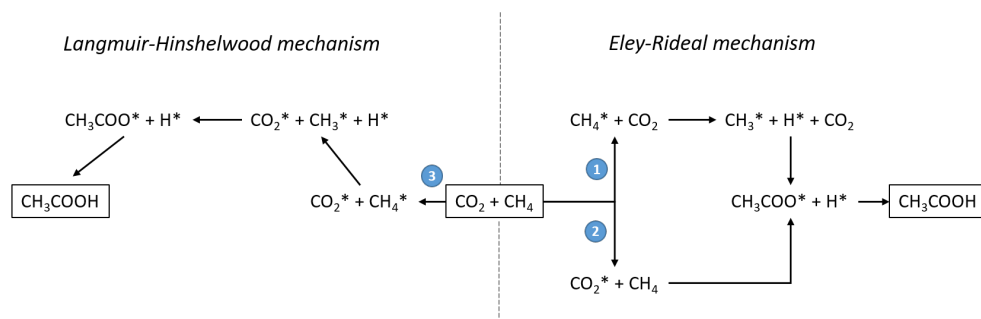
Besides the syngas synthesis, the production of CH<sub>3</sub>COOH by the direct C-C coupling of CH<sub>4</sub> and CO<sub>2</sub> has gained attention due to the 100% atomic efficiency and relatively mild conditions [2]. The CH<sub>3</sub>COOH is an important industrial feedstock to produce value-added chemicals such as vinyl acetate, cellulose acetate, and acetic anhydride [3, 4]. Another advantage of CH<sub>3</sub>COOH production over traditional dry reforming is that it requires much lower enthalpy of the formation ( $\Delta H^\circ$ ), as shown in equations (1) and (2) [5, 6]. However, the high stability of the substrate molecules in this process remains a challenge.



So far, many catalysts have been developed to promote the activation of the challenging CH<sub>4</sub> and CO<sub>2</sub> substrates for the direct CH<sub>3</sub>COOH synthesis. The promising catalyst should be able to activate CH<sub>4</sub> and CO<sub>2</sub> simultaneously as well as stabilize the CH<sub>3</sub>\* species to prevent coke formation from the dehydrogenation process [6]. Thus, using multifunctional heterogeneous catalysts can achieve efficient production of CH<sub>3</sub>COOH. Pd/SiO<sub>2</sub> [7], Rh/SiO<sub>2</sub> [7], Fe/ZnO [8], Zn/CeO<sub>2</sub> [1], and Co/Pd-based TiO<sub>2</sub> [9] are the metal oxide catalysts that have been used for the direct conversion of CO<sub>2</sub> and CH<sub>4</sub> to CH<sub>3</sub>COOH. The overall conversion process contains four elementary reaction steps: (1) the dissociation of CH<sub>4</sub>, (2) the activation of CO<sub>2</sub>, (3) the C-C bond coupling, and (4) the protonation of acetate forming acetic acid [1, 8, 10, 11]. The mechanistic studies by experiments and DFT calculations reveal that this reaction can occur via either the Langmuir-Hinshelwood (LH) or Eley-Rideal (ER) mechanism depending on the types and nature of active sites [2]. The LH mechanism is defined as the reaction of two surface species (CO<sub>2</sub>\* and CH<sub>3</sub>\*) forming acetate intermediate, while the ER



mechanism represents the reaction between adsorbed species and gas-phase molecules. In most cases, the insertion of gas-phase  $\text{CO}_2$  into  $\text{CH}_3^*$  is proposed [1, 10, 11], while the direct interaction between adsorbed  $\text{CO}_2^*$  and gas-phase  $\text{CH}_4$  is rarely reported. Three possible reaction pathways for the conversion of  $\text{CO}_2$  and  $\text{CH}_4$  to  $\text{CH}_3\text{COOH}$  are summarized in Scheme 4.1.



**Scheme 4.1.** Three possible pathways for the direct conversion of  $\text{CH}_4$  and  $\text{CO}_2$  to  $\text{CH}_3\text{COOH}$ .

Considering the active site of catalysts, it was found that the ER mechanism usually occurs on the metal sites, while the LH mechanism dominates on the oxide surfaces. Generally, a Lewis acid-base pair on metal oxide catalysts is responsible for the heterolytic C-H bond dissociation of  $\text{CH}_4$  and the activation of  $\text{CO}_2$  [2]. In some cases, the oxygen vacancies ( $\text{O}_v$ ) on the surface can serve as an active site for activating  $\text{CH}_4$  and  $\text{CO}_2$ . For instance, the  $\text{O}_v$  site of Zn-doped  $\text{CeO}_2$  can facilitate  $\text{CH}_4$  activation [12]. The  $\text{O}_v$  of  $\text{In}_2\text{O}_3$  in  $\text{ZnO}/\text{In}_2\text{O}_3$  catalyst was found to be an active site for adsorption and activation of  $\text{CO}_2$  [13]. In addition, additives such as alkali or alkali earth metals can influence the reactivity of  $\text{CO}_2$ . For example, the addition of alkalis was found to promote the  $\text{CO}_2$  methanation activity of  $\text{Ru}/\text{TiO}_2$  catalyst [14, 15]. The modifications of rutile  $\text{TiO}_2$  with  $\text{MgO}$ ,  $\text{CaO}$ , and  $\text{BaO}$  were found to promote the activation of  $\text{CO}_2$ , forming tridentate carbonate-like species [16]. However, the role of active sites and the mechanisms may change due to the type and nature of catalysts. Therefore, identifying active sites and understanding their role in each elementary reaction step is essential for improving catalytic performance.

Recently, Kanan and co-workers [17] reported the new efficient  $\text{K}_2\text{CO}_3/\text{TiO}_2$  catalyst for the two-step cycle of benzene esterification with  $\text{CO}_2$  and  $\text{CH}_3\text{OH}$ . The first cycle is the benzene C-H bond carboxylation with  $\text{CO}_2$ , while another is the methylation of benzoate with  $\text{CH}_3\text{OH}$  forming methyl ester. Our DFT calculations described in the previous chapter revealed that the  $\text{K}_2\text{CO}_3$  species could prevent catalyst poisoning, whereas the  $\text{O}_v$  surface site significantly affects the catalytic

activity. The interfacial atoms at the proximity of  $O_v$ , such as  $Ti^{3+}-K^+$  and  $Ti^{3+}-O^{2-}$ , are responsible for binding the reactive intermediate [18]. In this chapter, we applied those finding to explore the catalytic potential of  $K_2CO_3/TiO_2$  for a similar reaction but using  $CH_4$  instead of benzene. We expect that the understanding through this study will be useful in the rational design of oxides-based catalysts for the effective direct conversion of  $CH_4$  and  $CO_2$  to produce  $C_{2+}$  chemicals.

## 4.2 Computational details

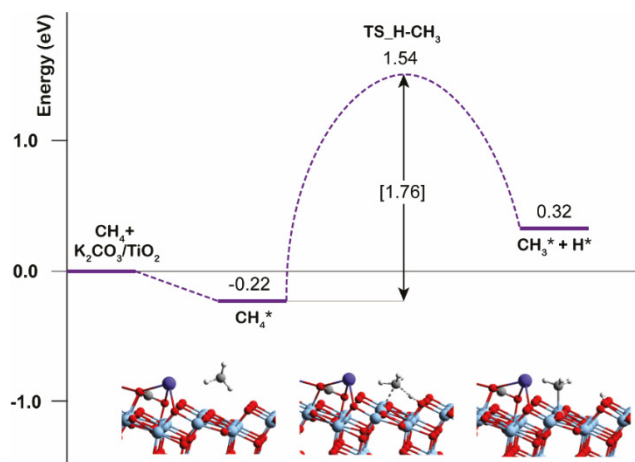
All calculations were performed using the Vienna Ab Initio Simulation Package (VASP) 5.3.5 [19, 20]. DFT calculations were carried out using PBE functional based on the generalized gradient approximation (GGA) [21]. Grimme's DFT-D3 method with Becke-Jonson damping was used to account for the dispersion interactions [22]. The DFT+U method was applied to the 3d orbitals of Ti to correct the on-site Coulomb interactions. The U value used in this work is 4.2 eV [23]. The energy cutoff and convergence criteria for the electronic and ionic loops were 400 eV,  $10^{-5}$  eV, and 0.05 eV/Å, respectively. Transition states were determined by the nudged-elastic band method with the improved tangent estimate (CI-NEB) and subsequent frequency analysis. The model of  $K_2CO_3/TiO_2$  catalyst was built as described in our previous work [18] following the experimental evidence of the very fine dispersion of  $K_2CO_3$  on the surface of  $TiO_2$  [17]. The catalyst model featuring the  $K_2CO_3$  species deposited on the defective anatase  $TiO_2$  (101) surface as the same as shown in Chapter 3 (Figure 3.1). We hypothesized that the interface of coordination-unsaturated surface Ti site ( $Ti^{3+}$ ) together with the 2-coordinated O surface site ( $O_{2c}$ ), and the adjacent  $K_2CO_3$  cluster form the reactive ensemble because neither the bulk crystalline  $K_2CO_3$  nor the pristine  $TiO_2$  surface are active [17, 24].

## 4.3 Results and Discussion

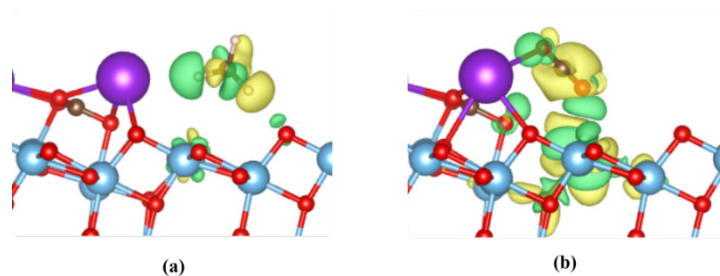
### 4.3.1 The dissociative adsorption of $CH_4$

Both Eley-Rideal (ER) and Langmuir-Hinshelwood (LH) mechanisms were proposed for the coupling of  $CH_4$  and  $CO_2$ , depending on the types and nature of catalysts (Scheme 4.1) [2]. In the first case, a common mechanistic picture involves the dissociation of  $CH_4$  on the catalyst surface followed by the C-C coupling with a gas-phase  $CO_2$ , as shown in the route ① in Scheme 4.1. When taking place on metal oxides, the oxygen vacancy site can promote the adsorption and activation of  $CO_2$ , facilitating thus the coupling of a gas-phase  $CH_4$  over an activated  $CO_2$  (② in Scheme

4.1). In the case of LH mechanism, the product of  $\text{CH}_3\text{COOH}$  is formed via the C-C coupling of two surface species,  $\text{CO}_2^*$  and  $\text{CH}_3^*$ , as shown in route ③ in Scheme 4.1. We, therefore, first considered the dissociative adsorption of  $\text{CH}_4$  on the  $\text{K}_2\text{CO}_3/\text{TiO}_2$  model surface. The respective computed reaction energy diagrams and optimized structures of the key intermediates and transition states are shown in Figure 4.1. Upon adsorption ( $\Delta E_{\text{ads,CH}_4} = -0.22$  eV),  $\text{CH}_4$  coordinates weakly to the open  $\text{Ti}^{3+}$  surface site and forms additional weak  $\text{CH}\cdots\text{O}$  interactions ( $r = 2.20$  Å) with surface oxygen atoms (Figure 4.2a). Next, the C-H bond, which points to the adjacent  $\text{O}_{2c}$  site, is dissociated to form  $\text{CH}_3^*$  on the  $\text{Ti}^{3+}$  site and leaves its H on the  $\text{O}_{2c}$  site as a Brønsted acid. The formally heterolytic C-H cleavage of methane is predicted to be a kinetically difficult ( $E_a = 1.76$  eV) and thermodynamically unfavorable process ( $\Delta E = 0.54$  eV).



**Figure 4.1** Reaction energy diagram for  $\text{CH}_4$  dissociation on  $\text{K}_2\text{CO}_3/\text{TiO}_2$



**Figure 4.2** Electron density difference plots of (a)  $\text{CH}_4^*$ , and (b)  $\text{CO}_2^*$  structures on  $\text{K}_2\text{CO}_3/\text{TiO}_2$ . The green and yellow regions represent enriched and depleted electron density, respectively (isosurface value =  $0.001$  e/Bohr<sup>3</sup>).

For the alternative reaction pathway following ER mechanism (② in Scheme 4.1), the CO<sub>2</sub> adsorption is considered as the initial step. The adsorbed CO<sub>2</sub> interacts with Ti<sup>3+</sup> and K<sup>+</sup> sites through its O atoms. The O-C-O angle is 177.6° implying CO<sub>2</sub> is activated. The adsorption energy of CO<sub>2</sub> is calculated to be -0.40 eV, which is about two times stronger than that of CH<sub>4</sub>. This result is also reflected by a large electron accumulation between O of CO<sub>2</sub> and Ti<sup>3+</sup> surface site, as shown in Figure 4.2b. The electron density plot also indicates the transfer of electrons from CO<sub>2</sub> to the surface, resulting in the electrophilicity of adsorbed CO<sub>2</sub>. Hence, we hypothesize that the carboxylation of CH<sub>4</sub> with CO<sub>2</sub> on the K<sub>2</sub>CO<sub>3</sub>/TiO<sub>2</sub> starts with the CO<sub>2</sub><sup>\*</sup> rather than the CH<sub>4</sub><sup>\*</sup> due to the strong adsorption energy of CO<sub>2</sub> and the high activation energy of CH<sub>4</sub> dissociation. In addition, the difficulty of CH<sub>4</sub> dissociation implies that the LH mechanism (③ in Scheme 4.1) is not the preferred reaction pathway for the coupling of CO<sub>2</sub> and CH<sub>4</sub> on the K<sub>2</sub>CO<sub>3</sub>/TiO<sub>2</sub> catalyst.

### 4.3.2 CH<sub>4</sub> carboxylation with CO<sub>2</sub> to CH<sub>3</sub>COOH

As described in the above section, we propose that CH<sub>3</sub>COOH can be produced on the K<sub>2</sub>CO<sub>3</sub>/TiO<sub>2</sub> catalyst by the C-C coupling of activated CO<sub>2</sub> and gas-phase CH<sub>4</sub>. The reaction mechanism and energy profiles are shown in Figure 4.3. The reaction starts with the adsorption of CO<sub>2</sub> at the interface Ti<sup>3+</sup> and K<sup>+</sup> sites, followed by the physisorption of CH<sub>4</sub> at the nearby O<sub>2c</sub> site (CH<sub>4</sub>\_CO<sup>\*</sup>). Then the C-C coupling of CO<sub>2</sub><sup>\*</sup> and CH<sub>4</sub> occurs simultaneously with the breaking of one C-H bond of CH<sub>4</sub>, forming the CH<sub>3</sub>COO<sup>\*</sup> intermediate and H<sup>\*</sup> on the surface. This reaction is exothermic with an activation barrier of 1.22 eV, which is about 0.50 eV lower than that of the direct C-H bond dissociation of CH<sub>4</sub> on the catalyst. This indicates that CO<sub>2</sub><sup>\*</sup> can facilitate the C-H bond activation of CH<sub>4</sub>, which is similar to the C-H carboxylation of C<sub>6</sub>H<sub>6</sub> with CO<sub>2</sub> discussed in Chapter 3.

In the next step, the proton migration might occur before the protonation of CH<sub>3</sub>COO<sup>\*</sup> due to a long distance between CH<sub>3</sub>COO<sup>\*</sup> and H<sup>\*</sup>\_O<sub>2c</sub> (3.40 Å). The activation energy of the proton migration from the O<sub>2c</sub> to the O<sub>3c</sub> site is about 1.00 eV. After that, the CH<sub>3</sub>COO<sup>\*</sup> is protonated by the H<sup>\*</sup>\_O<sub>3c</sub> forming CH<sub>3</sub>COOH<sup>\*</sup> with an activation barrier of 0.32 eV. The alternative reaction pathway is a direct H-transfer from CH<sub>4</sub> to the terminal O of CO<sub>2</sub><sup>\*</sup> (concerted route). We found that the activation energy of this step is extremely high (E<sub>a</sub> = 2.45 eV), indicating this reaction route is not feasible. It should be noted that this result differs from our previous study in that the carboxylation of C<sub>6</sub>H<sub>6</sub> with CO<sub>2</sub> on the same catalyst can proceed via both stepwise and concerted manners with a small difference in activation energy (ΔE<sub>a</sub> = 0.1 eV).

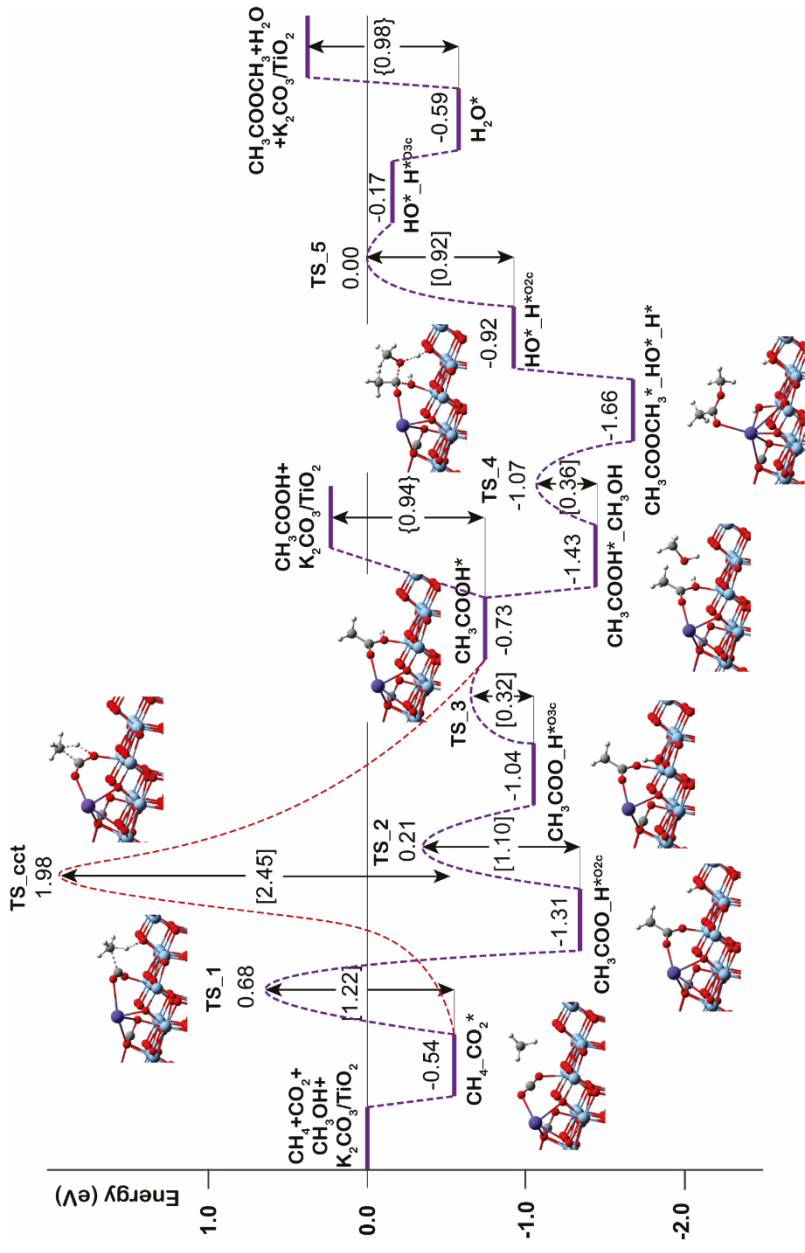


Figure 4.3 Reaction energy profile for the CH<sub>4</sub> carboxylation with CO<sub>2</sub> and subsequent reaction with CH<sub>3</sub>OH on K<sub>2</sub>CO<sub>3</sub>/TiO<sub>2</sub>

### 4.3.3 CH<sub>3</sub>COOH methylation with CH<sub>3</sub>OH to CH<sub>3</sub>COOCH<sub>3</sub>

In this section, the esterification of CH<sub>3</sub>COOH with CH<sub>3</sub>OH by K<sub>2</sub>CO<sub>3</sub>/TiO<sub>2</sub> catalyst is investigated, as shown in Figure 4.3. Similar to the esterification of benzoic acid in Chapter 3, CH<sub>3</sub>OH weakly interacts with the O<sub>2c</sub> surface site and the –OH moiety of acetic acid through its OH group forming CH<sub>3</sub>COOH\*–CH<sub>3</sub>OH complex. Then, the esterification is occurred by forming a C–O bond between the C atom of CH<sub>3</sub>COOH\* and the O atom of CH<sub>3</sub>OH. At the same time, the C–OH bond of CH<sub>3</sub>COOH\* cleaves accompanied by the deprotonation of CH<sub>3</sub>OH producing CH<sub>3</sub>COOCH<sub>3</sub>\* and two hydroxyl groups on the surface (CH<sub>3</sub>COOCH<sub>3</sub>\*–HO\*–H\*). This process is slightly exothermic and proceeds with a small activation energy (E<sub>a</sub> = 0.36 eV). Then, CH<sub>3</sub>COOCH<sub>3</sub> can desorb from the catalyst with a barrier of 0.74 eV. For the last step, the two hydroxyl groups on the surface can form H<sub>2</sub>O and the catalytic active site is regenerated (HO\*–H\*O<sub>3c</sub> → H<sub>2</sub>O\*). This reaction is barrierless, however, H\* migration on the surface needs to overcome a barrier of 0.92 eV before H<sub>2</sub>O formation. The desorption energy of H<sub>2</sub>O is calculated to be 0.98 eV. Overall, the C–C coupling of CO<sub>2</sub> with CH<sub>4</sub> is identified as the most difficult step of the reaction, with the highest activation barrier of 1.22 eV along the reaction coordinate.

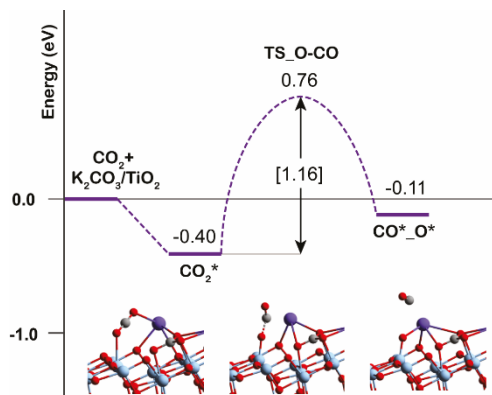
### 4.3.4 Product selectivity and comparison between CH<sub>4</sub> and benzene

We also studied the dissociation of CO<sub>2</sub>\* to CO\* because this reaction might be a competitive pathway to the production of CH<sub>3</sub>COOH. As shown in Figure 4.4, the dissociation of CO<sub>2</sub> occurred by the C–O bond cleavage forming CO, while a leaving O atom from CO<sub>2</sub> occupies the unsaturated Ti<sup>3+</sup> surface site. This process is slightly endothermic, with an activation energy of 1.16 eV. The moderate activation energy indicates that the direct dissociation of CO<sub>2</sub> to CO on K<sub>2</sub>CO<sub>3</sub>/TiO<sub>2</sub> is possible.

We further compared the coupling of CO<sub>2</sub>\* and CH<sub>4</sub> (Figure 4.5a) with the direct conversion of CO<sub>2</sub>\* to CO\*. The results show that the activation energy difference between both reactions is very small (ΔE<sub>a</sub> = 0.06 eV). Thus, CO might be observed as a side product of the reaction, whereas the oxidation of Ti<sup>3+</sup> to Ti<sup>4+</sup> during this process could deactivate the catalyst.

In the case of benzene (Figure 4.5b), the activation energy of C–H carboxylation with CO<sub>2</sub> was calculated to be 1.19 eV. This energy is almost identical to the CO formation (1.16 eV) and the C–H carboxylation with CO<sub>2</sub> in CH<sub>4</sub> (1.22 eV). So, it seems that the formation of CO could compete with the production of benzoate. However, the experimental results showed high selectivity to benzoate (88–91%).

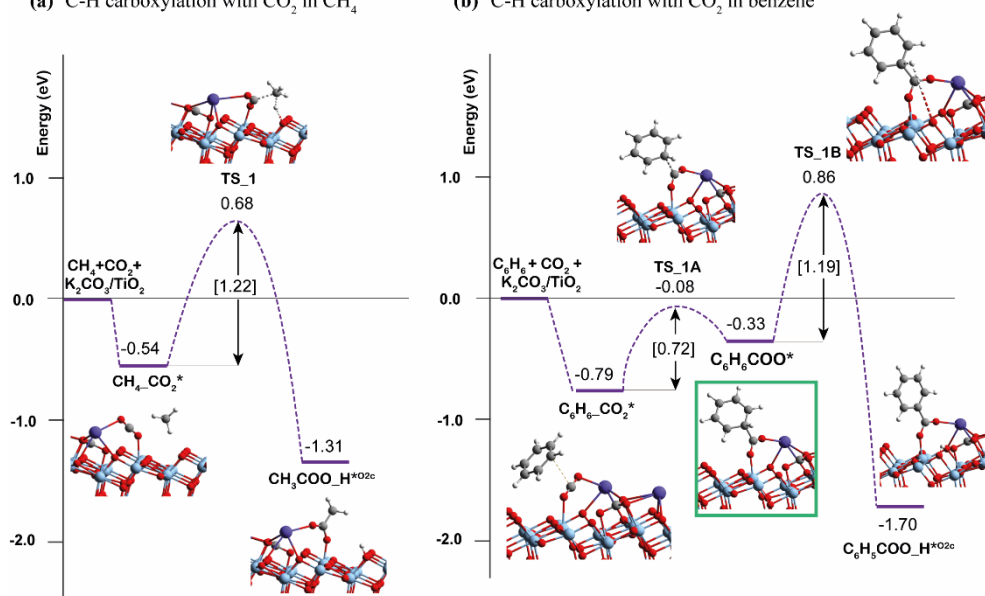
We hypothesize that the formation of metastable  $C_6H_6COO^*$  is a key to the high selectivity of benzoate. As shown in Figure 4.5, the C-H carboxylation with  $CO_2$  in  $CH_4$  proceeds in one step without forming an intermediate, while benzene occurs in two-step reactions via the  $C_6H_6COO^*$ . The formation of such metastable intermediate is due to the aromaticity of benzene, as described in Chapter 3. This process requires an activation energy of 0.72 eV, which is significantly lower than the conversion of  $CO_2$  to CO. Thus, this result can explain why the C-H carboxylation of benzene with  $CO_2$  dominates over the decomposition of  $CO_2$ .



**Figure 4.4.** Reaction energy diagram for  $CO_2$  dissociation on  $K_2CO_3/TiO_2$

(a) C-H carboxylation with  $CO_2$  in  $CH_4$

(b) C-H carboxylation with  $CO_2$  in benzene



**Figure 4.5.** Reaction energy diagram for the C-H carboxylation with  $CO_2$  in (a)  $CH_4$  and (b) benzene

## 4.4 Conclusion

Our previous computational study [18] and experimental study from Kanan et al. [17] showed that the  $\text{K}_2\text{CO}_3/\text{TiO}_2$  is an efficient catalyst for benzene esterification with  $\text{CO}_2$  and  $\text{CH}_3\text{OH}$ . Hence, we further extend this system to study other hydrocarbon carboxylation and further esterification. In this study,  $\text{CH}_4$  is used as a representative of non-aromatic compounds. The results indicate that  $\text{K}_2\text{CO}_3/\text{TiO}_2$  is an efficient catalyst for the esterification of both benzoic acid and acetic acid with  $\text{CH}_3\text{OH}$ . For the carboxylation reaction, the  $\text{K}_2\text{CO}_3/\text{TiO}_2$  can catalyze both  $\text{C}_6\text{H}_6$  and  $\text{CH}_4$  carboxylation with  $\text{CO}_2$ . However, it is interesting to note that the side reaction, which is the formation of  $\text{CO}$ , could compete with the  $\text{CH}_4$  carboxylation, while it is not the case for the  $\text{C}_6\text{H}_6$  carboxylation reaction. Therefore, we expect the low selectivity of carboxylate when using a non-aromatic compound as a reactant for the carboxylation with  $\text{CO}_2$  on  $\text{K}_2\text{CO}_3/\text{TiO}_2$  catalyst. To improve product selectivity, enhancing the Lewis basic strength of the  $\text{O}_{2c}$  site by replacing  $\text{Ti}^{4+}$  with a lower-valence cation might be one of the strategies to facilitate the C-H bond activation of  $\text{CH}_4$ , which is the most difficult step of the reaction.

## References

1. Zhao, Y., C. Cui, J. Han, H. Wang, X. Zhu, and Q. Ge, *Direct C–C Coupling of  $\text{CO}_2$  and the Methyl Group from  $\text{CH}_4$  Activation through Facile Insertion of  $\text{CO}_2$  into  $\text{Zn–CH}_3$   $\sigma$ -Bond*. *J. Am. Chem. Soc.*, 2016. **138**(32): p. 10191-10198.
2. Tu, C., X. Nie, and J.G. Chen, *Insight into Acetic Acid Synthesis from the Reaction of  $\text{CH}_4$  and  $\text{CO}_2$* . *ACS Catal.*, 2021. **11**(6): p. 3384-3401.
3. Martín-Espejo, J.L., J. Gandara-Loe, J.A. Odriozola, T.R. Reina, and L. Pastor-Pérez, *Sustainable routes for acetic acid production: Traditional processes vs a low-carbon, biogas-based strategy*. *Sci. Total Environ.*, 2022. **840**: p. 156663.
4. Merli, G., A. Becci, A. Amato, and F. Beolchini, *Acetic acid bioproduction: The technological innovation change*. *Sci. Total Environ.*, 2021. **798**: p. 149292.
5. Arora, S. and R. Prasad, *An overview on dry reforming of methane: strategies to reduce carbonaceous deactivation of catalysts*. *RSC Adv.*, 2016. **6**(110): p. 108668-108688.
6. Alcantara, M.L., K.A. Pacheco, A.E. Bresciani, and R.M. Brito Alves, *Thermodynamic Analysis of Carbon Dioxide Conversion Reactions. Case Studies: Formic Acid and Acetic Acid Synthesis*. *Ind. Eng. Chem. Res.*, 2021. **60**(25): p. 9246-9258.

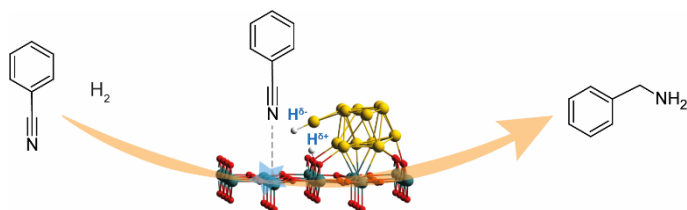


7. Ding, Y.-H., W. Huang, and Y.-G. Wang, *Direct synthesis of acetic acid from CH<sub>4</sub> and CO<sub>2</sub> by a step-wise route over Pd/SiO<sub>2</sub> and Rh/SiO<sub>2</sub> catalysts*. *Fuel Process. Technol.*, 2007. **88**(4): p. 319-324.
8. Nie, X., X. Ren, C. Tu, C. Song, X. Guo, and J. G. Chen, *Computational and experimental identification of strong synergy of the Fe/ZnO catalyst in promoting acetic acid synthesis from CH<sub>4</sub> and CO<sub>2</sub>*. *Chem. Commun.*, 2020. **56**(28): p. 3983-3986.
9. Huang, W., W.Z. Sun, and F. Li, *Efficient synthesis of ethanol and acetic acid from methane and carbon dioxide with a continuous, stepwise reactor*. *AIChE J.*, 2010. **56**(5): p. 1279-1284.
10. Montejo-Valencia, B.D., Y.J. Pagán-Torres, M.M. Martínez-Iñesta, and M.C. Curet-Arana, *Density Functional Theory (DFT) Study To Unravel the Catalytic Properties of M-Exchanged MFI, (M = Be, Co, Cu, Mg, Mn, Zn) for the Conversion of Methane and Carbon Dioxide to Acetic Acid*. *ACS Catal.*, 2017. **7**(10): p. 6719-6728.
11. Wang, S., S. Guo, Y. Luo, Z. Qin, Y. Chen, M. Dong, J. Li, W. Fan, and J. Wang, *Direct synthesis of acetic acid from carbon dioxide and methane over Cu-modulated BEA, MFI, MOR and TON zeolites: a density functional theory study*. *Catal. Sci. Technol.*, 2019. **9**(23): p. 6613-6626.
12. Zhao, Y., H. Wang, J. Han, X. Zhu, and Q. Ge, *Active Site Ensembles Enabled C–C Coupling of CO<sub>2</sub> and CH<sub>4</sub> for Acetone Production*. *J. Phys. Chem. C*, 2018. **122**(17): p. 9570-9577.
13. Zhao, Y., H. Wang, J. Han, X. Zhu, D. Mei, and Q. Ge, *Simultaneous Activation of CH<sub>4</sub> and CO<sub>2</sub> for Concerted C–C Coupling at Oxide–Oxide Interfaces*. *ACS Catal.*, 2019. **9**(4): p. 3187-3197.
14. Petala, A. and P. Panagiotopoulou, *Methanation of CO<sub>2</sub> over alkali-promoted Ru/TiO<sub>2</sub> catalysts: I. Effect of alkali additives on catalytic activity and selectivity*. *Appl. Catal. B*, 2018. **224**: p. 919-927.
15. Panagiotopoulou, P., *Methanation of CO<sub>2</sub> over alkali-promoted Ru/TiO<sub>2</sub> catalysts: II. Effect of alkali additives on the reaction pathway*. *Appl. Catal. B*, 2018. **236**: p. 162-170.
16. Nolan, M., *Alkaline earth metal oxide nanocluster modification of rutile TiO<sub>2</sub> (110) promotes water activation and CO<sub>2</sub> chemisorption*. *J. Mater. Chem. A*, 2018. **6**(20): p. 9451-9466.
17. Xiao, D.J., E.D. Chant, A.D. Frankhouser, Y. Chen, A. Yau, N.M. Washton, and M.W. Kanan, *A closed cycle for esterifying aromatic hydrocarbons with CO<sub>2</sub> and alcohol*. *Nat. Chem.*, 2019. **11**(10): p. 940-947.
18. Meeprasert, J., G. Li, and E.A. Pidko, *Mechanistic investigation of benzene esterification by K<sub>2</sub>CO<sub>3</sub>/TiO<sub>2</sub>: the catalytic role of the multifunctional interface*. *Chem. Commun.*, 2021. **57**(64): p. 7890-7893.

19. Kresse, G. and J. Furthmüller, *Efficiency of ab-initio total energy calculations for metals and semiconductors using a plane-wave basis set*. *Comput. Mater. Sci.*, 1996. **6**(1): p. 15-50.
20. Kresse, G. and J. Furthmüller, *Efficient iterative schemes for ab initio total-energy calculations using a plane-wave basis set*. *Phys. Rev. B*, 1996. **54**(16): p. 11169-11186.
21. Perdew, J.P., K. Burke, and M. Ernzerhof, *Generalized Gradient Approximation Made Simple*. *Phys. Rev. Lett.*, 1996. **77**(18): p. 3865-3868.
22. Grimme, S., S. Ehrlich, and L. Goerigk, *Effect of the damping function in dispersion corrected density functional theory*. *J. Comput. Chem.*, 2011. **32**(7): p. 1456-1465.
23. Song, W., S. Ma, L. Wang, J. Liu, and Z. Zhao, *Theoretical Explanation of the Photogenerated Carrier Separation at the Surface Junction*. *ChemCatChem*, 2017. **9**(23): p. 4340-4344.
24. Sorescu, D.C., W.A. Al-Saidi, and K.D. Jordan, *CO<sub>2</sub> adsorption on TiO<sub>2</sub>(101) anatase: A dispersion-corrected density functional theory study*. *J. Chem. Phys.*, 2011. **135**(12): p. 124701.

## 5

# Benzonitrile hydrogenation on $\text{Au}_{13}/\text{TiO}_2$



Density Functional Theory is used to determine the reaction mechanisms of benzonitrile hydrogenation to benzylamine on  $\text{Au}_{13}$  cluster supported on a rutile  $\text{TiO}_2$  (110) catalyst. An  $\text{Au}/\text{TiO}_2$  interface is identified as an active site for the dissociation of  $\text{H}_2$  and the hydrogenation of benzonitrile. The CN moiety of the benzonitrile substrate is polarized by the adsorption to Lewis acidic Ti center. The generated hydride-proton pair is necessary for reducing the polar CN moiety, facilitating the subsequent hydrogenation reaction.

*This chapter is partially based on ACS Catal, 2021, 11(13), 7672-7684.*

## 5.1 Introduction

Benzylamine is an important chemical compound with widespread applications in the textile, agrochemical, and pharmaceutical industries [1, 2]. There are three main classical production paths of benzylamine summarized in Figure 5.1. The first method is the chlorination of toluene to benzyl chloride, followed by the reaction with ammonia to produce the target benzylamine compound [2, 3]. Despite its simplicity, the use of toxic chlorine gas as the key reagent as well as the accompanying non-selective conversion and generation of substantial amounts of inorganic wastes render this method the least environmentally friendly. The second route starts with the high-temperature ammoxidation of toluene to benzonitrile followed by the catalytic hydrogenation to form benzylamine. Alternatively, the selective oxidation of toluene can be used to generate benzaldehyde, which is then converted to benzylamine via the reductive amination reaction. Although the latter two methods are substantially more environmentally friendly and efficient, there are some significant drawbacks. The ammoxidation of toluene to benzonitrile is limited mostly to nonfunctionalized substrates due to the high temperature and pressure used [4, 5]. Whereas the formation of benzaldehyde can be performed under relatively mild conditions, it suffers from overoxidation to benzoic acid [6].

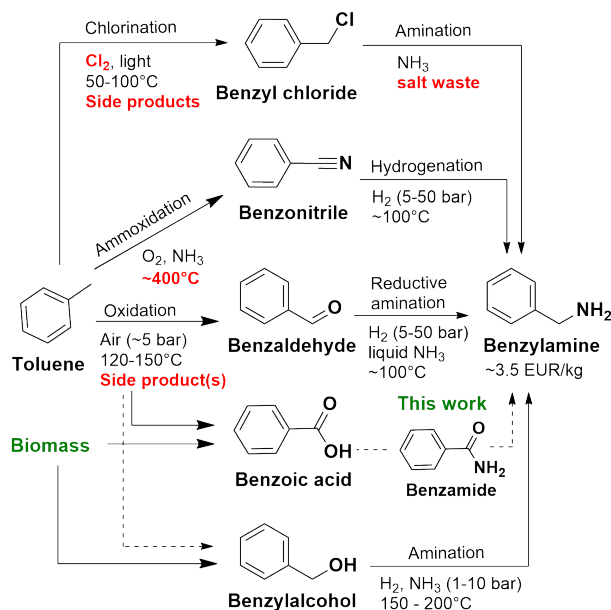
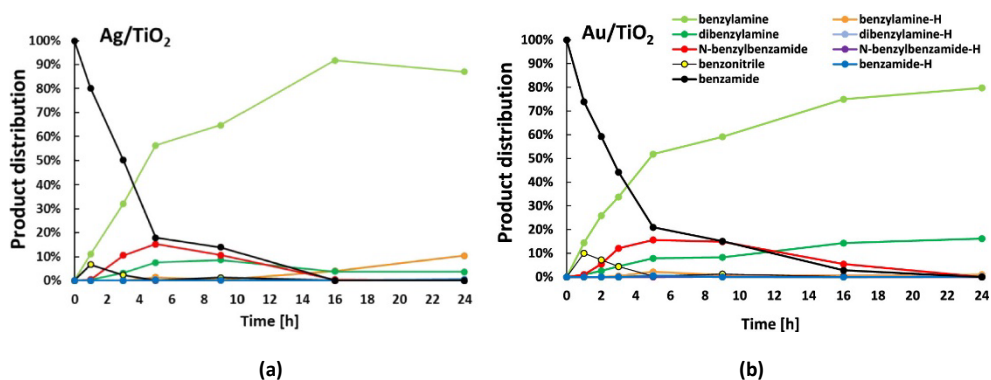


Figure 5.1 An overview of benzylamine synthesis methods [7].

In the past decades, many studies have attempted to synthesize benzylamine efficiently from green and renewable resources under milder conditions. An attractive substrate for such a process is the biomass-derived benzyl alcohol that can be converted to benzylamine via the direct amination reaction with yields ranging between 66–86% [8–14]. An even more desirable substrate is benzoic acid which is generally more abundant, cheaper, and readily obtained from renewable feedstocks [15, 16]. Conventional routes from the benzoic acid or its derivatives to benzylamine would require multistep synthetic procedures and/or the use of stoichiometric reducing agents, inevitably resulting in selectivity losses and/or substantial waste generation. A catalytic conversion path utilizing molecular H<sub>2</sub> as the reducing and NH<sub>3</sub> as the amination agent is highly desirable for high atom- and energy efficiency.



**Figure 5.2** Time profiles for the hydrogenation of benzamide with (a) Ag/TiO<sub>2</sub> and (b) Au/TiO<sub>2</sub>. Reaction conditions: benzamide (2 mmol), 200 °C, 6 bar NH<sub>3</sub>, 30 bar H<sub>2</sub> (Au) or 50 bar H<sub>2</sub> (Ag), 1 mol % Au (1 wt % Au catalyst) or 5 mol % Ag (2.5 wt % Ag catalyst), undecane (internal standard, 40 μL), and CPME (20 mL). (Product names ending with “-H” have at least one aromatic ring that is hydrogenated toward a cyclohexyl moiety.) [7]

Previous studies demonstrated that hydrogenation and reductive amination of aliphatic amides and carboxylic acids could indeed provide a sustainable route to amines [17, 18]. However, these methodologies based on noble metal catalysts such as Ru, Rh, Pd, and Pt were not applicable to the conversion of aromatic substrates because of their high reactivity towards the aromatic ring hydrogenation. Very recently, the experimental studies by De Vos group at KU Leuven identified Ag/TiO<sub>2</sub> and Au/TiO<sub>2</sub> as highly efficient catalysts for the reductive amination of benzoic acid and its derivatives (e.g. benzamide) to produce benzylamine by using only H<sub>2</sub> and NH<sub>3</sub> as the reagents [7]. In particular, the experimental studies demonstrated high selectivity for conversion of benzamide to

benzylamine in the presence of  $\text{H}_2$  and  $\text{NH}_3$  over  $\text{TiO}_2$ -supported Au and Ag catalysts. At the high conversion levels, the formation of dibenzylamine and *N*-benzylbenzamide was observed, while no notable over hydrogenation activity of the aromatic ring was detected (Figure 5.2). The optimized reaction conditions allowed obtaining benzylamine in yields ranging 80-92%. The experimental analysis has led to a mechanistic proposal for the direct catalytic conversion of benzamide to benzylamine illustrated in Figure 5.3, in which the specific role of Au/ $\text{TiO}_2$  catalyst was ascribed to the highly selective and efficient hydrogenation of the polar  $-\text{CN}$  moiety in the benzamide intermediate. However, the origin of this unique reactivity and the role of the multifunctional interface in it were unclear. To clarify these issues and provide mechanistic support to our experimental collaborators from the de Vos group, I investigated the mechanism of benzonitrile hydrogenation to benzylamine over a model Au/ $\text{TiO}_2$  catalyst by periodic Density Functional Theory (DFT) calculations.

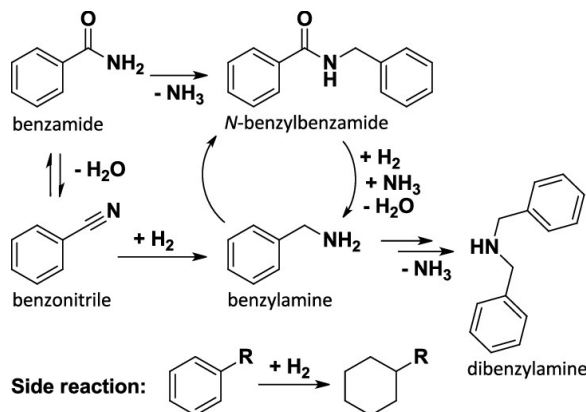


Figure 5.3 Reaction scheme for the hydrogenation of benzamide to benzylamine [7].

## 5.2 Computational details

All periodic Density Functional Theory (DFT) calculations were carried out using the Vienna Ab Initio Simulation Package (VASP) 5.3.5 [19, 20]. The generalized gradient approximation (GGA) with PBE exchange-correlation functional was used [21]. Grimme's DFT-D3 method with Becke-Jonson damping was used to account for the dispersion interactions [22]. The on-site Coulomb interaction was included using the DFT+U method with a Hubbard parameter of  $U = 4.2$  eV for the Ti atoms [23]. The kinetic energy cutoff of the plane wave basis set was set to 400 eV. The threshold for the energy convergence for each electronic optimization iteration

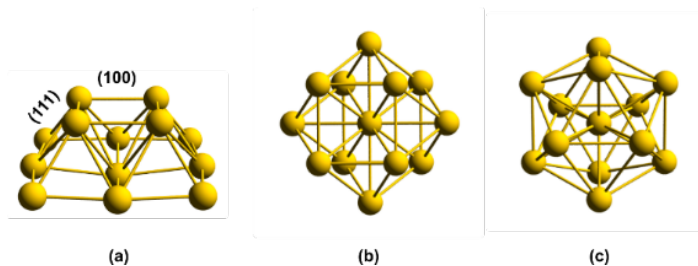
was set to  $10^{-5}$  eV, while the geometry optimizations were assumed to be converged when forces on each atom were less than  $0.05$  eV/Å.

The Gibbs free energy profiles were estimated by considering only the entropy losses due to the adsorption of molecular species on the catalyst surface and the formation of the adsorption complex ( $G_{complex}$ ), which were calculated by:

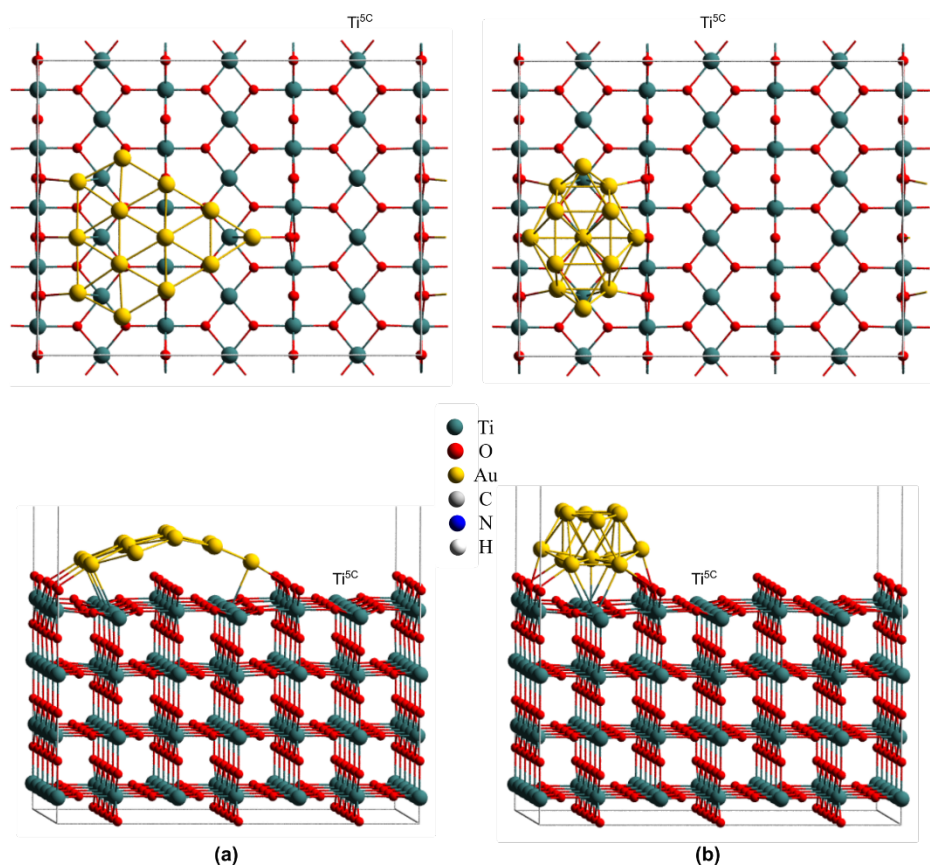
$$G_{complex} = [E_{complex} - E_{Au_{13}/TiO_2} - \sum (E_{adsorbate} + TS_{rot} + TS_{trans})]$$

where  $E_{complex}$ ,  $E_{Au_{13}/TiO_2}$ , and  $E_{adsorbate}$  are the electronic energy of adsorption complex, bare  $Au_{13}/TiO_2$  and the adsorbate, respectively. The  $TS_{rot}$  and  $TS_{trans}$  are the rotational and translational entropy contribution to the energy of the gas-phase adsorbate at the corresponding reaction temperature, respectively. Note, that the zero-point energy (ZPE) is neglected in our calculations.

To construct the model of  $Au_{13}/TiO_2$  catalyst, the rutile  $TiO_2$  (110) surface with a  $p(3 \times 5)$  supercell size as the support following the experimental results. The  $Au_{13}$  cluster size was selected because it is small enough to be computationally feasible and large enough to provide a hemispherical shape in contact with the substrate, mimicking that seen in experiments [24]. In addition, the  $Au_{13}$  has been used as a representative of supported Au particles on  $TiO_2$  for the chemoselective hydrogenation of nitroaromatic compounds [25]. Previous DFT study demonstrated that the supported  $Au_{13}$  cluster could form either planar (2D) or 3D structures on the  $TiO_2$  (110) surface [26, 27]. Therefore, both configurations were considered in this study. For the 3D  $Au_{13}$  cluster supported on  $TiO_2$ , three different configurations (Figure 5.4) were constructed and deposited on the  $TiO_2$  (110) surface. These starting configurations were selected based on the literature data [28, 29]. The DFT calculations revealed that the planar  $Au_{13}$ -2D/ $TiO_2$  (Figure 5.5a) is 0.62 eV more stable than the most favorable 3D structure of  $Au_{13}$  cluster on  $TiO_2$  ( $Au_{13}$ -3D/ $TiO_2$ , Figure 5.5b). Thus, both  $Au_{13}$ -2D/ $TiO_2$  and  $Au_{13}$ -3D/ $TiO_2$  structures were considered as representative model catalysts in the mechanistic analysis of the catalytic benzonitrile hydrogenation because the energy difference is not very significant.

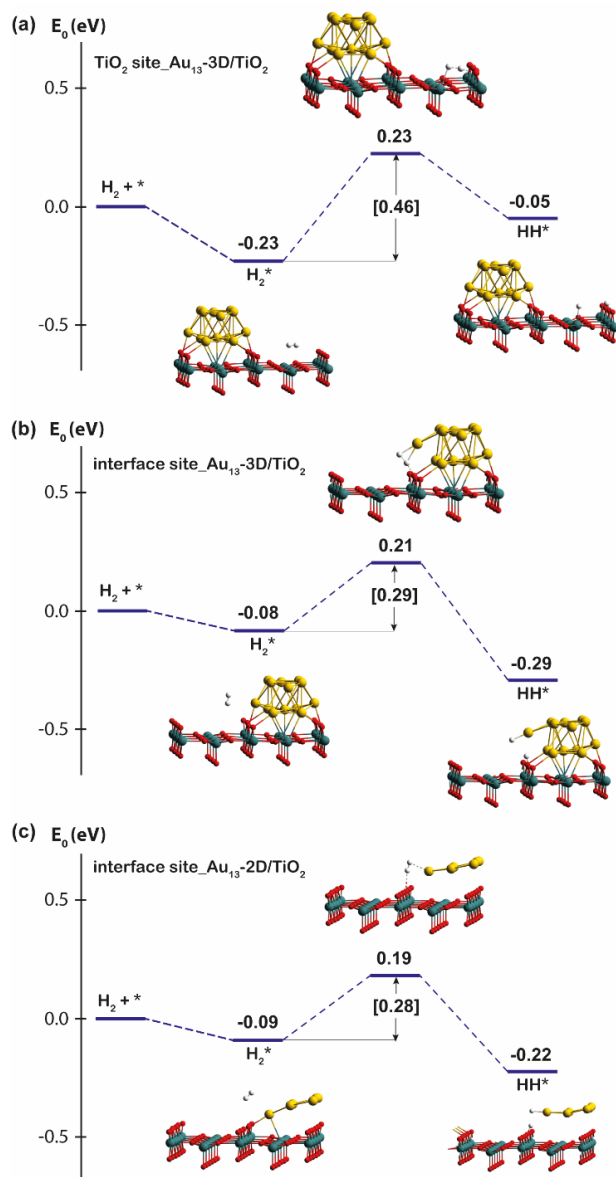


**Figure 5.4** Optimized structures of Au<sub>13</sub>-3D cluster with different geometry. **(a)** Au<sub>13</sub> cluster as extracted from bulk Au, **(b)** octahedral Au<sub>13</sub> cluster, and **(c)** icosahedral Au<sub>13</sub> cluster.



**Figure 5.5** Structural configurations of Au<sub>13</sub> clusters deposited on the stoichiometric rutile TiO<sub>2</sub> (110) surface. **(a)** top and side view of Au<sub>13</sub>-2D/TiO<sub>2</sub>. **(b)** top and side view of the most stable configuration of Au<sub>13</sub>-3D/TiO<sub>2</sub>.





**Figure 5.6** DFT-computed reaction energy profiles of H<sub>2</sub> dissociation on (a) a TiO<sub>2</sub> site and (b) interfacial sites of Au<sub>13</sub>-3D/TiO<sub>2</sub>, and on (c) an interfacial site of Au<sub>13</sub>-2D/TiO<sub>2</sub>

## 5.3 Results and Discussion

### 5.3.1 H<sub>2</sub> dissociation on Au<sub>13</sub>/TiO<sub>2</sub>

Previous studies of H<sub>2</sub> dissociation on bare rutile TiO<sub>2</sub> (110) [30] and Au/TiO<sub>2</sub> (110) [31, 32] found that the heterolytic dissociation is favored in comparison with the homolytic H<sub>2</sub> activation. Thus, only the former mechanism, which is the H<sub>2</sub> cleavage to produce a couple of proton (H<sup>+</sup>) and hydride (H<sup>-</sup>) was considered in this study. The results in Chapter 2 also suggest that such a heterolytic H<sub>2</sub> cleavage can be promoted both by the Lewis acid-base sites of the support itself or by the metal-titania interface sites. Therefore, three alternative sites were considered for H<sub>2</sub> dissociation by Au/TiO<sub>2</sub> (Figure 5.6), namely (a) the Ti<sub>5c</sub>-O<sub>2c</sub> pair site of the TiO<sub>2</sub> support, as well as (b) the Au(3D)-O<sub>2c</sub> and (c) Au(2D)-O<sub>2c</sub> interface sites for the 3D and 2D supported Au cluster models, respectively. The DFT calculations show that the heterolytic H<sub>2</sub> dissociation at the Au/TiO<sub>2</sub> interface site is exothermic, while that reaction at the TiO<sub>2</sub> surface site is endothermic. The calculated activation energy of H-H bond cleavage at the Ti<sub>5c</sub>-O<sub>2c</sub> pair site ( $E_a = 0.46$  eV) is about one time higher than that over the Au-O<sub>2c</sub> pair sites ( $E_a = 0.29$ - $0.28$  eV). Therefore, our calculations show that the H<sub>2</sub> dissociation at the interfacial Au-O<sub>2c</sub> sites is both thermodynamically and kinetically more favorable than at the Ti<sub>5c</sub>-O<sub>2c</sub> pair site. Furthermore, we found that the geometry of the supported Au<sub>13</sub> clusters does not affect the activation and the reaction energy of H<sub>2</sub> dissociation. Both Au<sub>13</sub>-2D/TiO<sub>2</sub> and Au<sub>13</sub>-3D/TiO<sub>2</sub> show very similar catalytic activity for this step.

Compared with the results of heterolytic H<sub>2</sub> dissociation on Cd/TiO<sub>2(anatase)</sub> (Chapter 2), Au/TiO<sub>2(rutile)</sub> is more active for the dissociation of H<sub>2</sub> molecule. The activation energy of H-H bond cleavage at the Au/TiO<sub>2</sub> interface site is about 0.1 eV lower than that of the Cd/TiO<sub>2</sub> interface. In addition, this reaction at Au/TiO<sub>2</sub> interface sites is exothermic ( $\Delta E_{rxn}@Au_{13}$ -2D/TiO<sub>2</sub> = -0.13 eV,  $\Delta E_{rxn}@Au_{13}$ -3D/TiO<sub>2</sub> = -0.21 eV) while that reaction at Cd/TiO<sub>2</sub> interface sites is endothermic (0.15, 0.02, and 0.19 eV for sites B, C, and D, respectively). These results indicate that the catalytic activity of metal/oxides depends on the type and nature of both metal and oxide support.

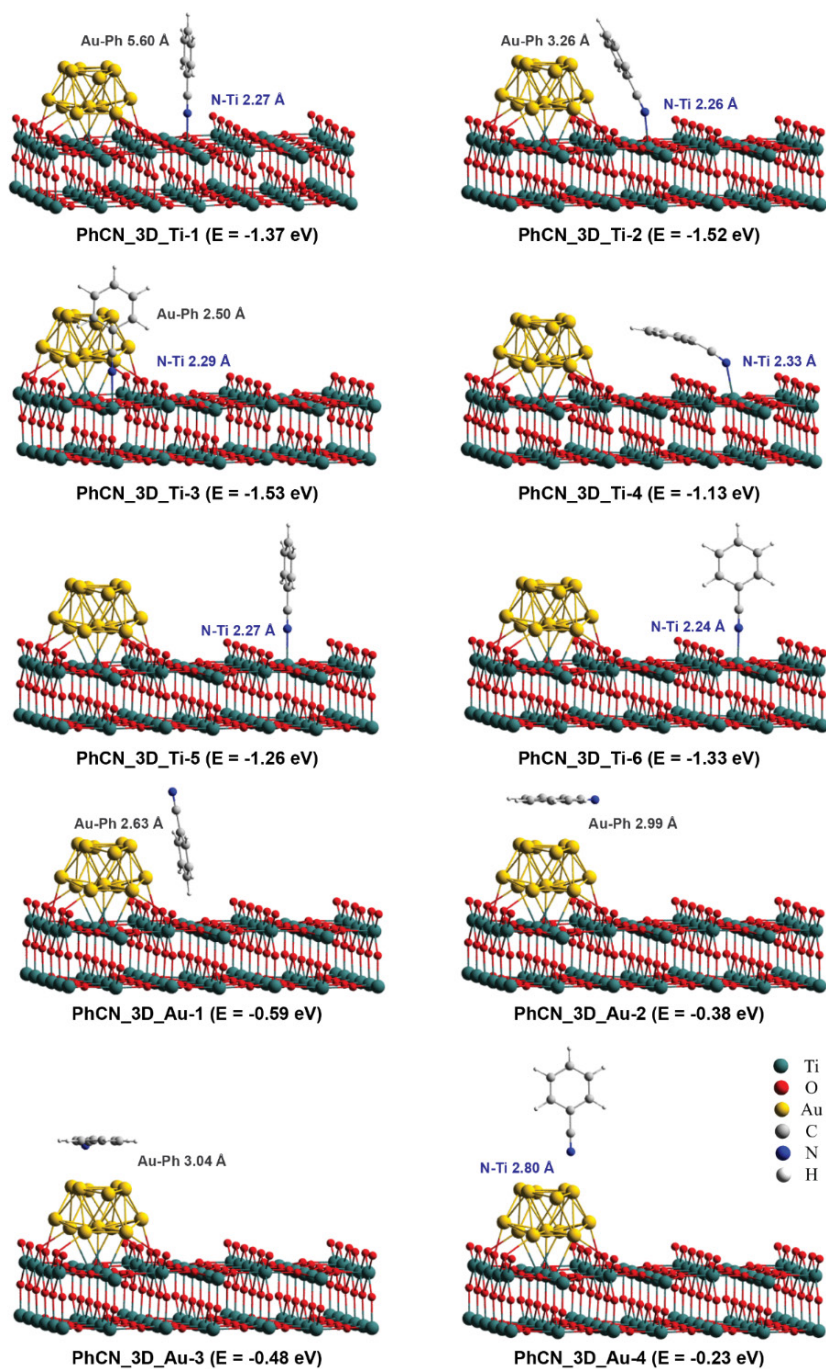
### 5.3.2 Adsorption of benzonitrile on Au<sub>13</sub>/TiO<sub>2</sub>

Next, the molecular adsorption of benzonitrile (PhCN) on the surface of Au<sub>13</sub>-3D/TiO<sub>2</sub> was analyzed to identify the starting configurations for the catalytic reaction. We considered ten different adsorption configurations resulting in the optimized structures shown in Figure 5.7. Our DFT calculations indicate that PhCN

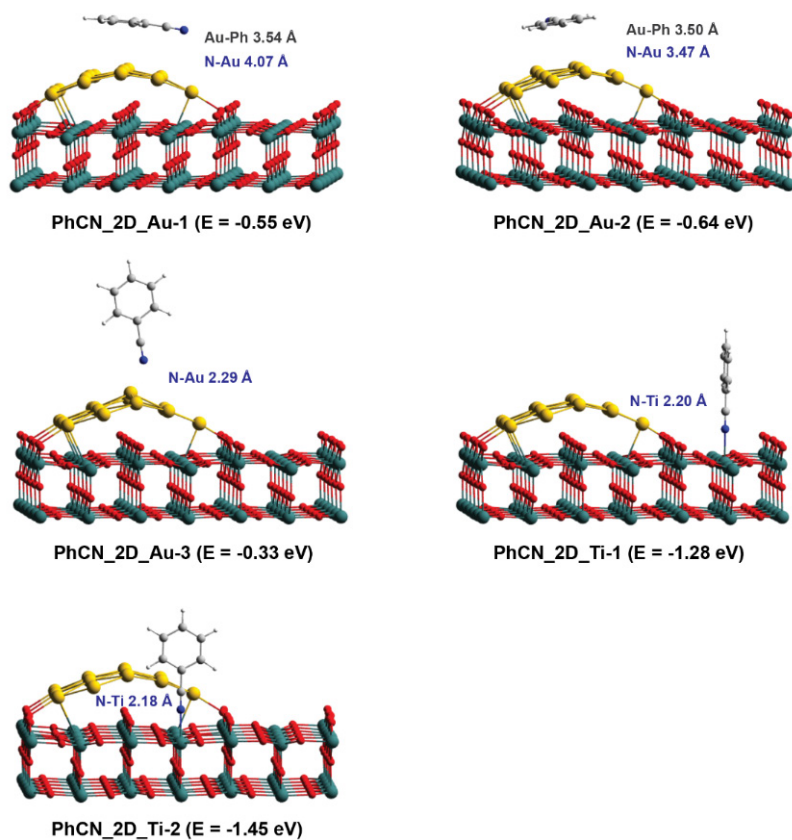
preferentially binds to the Lewis acidic  $Ti_{5c}$  surface site of the support in an end-on fashion rather than coordinating with the atoms of the supported Au cluster. The metallic surface stabilizes the  $TiO_2$ -adsorbed species through the interaction with the  $\pi$  system of the aromatic ring. The coordination of PhCN to  $Ti_{5c}$  surface sites shows adsorption energies in the range of -1.13 to -1.53 eV. Among adsorption modes, the complexes PhCN\_3D\_Ti-1, PhCN\_3D\_Ti-2, and PhCN\_3D\_Ti-3 formed near the supported  $Au_{13}$  cluster are found to be the three most stable structures (-1.37, -1.52 and -1.53 eV), which is ca. 0.2-0.4 eV more favorable than the adsorption to the distant  $Ti_{5c}$  sites. This energy difference is close to the energy values computed for PhCN physisorbed to Au sites (-0.23 – -0.59 eV). Note that the most stable configuration, in this case, is obtained for the configuration featuring PhCN physisorbed at the Au/ $TiO_2$  interface, but with the basic -CN moiety pointing opposite to the Lewis acidic Ti sites.

A similar analysis of PhCN adsorption to the  $Au_{13}$ -2D/ $TiO_2$  model has provided us with five distinct adsorption configurations summarized in Figure 5.8. In line with the discussion above, the most favorable adsorption mode in the current case is realized for the coordination of the CN group of PhCN in an end-on mode to the surface sites with the preferential binding to the Lewis acidic  $Ti_{5c}$  site (PhCN\_2D\_Ti-1 and PhCN\_2D\_Ti-2). The DFT computed adsorption energies for these modes are in the range of -1.28 to -1.45 eV. In line with the higher stability of the  $Au_{13}$ -2D/ $TiO_2$  structure compared to the  $Au_{13}$ -3D/ $TiO_2$ , a somewhat weaker PhCN adsorption is predicted for the former model. For other configurations, the parallel adsorption of PhCN to the gold surface of the supported 2D  $Au_{13}$  cluster is less favorable (PhCN\_2D\_Au-1 and PhCN\_2D\_Au-2) with the computed adsorption energies of -0.55 and -0.63 eV, respectively. The alternative end-on adsorption mode of PhCN to Au surface site (PhCN\_2D\_Au-3) gives rise to the least stable configuration with the adsorption energy of -0.33 eV.

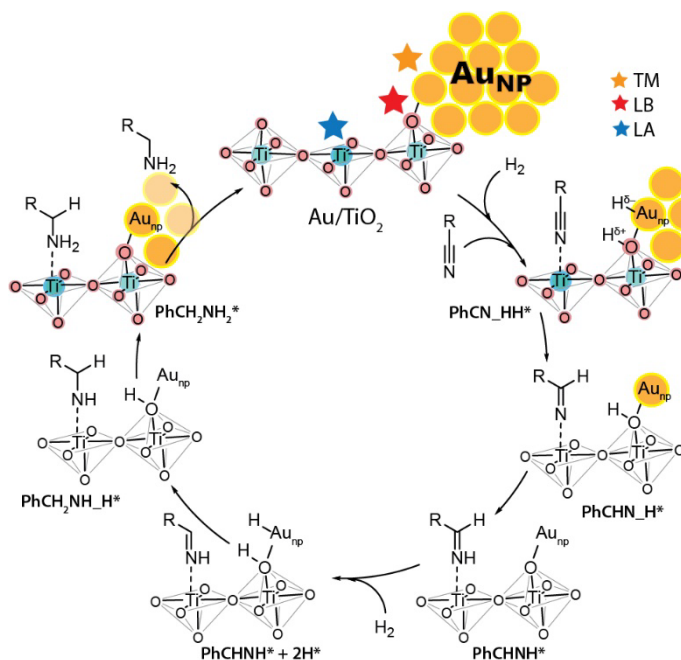
In summary, the DFT analysis of PhCN adsorption to  $Au_{13}$ -3D/ $TiO_2$  and  $Au_{13}$ -2D/ $TiO_2$  systems reveals that these species preferentially adsorb the PhCN substrate to the Lewis acidic  $Ti_{5c}$  site at the Au/ $TiO_2$  interface, which features the Au- $O_{2c}$  Lewis acid-base pairs necessary for the heterolytic  $H_2$  cleavage. We propose that such preferred coordination and polarization of the PhCN substrate near the  $H_2$  dissociation sites provide a favorable channel for further highly selective reduction of the polar CN group. To probe this hypothesis, we further investigated the catalytic reduction of PhCN, starting with the most stable adsorption configurations for both  $Au_{13}$ -3D/ $TiO_2$  and  $Au_{13}$ -2D/ $TiO_2$  structures.



**Figure 5.7** The optimized structures of benzonitrile (PhCN) adsorbed on different sites of  $\text{Au}_{13}\text{-3D}/\text{TiO}_2$



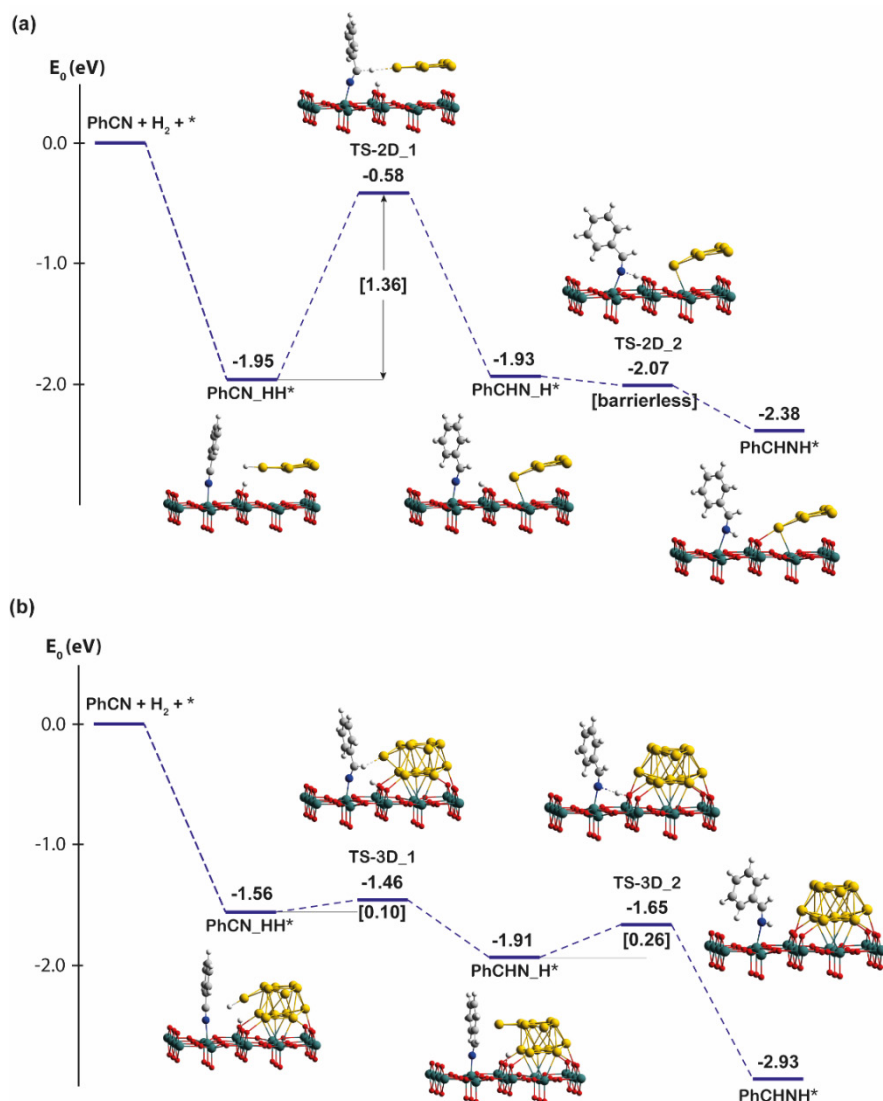
**Figure 5.8** The optimized structure of benzonitrile (PhCN) adsorption on different sites of  $Au_{13}$ - $2D/TiO_2$  catalyst



**Figure 5.9** The proposed mechanism of benzonitrile hydrogenation at the Au/TiO<sub>2</sub> interface

### 5.3.3 Benzonitrile hydrogenation on Au<sub>13</sub>/TiO<sub>2</sub>

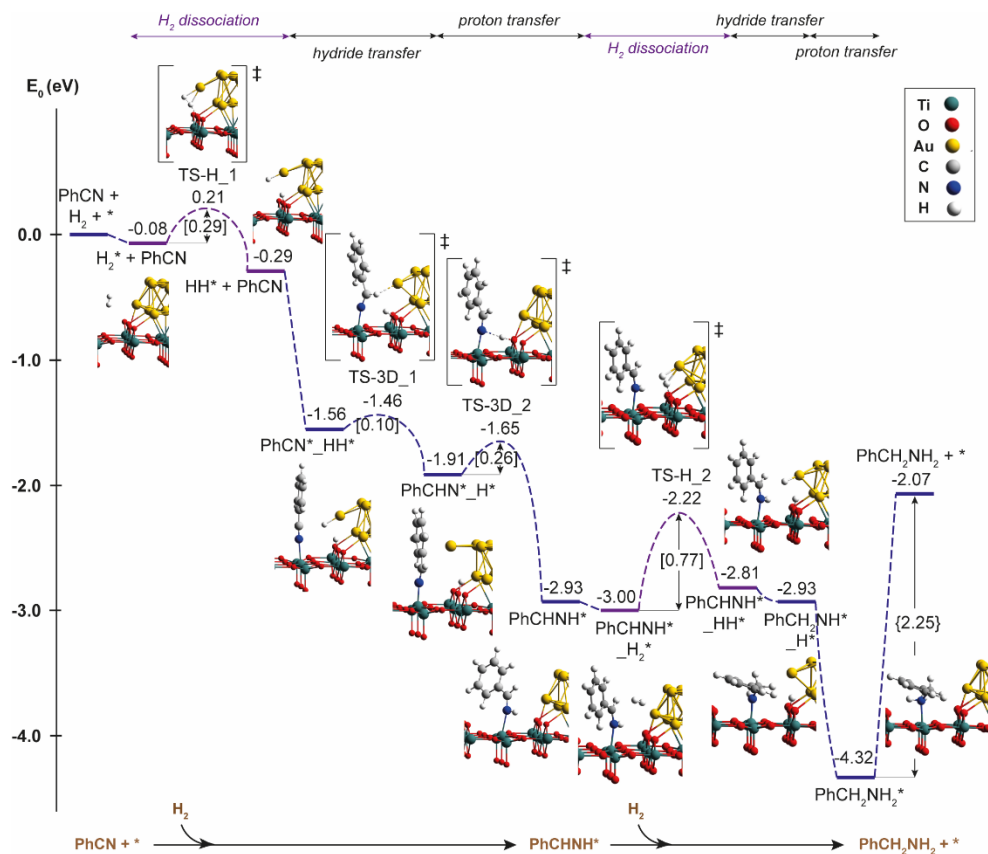
The reaction mechanism of benzonitrile (PhCN) hydrogenation to benzylamine (PhCH<sub>2</sub>NH<sub>2</sub>) is schematically presented in Figure 5.9. The synergy of the Lewis acid and base sites of the titania support and the metallic Au nanoparticle is proposed to play an important role in the heterolytic cleavage of H<sub>2</sub> and subsequent selective hydrogenation of the polar nitrile moiety. We propose that the hydrogenation of PhCN proceeds in four consecutive hydride and proton transfer reaction steps, forming PhCHN, PhCHNH, PhCH<sub>2</sub>NH, and the final product PhCH<sub>2</sub>NH<sub>2</sub>. Firstly, the conversion of PhCN to PhCHN via a hydride transfer is studied on two different catalytic models (Au<sub>13</sub>-3D/TiO<sub>2</sub> and Au<sub>13</sub>-2D/TiO<sub>2</sub>). Figure 5.10 shows that the first intermediate PhCHN is easily generated on the Au<sub>13</sub>-3D/TiO<sub>2</sub> with small activation energy (E<sub>a</sub> = 0.10 eV). In contrast, the same reaction on Au<sub>13</sub>-2D/TiO<sub>2</sub> requires much higher activation energy (E<sub>a</sub> = 1.36 eV). This result implies that the Au<sub>13</sub>-3D/TiO<sub>2</sub> is the preferred catalytic model for the hydrogenation of PhCN even though the supported Au<sub>13</sub> cluster with the 3D structure is less stable than the planar structure. Hence, the full catalytic cycle is further determined by using only the Au<sub>13</sub>-3D/TiO<sub>2</sub> catalytic structure.



**Figure 5.10** Reaction energy profiles of PhCN hydrogenation on (a)  $Au_{13}$ -2D/ $TiO_2$  and (b)  $Au_{13}$ -3D/ $TiO_2$  catalysts

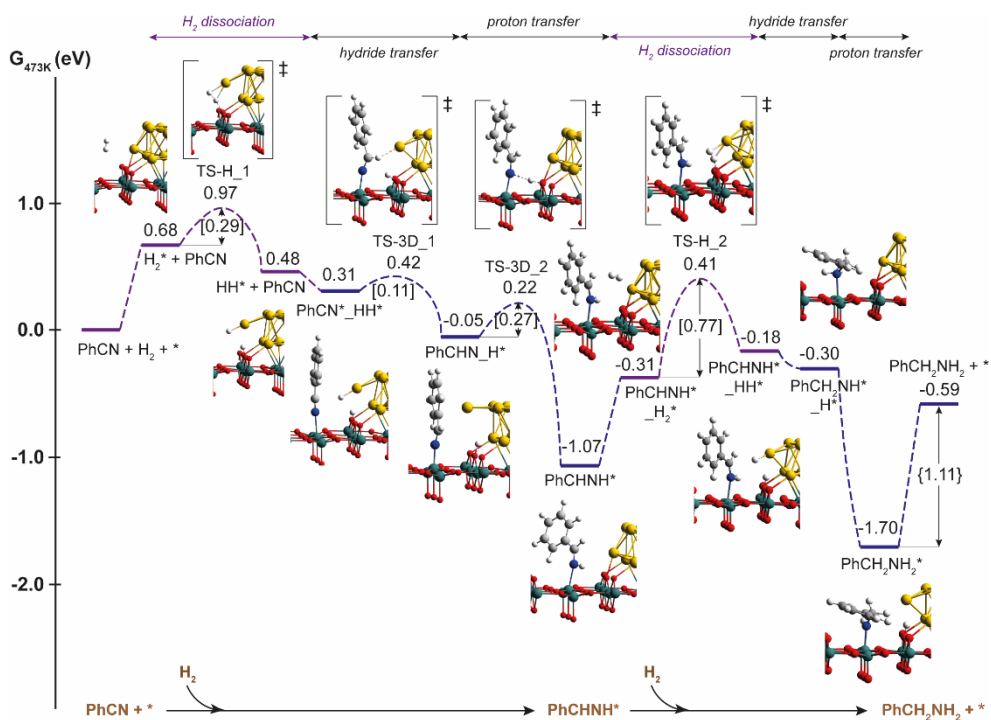
The complete reaction energy profile of PhCN hydrogenation to produce  $PhCH_2NH_2$  is illustrated in Figure 5.11. The end-on coordination of PhCN to the Lewis acidic  $Ti_{5c}$  site polarizes and activates the CN moiety facilitating thus the hydride transfer step. Indeed, once the  $H^{\delta+} \dots H^{\delta-}$  pair is generated at the interface site, the subsequent PhCN hydrogenation is energetically favorable and proceeds with small activation barriers of 0.10 eV and 0.26 eV for the hydride and proton

transfer steps, respectively. Further reduction of the benzylimine intermediate (PhCHNH) to benzylamine (PhCH<sub>2</sub>NH<sub>2</sub>) is barrierless. However, the desorption of the PhCH<sub>2</sub>NH<sub>2</sub> product and the regeneration of the Lewis acidic Ti site is quite endothermic by 2.25 eV. By accounting for the translational and rotational entropy gains due to the product desorption at 200 °C, we estimate the Gibbs free energy for this final step to be only 1.11 eV, as shown in Figure 5.12. These DFT results indicate that the synergetic action of the multifunctional active sites at the Au-TiO<sub>2</sub> interface is the key for selective nitrile hydrogenation.



**Figure 5.11** Reaction energy profile of the catalytic reduction of benzonitrile (PhCN) to benzylamine (PhCH<sub>2</sub>NH<sub>2</sub>) on the Au<sub>13</sub>-3D/TiO<sub>2</sub>





**Figure 5.12** Reaction Gibbs free energy profile for benzonitrile hydrogenation to benzylamine ( $\text{PhCN} + 2\text{H}_2 \rightarrow \text{PhCH}_2\text{NH}_2$ ) on the  $\text{Au}_{13}/\text{TiO}_2$  catalyst.

## 5.4 Conclusion

In summary, the catalytic activity of  $\text{Au}_{13}/\text{TiO}_2$  for the benzonitrile hydrogenation to benzylamine was investigated by using periodic DFT calculations. We found that the  $\text{Au}/\text{TiO}_2$  interface is the critical active site for the dissociation of  $\text{H}_2$ , while the benzonitrile tends to be adsorbed in the end-on configuration at the interfacial  $\text{Ti}_{5c}$  site via its CN moiety. The generated hydride and proton from the heterolytic cleavage of  $\text{H}_2$  are essential for reducing the polar CN moiety, facilitating the subsequent hydrogenation reaction. Furthermore, we found that the geometry of the  $\text{Au}_{13}$  cluster has a negligible effect on the activation energy of  $\text{H}_2$  dissociation but has a significant impact on the hydrogenation of benzonitrile. The DFT calculations provide detailed mechanisms, while the descriptions of the catalytic role of each functional component clarify the catalytic reactivity. This information is useful for guiding the experiment and rationalizing the catalyst design for selective nitriles hydrogenation.

## References

1. Nair, U.R., R. Sivabalan, G.M. Gore, M. Geetha, S.N. Asthana, and H. Singh, *Hexanitrohexaazaisowurtzitane (CL-20) and CL-20-based formulations (review)*. *Combust. Explos. Shock Waves*, 2005. **41**(2): p. 121-132.
2. Heuer, L., Benzylamine, in *Ullmann's Encyclopedia of Industrial Chemistry*. 2006.
3. Xungang, G., L. Guoqing, L. Shaosuo, L. Yinghui, L. Xuefeng, W. Gang, X. Song, and Z. Yunbing, *Method for synthesizing benzyl chloride*. *Patent CN109721466A*. 2019: China.
4. Anbarasan, P., T. Schareina, and M. Beller, *Recent developments and perspectives in palladium-catalyzed cyanation of aryl halides: synthesis of benzonitriles*. *Chem. Soc. Rev.*, 2011. **40**(10): p. 5049-5067.
5. Sundermeier, M., A. Zapf, S. Mutyala, W. Baumann, J. Sans, S. Weiss, and M. Beller, *Progress in the Palladium-Catalyzed Cyanation of Aryl Chlorides*. *Eur. J. Chem.*, 2003. **9**(8): p. 1828-1836.
6. Lv, J., Y. Shen, L. Peng, X. Guo, and W. Ding, *Exclusively selective oxidation of toluene to benzaldehyde on ceria nanocubes by molecular oxygen*. *Chem. Commun.*, 2010. **46**(32): p. 5909-5911.
7. Coeck, R., J. Meeprasert, G. Li, T. Altantzis, S. Bals, E.A. Pidko, and D.E. De Vos, *Gold and Silver-Catalyzed Reductive Amination of Aromatic Carboxylic Acids to Benzylic Amines*. *ACS Catal.*, 2021. **11**(13): p. 7672-7684.
8. Pugh, S., R. McKenna, I. Halloum, and D.R. Nielsen, *Engineering Escherichia coli for renewable benzyl alcohol production*. *Metab. Eng. Commun.*, 2015. **2**: p. 39-45.
9. Fujita, K.-i., S. Furukawa, N. Morishima, M. Shimizu, and R. Yamaguchi, *N-Alkylation of Aqueous Ammonia with Alcohols Leading to Primary Amines Catalyzed by Water-Soluble N-Heterocyclic Carbene Complexes of Iridium*. *ChemCatChem*, 2018. **10**(9): p. 1993-1997.
10. Gunanathan, C. and D. Milstein, *Selective Synthesis of Primary Amines Directly from Alcohols and Ammonia*. *Angew. Chem. Int. Ed.*, 2008. **47**(45): p. 8661-8664.
11. Imm, S., S. Bähn, M. Zhang, L. Neubert, H. Neumann, F. Klasovsky, J. Pfeffer, T. Haas, and M. Beller, *Improved Ruthenium-Catalyzed Amination of Alcohols with Ammonia: Synthesis of Diamines and Amino Esters*. *Angew. Chem. Int. Ed.*, 2011. **50**(33): p. 7599-7603.
12. Liu, Y., A. Afanasenko, S. Elangovan, Z. Sun, and K. Barta, *Primary Benzylamines by Efficient N-Alkylation of Benzyl Alcohols Using Commercial Ni Catalysts and Easy-to-Handle Ammonia Sources*. *ACS Sustain. Chem. Eng.*, 2019. **7**(13): p. 11267-11274.

13. Shimizu, K.-I., K. Kon, W. Onodera, H. Yamazaki, and J.N. Kondo, *Heterogeneous Ni Catalyst for Direct Synthesis of Primary Amines from Alcohols and Ammonia*. *ACS Catal.*, 2013. **3**(1): p. 112-117.
14. Shimizu, K.-I., S. Kanno, K. Kon, S.M.A. Hakim Siddiki, H. Tanaka, and Y. Sakata, *N-alkylation of ammonia and amines with alcohols catalyzed by Ni-loaded CaSiO<sub>3</sub>*. *Catal. Today*, 2014. **232**: p. 134-138.
15. Arceo, E., J.A. Ellman, and R.G. Bergman, *A Direct, Biomass-Based Synthesis of Benzoic Acid: Formic Acid-Mediated Deoxygenation of the Glucose-Derived Materials Quinic Acid and Shikimic Acid*. *ChemSusChem*, 2010. **3**(7): p. 811-813.
16. Pfennig, T., J.M. Carraher, A. Chemburkar, R.L. Johnson, A.T. Anderson, J.-P. Tessonnier, M. Neurock, and B.H. Shanks, *A new selective route towards benzoic acid and derivatives from biomass-derived coumalic acid*. *Green Chem.*, 2017. **19**(20): p. 4879-4888.
17. Coeck, R., S. Berden, and D.E. De Vos, *Sustainable hydrogenation of aliphatic acyclic primary amides to primary amines with recyclable heterogeneous ruthenium–tungsten catalysts*. *Green Chem.*, 2019. **21**(19): p. 5326-5335.
18. Coeck, R. and D.E. De Vos, *One-pot reductive amination of carboxylic acids: a sustainable method for primary amine synthesis*. *Green Chem.*, 2020. **22**(15): p. 5105-5114.
19. Kresse, G. and J. Furthmüller, *Efficiency of ab-initio total energy calculations for metals and semiconductors using a plane-wave basis set*. *Comput. Mater. Sci.*, 1996. **6**(1): p. 15-50.
20. Kresse, G. and J. Furthmüller, *Efficient iterative schemes for ab initio total-energy calculations using a plane-wave basis set*. *Phys. Rev. B*, 1996. **54**(16): p. 11169-11186.
21. Perdew, J.P., K. Burke, and M. Ernzerhof, *Generalized Gradient Approximation Made Simple*. *Phys. Rev. Lett.*, 1996. **77**(18): p. 3865-3868.
22. Grimme, S., S. Ehrlich, and L. Goerigk, *Effect of the damping function in dispersion corrected Density Functional Theory*. *J. Comput. Chem.*, 2011. **32**(7): p. 1456-1465.
23. Song, W., S. Ma, L. Wang, J. Liu, and Z. Zhao, *Theoretical Explanation of the Photogenerated Carrier Separation at the Surface Junction*. *ChemCatChem*, 2017. **9**(23): p. 4340-4344.
24. Hong, S. and T.S. Rahman, *Rationale for the Higher Reactivity of Interfacial Sites in Methanol Decomposition on Au<sub>13</sub>/TiO<sub>2</sub>(110)*. *J. Am. Chem. Soc.*, 2013. **135**(20): p. 7629-7635.
25. Boronat, M., P. Concepción, A. Corma, S. González, F. Illas, and P. Serna, *A Molecular Mechanism for the Chemoselective Hydrogenation of Substituted Nitroaromatics with Nanoparticles of Gold on TiO<sub>2</sub> Catalysts: A*

- Cooperative Effect between Gold and the Support. J. Am. Chem. Soc.*, 2007. **129**(51): p. 16230-16237.
26. Ding, R.-L., J. Jia, and H.-S. Wu, *The growth pattern of Au<sub>n</sub> (n=1–20) clusters absorbed on rutile TiO<sub>2</sub> (110) surfaces. Appl. Surf. Sci.*, 2015. **359**: p. 729-735.
  27. Boronat, M., F. Illas, and A. Corma, *Active Sites for H<sub>2</sub> Adsorption and Activation in Au/TiO<sub>2</sub> and the Role of the Support. J. Phys. Chem. A*, 2009. **113**(16): p. 3750-3757.
  28. Wan, W., X. Nie, M.J. Janik, C. Song, and X. Guo, *Adsorption, Dissociation, and Spillover of Hydrogen over Au/TiO<sub>2</sub> Catalysts: The Effects of Cluster Size and Metal–Support Interaction from DFT. J. Phys. Chem. C*, 2018. **122**(31): p. 17895-17916.
  29. Liu, L., Z. Liu, H. Sun, and X. Zhao, *Morphological effects of Au<sub>13</sub> clusters on the adsorption of CO<sub>2</sub> over anatase TiO<sub>2</sub>(101). Appl. Surf. Sci.*, 2017. **399**: p. 469-479.
  30. Hu, G., Z. Wu, and D.-E. Jiang, *First Principles Insight into H<sub>2</sub> Activation and Hydride Species on TiO<sub>2</sub> Surfaces. J. Phys. Chem. C*, 2018. **122**(35): p. 20323-20328.
  31. Yang, B., X.-M. Cao, X.-Q. Gong, and P. Hu, *A Density Functional Theory study of hydrogen dissociation and diffusion at the perimeter sites of Au/TiO<sub>2</sub>. Phys. Chem. Chem. Phys.*, 2012. **14**(11): p. 3741-3745.
  32. Sun, K., M. Kohyama, S. Tanaka, and S. Takeda, *A Study on the Mechanism for H<sub>2</sub> Dissociation on Au/TiO<sub>2</sub> Catalysts. J. Phys. Chem. C*, 2014. **118**(3): p. 1611-1617.

## Summary

Computational chemistry provides powerful research tools for catalysis. It potentially allows us to study the structures of the catalytic sites and reaction mechanisms, which are difficult to observe only by experiment. This is particularly true for supported heterogeneous catalysts, of which reactivity and catalytic behavior are directly related to the presence of various functional groups and reactive ensembles on their surfaces. Such surface heterogeneities give rise to the formation of multifunctional reactive ensembles ready to convert substrate molecules to the desired products efficiently. At the same time, the presence of various reactive centers on the surface may contribute to undesirable conversion paths. Understanding the role of the multifunctional reaction environments established on the complex surfaces of supported heterogeneous catalysts is key to formulating design rules for achieving control over their activity and selectivity.

However, the complexity of surface species and the associated chemistry make it particularly challenging to get insights into the nature of the active site and the reaction pathways during the catalytic processes. In this context, computational chemistry provides a unique opportunity to unravel the detailed mechanistic picture of the catalytic phenomenon and understand the specific role and potential synergy between the different components of complex heterogeneous catalyst systems. In this thesis, I applied density functional theory (DFT) calculations to study the role of the multifunctionality of TiO<sub>2</sub>-based catalysts for the valorization of CO<sub>2</sub> and biomass. The main focus lies on the reaction mechanisms, the role of each catalytic component, and how they organically work together to facilitate the specific reaction steps.

In Chapter 2, periodic DFT calculations combined with microkinetic modeling (MKM) were performed to investigate the mechanisms of CO<sub>2</sub> hydrogenation to CH<sub>3</sub>OH on Cd<sub>4</sub>/TiO<sub>2</sub> catalyst. This catalyst, which was developed by our collaborators, displayed highly selective towards CH<sub>3</sub>OH. Herein, we found that the multifunctionality at the Cd-TiO<sub>2</sub> interface, including the Lewis acid of metal and the Lewis base of surface oxygen, is essential for the outstanding performance of Cd/TiO<sub>2</sub> catalyst. H<sub>2</sub> and CO<sub>2</sub> molecules prefer to be activated at the Cd-TiO<sub>2</sub> interface rather than at the TiO<sub>2</sub> surface or Cd cluster. The detailed mechanistic study indicates that the formate pathway dominates over the RWGS pathway for the production of CH<sub>3</sub>OH. In the RWGS pathway, the effect of the promotor, which is H<sub>2</sub>O, was studied. We found that H<sub>2</sub>O is needed to proceed the reaction via the

RWGS pathway. The MKM analysis pointed to the formation of the formaldehyde intermediate in the formate pathway as the rate-limiting reaction step. Surface formate species are identified as the resting state of the whole reaction, which is in line with the experimental observations. The strong binding of such species at the surface is responsible for the high activation energy in the rate-limiting reaction step. Thus, these results suggest that the interaction between support and the metal nanocluster should be fine-tuned to further improve the catalyst performance.

Besides the metal-support interface as a reaction center to activate reactant, the additives of alkali carbonates dispersed on the surface of  $\text{TiO}_2$  can also play as promoters to facilitate  $\text{CO}_2$  conversion and catalyst regeneration. In Chapter 3, we studied the catalytic activity of  $\text{K}_2\text{CO}_3/\text{TiO}_2$ , which was observed experimentally as an efficient catalyst for the esterification of benzene with  $\text{CO}_2$  and  $\text{CH}_3\text{OH}$ . The bare defective  $\text{TiO}_2$  was also investigated because it showed high efficiency but was deactivated rapidly. Here, the effect of the inhibition from the high thermodynamic stability of intermediates that was observed in the previous chapter was clarified. In these catalytic systems, the introduction of oxygen vacancy on  $\text{TiO}_2$  surface generates  $\text{Ti}^{3+}$  as a new active site for the catalyst. The periodic DFT calculations revealed that the catalytic reactivity originates from  $\text{Ti}^{3+}/\text{K}^+$  and  $\text{Ti}^{3+}/\text{Ti}^{3+}$  pair sites of  $\text{K}_2\text{CO}_3/\text{TiO}_2$  and bare defective  $\text{TiO}_2$ , respectively. The reaction mechanism of benzene esterification with  $\text{CO}_2$  and  $\text{CH}_3\text{OH}$  is composed of two main reactions. The first one is the carboxylation of benzene with  $\text{CO}_2$ , while another is the methylation with  $\text{CH}_3\text{OH}$  to produce methyl benzoate. We found that both catalysts can catalyze the reaction with similar activation energies. However, the too-strong binding of products on the bare defective  $\text{TiO}_2$  impedes the desorption and regeneration of the active site for the next catalytic cycle. In the case of  $\text{K}_2\text{CO}_3/\text{TiO}_2$ , the  $\text{K}_2\text{CO}_3$  species, which partially occupy oxygen vacancies, affect the lowering of the product's adsorption strength and thus prevent catalyst poisoning. From this study, we expect that the unique multifunction of  $\text{K}_2\text{CO}_3/\text{TiO}_2$  could be potential for the direct C-C coupling reaction of  $\text{CO}_2$  with other less reactive but more abundant hydrocarbons such as  $\text{CH}_4$ .

Therefore, to check our hypothesis, in Chapter 4, we extended the study of Chapter 3 to investigate the catalytic activity of  $\text{K}_2\text{CO}_3/\text{TiO}_2$  for the same esterification reaction but using  $\text{CH}_4$  instead of benzene as the substrate. One can expect that this catalyst could be as active in the conversion of  $\text{CH}_4$  as for benzene because of the similarity in their C-H bond energies ( $\Delta H_{298}(\text{CH}_4) = 105$  kcal/mol,  $\Delta H_{298}(\text{C}_6\text{H}_6) = 113$  kcal/mol). Direct activation and conversion of  $\text{CH}_4$  to chemicals

is extremely challenging because of the high binding energy, high symmetry, and low polarity of the C-H bonds. Moreover, the product is usually more reactive than CH<sub>4</sub>, making it difficult to control the selectivity and avoid over activation of the desired products. Thus, the conversion of CH<sub>4</sub> has been a challenge in chemical synthesis similar to CO<sub>2</sub>. This study highlights the difference in reactivity between benzene and CH<sub>4</sub>. The side reaction of CO production was also investigated to examine the product selectivity. The calculations revealed that, indeed, K<sub>2</sub>CO<sub>3</sub>/TiO<sub>2</sub> could potentially catalyze the esterification of CH<sub>4</sub> with CO<sub>2</sub> and CH<sub>3</sub>OH. The activation barriers of all elementary steps are similar to the esterification of benzene, and the manners of reactants activation at the interface of K<sub>2</sub>CO<sub>3</sub>/TiO<sub>2</sub> are also comparable between CH<sub>4</sub> and benzene esterification.

However, in the initial step, the C-H bond carboxylation of CH<sub>4</sub> with CO<sub>2</sub> proceeds in one step, while that of benzene occurs in two-step reactions with the metastable C<sub>6</sub>H<sub>6</sub>COO\* as an intermediate due to the aromaticity of benzene. The barrier of this step is 0.44 eV lower than the decomposition of CO<sub>2</sub> to CO. Thus, the selectivity towards methyl benzoate is higher than CO formation, which is consistent with the experimental observations. In contrast, in the case of CH<sub>4</sub>, a low selectivity of methyl acetate was predicted because the activation energy of C-H bond carboxylation with CO<sub>2</sub> in CH<sub>4</sub> is 0.06 eV higher than that of CO formation. This result implies that the formation of CO can compete with the CH<sub>4</sub> carboxylation, which is not the case in the carboxylation of benzene. Thus, further modification of this catalyst is required for selective C-H bond carboxylation of methane. We propose that enhancing the Lewis basic strength of surface oxygen atoms by replacing the neighboring Ti<sup>4+</sup> with a lower-valence cation might be one of the strategies to strengthen the interaction with CH<sub>4</sub> and facilitate the C-H bond dissociation without accelerating the decomposition of CO<sub>2</sub>.

Chapter 5 presents the mechanistic study of benzonitrile hydrogenation on Au<sub>13</sub>/TiO<sub>2</sub>. This catalyst, which was developed by our experimental collaborators, exhibited high reactivity and selectivity for the conversion of benzonitrile to benzylamine. In our work, we applied the knowledge about multifunctional TiO<sub>2</sub>-supported catalysts to study the conversion of more complicated substrates. In this catalytic system, the reactivity is due to the synergistic effect of Lewis acid and Lewis base at the Au/TiO<sub>2</sub> interface. We also examined the geometrical effects of the supported Au<sub>13</sub> cluster. The calculations reveal that the geometry of the Au<sub>13</sub> cluster has a minor effect on the activation energy of H<sub>2</sub> dissociation but a significant impact on the hydrogenation of benzonitrile.

We have shown that multiple functionalities in heterogeneous catalysts are responsible for both positive aspects, such as reactant activation and intermediate stabilization; and negative aspects, such as catalyst deactivation, low product selectivity, and undesired products. Therefore, understanding the role of each function on catalysts can help us facilitate those desired aspects and prevent those undesired phenomena by controlling the very complex chemical transformations along low-energy reaction pathways. Designing the multifunctionality and understanding how it helps the desirable conversions is a key to rational catalyst design. The challenges are to learn how to construct these multifunctional ensembles, ensure that they do not degrade during performing, and maintain their performances over a prolonged period of time.

So far, most DFT studies have been performed to provide mechanistic details of catalytic processes under ultra-high vacuum and 0 K conditions. However, over the past decades, computational catalysis has evolved toward studying catalytic processes under working conditions. In our works, combining DFT with MKM allows us to convert microscopic reaction mechanism data into experimentally measurable parameters such as key reaction intermediates and rate-limiting steps. This is a practical way to bridge the gap between static DFT modeling and realistic reaction under catalyst working conditions. We prospect that global optimization methods and *operando* methodologies such as *ab initio* thermodynamics and molecular dynamics would offer more options to further narrow the gap between modeling and experiment by including reaction conditions in the simulation.



# Samenvatting

Computationale chemie levert krachtige onderzoekshulpmiddelen voor katalyse. Dankzij computationale chemie kunnen we de structuren bestuderen van de katalytische centra en reactiemechanismen, die met alleen experimenten moeilijk waar te nemen zijn. Dit geldt met name voor gedragen heterogene katalysatoren, waarvan de reactiviteit en het katalytisch gedrag direct verband houden met de aanwezigheid van diverse functionele groepen en reactieve ensembles op het oppervlak ervan. Zulke oppervlakteheterogeniteiten geven aanleiding tot de vorming van multifunctionele reactieve ensembles die in staat zijn substraatmoleculen efficiënt om te zetten in de gewenste producten. Tegelijkertijd kan de aanwezigheid van diverse reactieve centra op het oppervlak bijdragen aan ongewenste omzettingroutes. Inzicht in de rol van de multifunctionele reactieomgevingen aan de complexe oppervlakken van gedragen heterogene katalysatoren is essentieel voor het formuleren van ontwerpregels om controle te krijgen over de activiteit en selectiviteit ervan.

De complexiteit van oppervlakte-entiteiten en de bijbehorende chemie maakt het echter bijzonder uitdagend om inzicht te krijgen in de aard van het actieve centrum en de reactieroutes tijdens de katalytische processen. In dit verband levert computationale chemie een unieke mogelijkheid om het gedetailleerde mechanistische beeld van het katalytische fenomeen te ontrafelen en de specifieke rol en potentiële synergie tussen de verschillende componenten van complexe heterogene katalysatorsystemen te begrijpen. In dit proefschrift gebruikte ik berekeningen volgens de dichtheidsfunctietheorie (DFT) om de rol te bestuderen van de multifunctionaliteit van katalysatoren op basis van  $\text{TiO}_2$  voor de valorisatie van  $\text{CO}_2$  en biomassa. De focus ligt vooral op de reactiemechanismen, de rol van elke katalytische component en hoe die organisch samenwerken om de specifieke reactiestappen mogelijk te maken.

In hoofdstuk 2 werden periodieke DFT-berekeningen in combinatie met microkinetische modellering (MKM) uitgevoerd om de mechanismen van  $\text{CO}_2$ -hydrogenering tot  $\text{CH}_3\text{OH}$  op  $\text{Cd}_4/\text{TiO}_2$ -katalysator te onderzoeken. Deze katalysator, die door onze samenwerkingspartners werd ontwikkeld, vertoonde hoge selectiviteit voor  $\text{CH}_3\text{OH}$ . Hierin vonden we dat de multifunctionaliteit aan het  $\text{Cd-TiO}_2$ -grensvlak, met inbegrip van het Lewis-zuur van metaal en de Lewis-base van oppervlaktezuurstof, essentieel is voor de uitstekende prestaties van  $\text{Cd/TiO}_2$ -katalysator.  $\text{H}_2$ - en  $\text{CO}_2$ -moleculen worden bij voorkeur geactiveerd aan het  $\text{Cd}$ -

TiO<sub>2</sub>-grensvlak in plaats van aan het TiO<sub>2</sub>-oppervlak of Cd-cluster. De gedetailleerde mechanistische studie geeft aan dat de formiaatroutte dominant is ten opzichte van de RWGS-route voor de productie van CH<sub>3</sub>OH. In de RWGS-route werd het effect van de promotor, die H<sub>2</sub>O is, bestudeerd. We hebben gevonden dat H<sub>2</sub>O nodig is om de reactie via de RWGS-route te laten verlopen. De MKM-analyse wees op de vorming van het formaldehyde-tussenproduct in de formiaatroutte als de snelheidsbepalende reactiestap. Formiaat-entiteiten aan het oppervlak zijn vastgesteld als de rusttoestand van de hele reactie, wat klopt met de experimentele waarnemingen. De sterke binding van zulke entiteiten aan het oppervlak zorgt voor de hoge activeringsenergie in de snelheidsbepalende reactiestap. Deze resultaten suggereren dus dat de interactie tussen drager en het metaalnanocluster nauwkeurig ingesteld zou moeten worden om de prestaties van de katalysator verder te verbeteren.

Naast het metaal-drager-grensvlak als reactiecentrum om reactant te activeren, kunnen de alkalicarbonaat-additieven die op het oppervlak van TiO<sub>2</sub> gedispergeerd zijn, ook als promotor fungeren om de omzetting van CO<sub>2</sub> en de regeneratie van katalysator te vergemakkelijken. In hoofdstuk 3 onderzochten we de katalytische activiteit van K<sub>2</sub>CO<sub>3</sub>/TiO<sub>2</sub>, waarvan experimenteel werd vastgesteld dat het een efficiënte katalysator voor de verestering van benzeen met CO<sub>2</sub> en CH<sub>3</sub>OH is. Het kale defectieve TiO<sub>2</sub> werd ook onderzocht omdat het hoge efficiëntie vertoonde, maar snel werd gedeactiveerd. Hier werd het in het vorige hoofdstuk waargenomen effect van de remming door de hoge thermodynamische stabiliteit van tussenproducten verhelderd. In deze katalytische systemen wordt door het inbrengen van zuurstofvacature op het TiO<sub>2</sub>-oppervlak Ti<sup>3+</sup> gegenereerd als een nieuw actief centrum voor de katalysator. De periodieke DFT-berekeningen lieten zien dat de katalytische reactiviteit voortkomt uit respectievelijk Ti<sup>3+</sup>/K<sup>+</sup> en Ti<sup>3+</sup>/Ti<sup>3+</sup>-paarcentra van K<sub>2</sub>CO<sub>3</sub>/TiO<sub>2</sub> en kaal defectief TiO<sub>2</sub>. Het reactiemechanisme van verestering van benzeen met CO<sub>2</sub> en CH<sub>3</sub>OH bestaat uit twee hoofdreacties. De eerste is de carboxylering van benzeen met CO<sub>2</sub> en de andere is de methylering met CH<sub>3</sub>OH om methylbenzoaat te produceren. We hebben gevonden dat beide katalysatoren de reactie met vergelijkbare activeringsenergieën kunnen katalyseren. Echter, de te sterke binding van producten aan het kale defectieve TiO<sub>2</sub> verhindert de desorptie en regeneratie van het actieve centrum voor de volgende katalytische cyclus. In het geval van K<sub>2</sub>CO<sub>3</sub>/TiO<sub>2</sub> zorgen de K<sub>2</sub>CO<sub>3</sub>-entiteiten, die de zuurstofvacatures gedeeltelijk bezetten, voor verlaging van de adsorptiesterkte van het product en wordt daarmee vergiftiging van de katalysator voorkomen. Op basis van dit onderzoek verwachten we dat de unieke

multifunctionaliteit van  $K_2CO_3/TiO_2$  potentie kan hebben voor C-C-koppelingsreactie van  $CO_2$  met minder reactieve, maar meer algemeen voorkomende koolwaterstoffen zoals  $CH_4$ .

Om onze hypothese te controleren, breidden we in hoofdstuk 4 daarom het onderzoek van hoofdstuk 3 verder uit om de katalytische activiteit van  $K_2CO_3/TiO_2$  voor dezelfde veresteringsreactie te onderzoeken, maar dan met gebruik van  $CH_4$  in plaats van benzeen als het substraat. Het is te verwachten dat deze katalysator even actief zou kunnen zijn bij de omzetting van  $CH_4$  als voor benzeen, vanwege de vergelijkbare C-H-bindingsenergieën ervan ( $\Delta H_{298}(CH_4) = 105$  kcal/mol,  $\Delta H_{298}(C_6H_6) = 113$  kcal/mol). Directe activering en omzetting van  $CH_4$  naar chemische stoffen is extreem uitdagend vanwege de hoge bindingsenergie, hoge symmetrie en lage polariteit van de C-H-bindingen. Bovendien is het product doorgaans reactiever dan  $CH_4$ , waardoor het moeilijk is om de selectiviteit onder controle te krijgen en overmatige activering van de gewenste producten te vermijden. Daarom is de omzetting van  $CH_4$  in de chemische synthese een uitdaging, net als met  $CO_2$ . Dit onderzoek belicht het verschil in reactiviteit tussen benzeen en  $CH_4$ . De nevenreactie van CO-productie werd ook bestudeerd om de productselectiviteit te onderzoeken. Uit de berekeningen bleek dat  $K_2CO_3/TiO_2$  de verestering van  $CH_4$  met  $CO_2$  en  $CH_3OH$  inderdaad zou kunnen katalyseren. De activeringsbarrières van alle elementaire stappen zijn vergelijkbaar met de verestering van benzeen, en de manieren waarop reactanten aan het grensvlak van  $K_2CO_3/TiO_2$  geactiveerd worden, zijn ook vergelijkbaar tussen de verestering van  $CH_4$  en die van benzeen.

Echter, in de eerste stap verloopt de carboxylering van de C-H-binding van  $CH_4$  met  $CO_2$  in één stap, terwijl die van benzeen in tweestapsreacties plaatsvindt met het metastabiele  $C_6H_6COO^*$  als tussenproduct als gevolg van de aromaticiteit van benzeen. De barrière van deze stap is 0,44 eV lager dan de ontleding van  $CO_2$  tot CO. Daarom is de selectiviteit voor methylbenzoaat hoger dan de vorming van CO, wat klopt met de experimentele waarnemingen. Daarentegen werd in het geval van  $CH_4$  een lage selectiviteit voor methylacetaat voorspeld, omdat de activeringsenergie van carboxylering van de C-H-binding met  $CO_2$  in  $CH_4$  0,06 eV hoger is dan die van CO-vorming. Dit resultaat impliceert dat de vorming van CO kan concurreren met de carboxylering van  $CH_4$ , wat niet het geval is bij de carboxylering van benzeen. Daarom is verdere modificatie van deze katalysator nodig voor de selectieve carboxylering van de C-H-binding van methaan. We stellen voor dat verhoging van de Lewis-basesterkte van oppervlaktezuurstofatomen door het aangrenzende  $Ti4+$  te vervangen door een kation met een lagere valentie een van de strategieën zou kunnen zijn om de interactie met  $CH_4$  te versterken en de

dissociatie van de C-H-binding te vergemakkelijken zonder de ontleding van CO<sub>2</sub> te versnellen.

Hoofdstuk 5 beschrijft de mechanistische studie van de hydrogenering van benzonitril op Au<sub>13</sub>/TiO<sub>2</sub>. Deze katalysator, die door onze experimentele samenwerkingspartners werd ontwikkeld, vertoonde hoge reactiviteit en selectiviteit voor de omzetting van benzonitril naar benzylamine. In ons werk pasten we de kennis over multifunctionele, op TiO<sub>2</sub> gedragen katalysatoren toe om de omzetting van complexere substraten te onderzoeken. In dit katalytische systeem is de reactiviteit het gevolg van het synergistische effect van Lewis-zuur en Lewis-base aan het Au/TiO<sub>2</sub>-grensvlak. We onderzochten ook de geometrische effecten van het gedragen Au<sub>13</sub>-cluster. Uit de berekeningen blijkt dat de geometrie van het Au<sub>13</sub>-cluster een klein effect heeft op de activeringsenergie van H<sub>2</sub>-dissociatie, maar een significante impact op de hydrogenering van benzonitril.

We hebben aangetoond dat meerdere functionaliteiten in heterogene katalysatoren verantwoordelijk zijn voor zowel positieve aspecten, zoals activering van reactanten en stabilisatie van tussenproducten, als negatieve aspecten, zoals deactivering van katalysator, lage productselectiviteit en ongewenste producten. Daarom kan inzicht in de rol van elke functie op katalysatoren ons helpen die gewenste aspecten te verbeteren en die ongewenste verschijnselen te voorkomen door de zeer complexe chemische transformaties via laagenergetische reactieroutes te controleren. Het ontwerpen van de multifunctionaliteit en het inzicht in hoe die gunstig is voor de wenselijke omzettingen is een sleutel tot rationeel katalysatorontwerp. De uitdagingen liggen in het leren hoe deze multifunctionele ensembles op te bouwen, te zorgen dat ze niet afbreken tijdens het gebruik en hun prestaties gedurende langere tijd behouden.

Tot dusver zijn de meeste DFT-studies gedaan om mechanistische details van katalytische processen onder omstandigheden van ultrahoog vacuüm en 0 K te leveren. In de afgelopen decennia is computationele katalyse echter geëvolueerd naar het bestuderen van katalytische processen onder werkomstandigheden. In ons werk heeft de combinatie van DFT en MKM ons in staat gesteld gegevens over microscopische reactiemechanismen om te zetten in experimenteel meetbare parameters, zoals belangrijke reactietussenproducten en snelheidsbepalende stappen. Dit is een praktische manier om de kloof te dichten tussen statische DFT-modellering en realistische reacties onder werkomstandigheden van katalysatoren. We verwachten dat algehele optimaliseringsmethoden en *operando*-methoden zoals ab-initio-thermodynamica en moleculaire dynamica

meer mogelijkheden zouden bieden om de kloof tussen modellering en experimenten verder te dichten door reactieomstandigheden in de simulatie op te nemen.



# Acknowledgements

This Thesis would have been impossible without the support of many people. My first appreciation goes to my supervisor, Evgeny Pidko, for his supervision, guidance, and support. Sincere gratitude is extended to his patience and encouragement when I was feeling unproductive and unmotivated. I would also like to thank my daily supervisor, Guanna Li, for sharing her knowledge and experience, teaching me many computational techniques, and giving me excellent advice during my Ph.D. journey.

I would like to offer my special thanks to my colleagues for their efforts and contributions to our research. I am thankful to Chong, who greatly helped me in my initial Ph.D. stage. Also, I would like to thank Dapeng, who taught me microkinetic modeling and troubleshooting my python scripts.

I thank all the members of the ISE group for their insightful comments and suggestions in the group meeting. I also thank Annika, Ali, Chong, Elena, and Dapeng for creating a good research atmosphere in the office. I appreciate all the kind people I met in TU Delft and thank them for their help and support.

I acknowledge the National Nanotechnology Center of Thailand and the Royal Thai Government Scholarship for giving me a chance to pursue a doctoral degree. I thank the Thai student community for their help while living in the Netherlands. Also, I thank my friends for their encouragement. Finally, I am grateful to my parents for their unconditional love and support.





## Curriculum Vitae

Jittima Meeprasert was born in Bangkok, Thailand, on the 27<sup>th</sup> of September 1983. In 2005, she graduated from Kasetsart University with a Bachelor's degree in General Science and continued with her Master's degree with a specialization in Physical Chemistry. In 2009, she worked at the National Nanotechnology Center (NANOTEC), a government organization under the National Science and Technology Development Agency, Thailand. In 2017, she received the Royal Thai Government Scholarship and moved to the Netherlands to pursue a Ph.D. research in the Inorganic Systems Engineering group at the Delft University of Technology, under the supervision of prof. dr. Evgeny Pidko. After finishing her Ph.D., she returns to Thailand and continues working as a researcher at the NANOTEC. The results of research in her Ph.D. period are described in this book.



# List of Publications

## Publications within the scope of this thesis

R. Coeck, **J. Meeprasert**, G. Li, T. Altantzis, S. Bals, E. A. Pidko, and D. E. De Vos, *Gold and Silver-Catalyzed Reductive Amination of Aromatic Carboxylic Acids to Benzylic Amines*. *ACS Catal.*, 2021, **11**(13), 7672-7684.

**J. Meeprasert**, G. Li, and E. A. Pidko, *Mechanistic investigation of benzene esterification by  $K_2CO_3/TiO_2$ : the catalytic role of the multifunctional interface*. *Chem. Commun.*, 2021, **57**, 7890-7893.

J. Wang, **J. Meeprasert**, Z. Han, H. Wang, Z. Feng, C. Tang, F. Sha, S. Tang, G. Li, E. A. Pidko, and C. Li, *Highly dispersed Cd cluster supported on  $TiO_2$  as an efficient catalyst for  $CO_2$  hydrogenation to methanol*. *Chinese J. Catal.*, 2022, **43**(3), 761-770.

**J. Meeprasert**, G. Li, J. Wang, C. Li, and E. A. Pidko,  *$CO_2$  Hydrogenation to Methanol over  $Cd_4/TiO_2$  Catalyst: Insight into Multifunctional Interface*. *ChemCatChem*, 2022, **14**, e202101646.

**J. Meeprasert**, G. Li, and E. A. Pidko, *The direct C-H carboxylation challenge: on the difference in the interaction mechanisms of  $CO_2$  with  $CH_4$  and  $C_6H_6$  on  $K_2CO_3/TiO_2$  catalyst*. *To be submitted*.

## Publications outside the scope of this thesis

L. Grajciar, C. J. Heard, A. A. Bondarenko, M. V. Polynski, **J. Meeprasert**, E. A. Pidko, and P. Nachtigall, *Towards operando computational modeling in heterogeneous catalysis*. *Chem. Soc. Rev.*, 2018, **47**, 8307-8348.

D. Culver, R. Dorn, A. Venkatesh, **J. Meeprasert**, A. Rossini, E. A. Pidko, A. Lipton, G. Lief, and M. Conley, *Active Sites in a Heterogeneous Organometallic Catalyst for the Polymerization of Ethylene*. *ACS Cent. Sci.*, 2021, **7**(7), 1225-1231.

A. Venugopal, L. H. T. Egberts, **J. Meeprasert**, E. A. Pidko, B. Dam, T. Burdyny, V. Sinha, and W. A. Smith, *Polymer Modification of Surface Electronic Properties of Electrocatalysts*. *ACS Energy Lett.* 2022 **7**(5), 1586-1593.

E. Khramenkova, **J. Meeprasert**, E. A. Uslamin, and E. A. Pidko, *Operando Computational Characterization and Modelling in Heterogeneous Catalysis*. *Submitted*.

